Polymer Nanoparticle Design for Ovarian Cancer Therapies

By

Catherine Suzanne Snyder

A dissertation submitted in partial fulfillment
of the requirements for the degree of
Doctor of Philosophy
(Materials Science and Engineering)
at the University of Michigan
2021

Doctoral Committee:

Associate Professor Geeta Mehta, Co-Chair
Associate Professor Anish Tuteja, Co-Chair
Associate Professor Sunitha Nagrath
Professor Max Shtein

Catherine Suzanne Snyder

cssnyder@umich.edu

ORCID iD: 0000-0002-6636-2798

© Catherine Suzanne Snyder 2021

Acknowledgements

Thank you to my advisors who have guided and mentored me these past 5 years.

To the friends that stuck with me through all the ups and downs and made my PhD possible: Caymen Novak, Abhishek Dhyani, Shreya Raghavan, Mathew Boban and Taylor Repetto.

To my lab mates who have been the best company through the long hours: Alex Kate Halvey, Eric Horst, Brian MacDonald and Maria Ward-Rashidi. Especially Michael Bregenzer and Pooja Mehta whose hard work contributed extensively to Chapter 3.

To my undergrads who were wonderful to work with: Ashley Bynum, Nicole Chiu, Erin Parlow, Andrew Rose, Laura Williams and Silva Zhang.

To my family, my life long best friends who are always there for me.

And to Riley, for everything.

Preface

The work presented in this manuscript was completed under the supervision and guidance of Prof. Geeta Mehta and Prof. Anish Tuteja. The following details the work that has previously been published and what work is intended for future publications.

Chapter 2: Section 2.2.1 Non-Spherical Microparticle Fabrication, including Figure 2.1, Figure 2.2, Figure 2.3 and Figure 2.4, are adapted from previous publications[1,2]. Section 2.2.2 Spherical Microparticle Reconfiguration, including Figure 2.5, Figure 2.6, Figure 2.7 and Figure 2.8, is being prepared for publication. Sections 2.2.4 Modification of WETS Substrate for Increase Production and 2.2.5 Nanoscale Fouling of Non-wettable Silane are not intended for publication but will be used for future work on this project.

Chapter 3: The work in this chapter, including all figures, is based on previous work in Prof. Geeta Mehta's lab[3], and is intended for a future publication.

Chapter 4: This work and all figures are unpublished but are intended for a future publication.

Table of Contents

List of Figures

List of Tables

Abstract

Ovarian cancer is the fifth leading cause of cancer related death in females and current clinical treatments have low patient survival rates. Nanoparticle drug delivery has been promoted as an effective therapy, however very few nanoformulations are translated from the lab to the clinic. This absence of successful nanoparticles is partially due to: 1) a lack of understanding of how nanoparticle properties impact *in vivo* biodistribution, 2) nanoparticle design which does not consider the multi-faceted tumor microenvironment (TME), and 3) reliance on chemotherapeutics which cause harsh side effects. My work addressed these shortcomings by designing polymer nanoparticles for improving ovarian cancer treatments.

The first aim was to develop wettability engendered templated self-assembly (WETS), a polymer particle fabrication method. This technique can produce monodisperse, spherical and non-spherical multiphasic particles in a range of 25 nm to 150 μm with up to 7 phases. The size, planar geometry and composition of each phase can be independently altered in non-spherical particles which can be reconfigured into spherical particles. WETS is the first technique which has clearly defined predictive models that allow for the fabrication of extremely varied particles with a single method. With continued work focused on the scale up of WETS, this method could enable the undertaking of a systematic study of particle properties *in vivo*. A survey of particle biodistribution based on size, shape and composition would improve the understanding of nanoparticle drug delivery. Additionally, ideal particle properties for cancer therapies could be identified, thus removing dependance on the rarely observed enhanced permeability and retention effect.

The second aim focused on developing a co-delivery nanoparticle therapy that addresses the supportive nature of non-cancerous mesenchymal stem cells (MSC) in the TME. MSC have been shown to increase cancer stem cells (CSC) chemoresistance and metastasis, and this effect is generally ignored in the design of nanoparticles for drug delivery. Polymer nanoparticles fabricated with electrospraying were demonstrated to encapsulate both paclitaxel and sunitinib with a diameter of 150-200 nm. Delivery of sunitinib as a free drug was shown to disrupt CSC stemness and migration due to MSC co-culture, and co-delivery of sunitinib and paclitaxel was more effective in causing CSC death. This identifies paclitaxel and sunitinib as a possible co-delivery nanoparticle therapy for future studies.

Finally, the third aim investigated α-terpineol (αT), one of the active components of tea tree oil, as a chemotherapeutic for ovarian cancer. αT was found to be more specific in killing ovarian cancer cells as opposed to non-cancerous cells and was able to be encapsulated within an electrosprayed polymer nanoparticle (150-200 nm). Continued work in developing an αT-conjugated polymer could lead to the fabrication of a slow-release formulation with a higher initial αT loading which is hypothesized to be more effective.

In summary, my PhD work has created innovative polymer nanoparticle technologies and therapeutic approaches to kill ovarian cancer cells and improve cure rates. The unique and highly versatile polymer particle fabrication method, WETS, was developed and can contribute extensively to the understanding of nanoparticle behavior *in vivo*. Additionally, investigation into the combination treatment of paclitaxel and sunitinib, as well as αT was carried out which can provide insight to future ovarian cancer therapies. This work reflects the integration of concepts from surface science, polymer and cancer bioengineering in pursuit of eradicating ovarian cancer.

Chapter 1: Introduction

1.1 Introduction to Ovarian Cancer

Cancer is the second leading cause of death in the United States with an estimated 1.8 million new cases diagnosed in 2020[4]. For females, ovarian cancer is one of the most deadly due to late stage detection making it the fifth leading cause of cancer related deaths in females[4,5]. Additionally, a sub-population of cancerous cells, cancer stem cells (CSC) have been linked to the high mortality rate in ovarian cancer due to increased tumor growth, chemoresistance and metastasis[6–8]. However, these CSC do not act alone and are highly influenced by other cell types within the ovarian cancer microenvironment such as macrophages, mesenchymal stem cells (MSC) and fibroblasts among many others[3,9–12]. Macrophages have been linked to angiogenesis, metastasis and enabling CSC immune escape[13]. Cancer-associated fibroblasts have been shown to increase tumor growth, inflammation, chemoresistance and the prevalence of CSC through the secretion of various paracrine factors[11,14]. MSC have recently been implicated in increased chemoresistance, proliferation and invasion of ovarian CSC[15–18].

Assistance from these non-cancerous cells leads to the dissemination of the cancer into the peritoneal cavity which renders surgical removal of cancerous growths much more difficult. Platinum based chemotherapy is usually paired with surgical removal to treat remaining cells and metastasized growths, however this treatment method has a response rate of only ~65% with a median overall survival of ~2-5 years. This low response rate is due to the high frequency of recurrence and development of chemoresistant disease, which is linked to CSC[19,20]. Many patients

become extremely ill during treatment and report feelings of depression and stress due to the fear of reoccurrence, the pain resulting from surgery and chemotherapy, and for younger patients, developed infertility[21]. This highlights the need for additional and more effective treatment methods for ovarian cancer in the clinic which target CSC and their microenvironment-conferred malignant properties, as well as treatments that have gentler side effects on the physical and mental well-being of patients.

1.2 Nanoparticle Drug Delivery as a Cancer Therapy

Nanoparticle drug delivery for cancer therapy has been promised to be next breakthrough for many years since the inception of Paul Ehrlich's 'magic bullet' and Matsumura and Maeda's publication identifying the enhanced permeability and retention (EPR) effect in cancers[22,23]. Nanoparticle passive targeting with the EPR effect allows for a higher accumulation of drug at the tumor site, and less elsewhere in the body as nanoparticles will naturally extravasate at the tumor site due to the leaky vasculature and then remain in the tumor area due to poor lymphatic drainage[24,25]. Functionalizing the nanoparticle surface with targeting agents is a form of active targeting that is used in conjunction with the EPR effect to keep extravasated nanoparticles from being cleared, as well as promoting nanoparticle internalization by the targeted cells[26]. As more drug will naturally be directed to the tumor site using nanoparticles instead of systemic delivery, a higher overall dose can be administered without increasing the severity of the side effects. Additionally, nanoparticle drug delivery also increases the ability to deliver hydrophobic or more fragile drugs, such as siRNA, as the nanoparticles have a prolonged circulation time as well as protecting the drug it is encapsulating from being absorbed or metabolized at a non-specific site[27]. However, despite many publications detailing the benefits of nanoparticle drug delivery, this promise has yet to pan out on a larger scale as only 51 nanoformulations have been approved by

the U.S. Food and Drug Administration (FDA) since 1992 due to many challenges in translation from laboratory to the clinic[28,29].

Some of the challenges that have prevented the development of effective nanoparticle therapies have been extensively discussed[30], but are summarized here. Continued research has shown that the EPR effect is not present in most human cancers and that while encapsulating a drug in a nanoparticle does increase delivery to the target site, the increase is very small compared to the amount of drug that still accumulates in off-target locations[31,32]. Additionally, detailed understanding of how nanoparticle size, shape and chemistry impacts *in vivo* biodistribution is lacking due to a previous reliance on the EPR effect to overcome differences in nanoparticle properties[33,34]. There is also little development in nanoparticle design which is able to increase nanoparticle penetration into solid tumors once the nanoparticles reach the tumor mass, lowering the effectiveness of nanoparticles even further[30,35].

1.3 Thesis Overview and Impact

In this work, polymer nanoparticle systems were designed in order to address some of the short comings of current ovarian cancer therapies through nanoparticle drug delivery. Chapter 2 focuses on the development of a new polymer particle fabrication method, wettability engendered templated self-assembly (WETS). This method is the first that can produce monodisperse, spherical and non-spherical multiphasic particles with independent control of the nanoparticle's size, shape, and chemistry as well as that of each individual phase. Predictive models for both non-spherical and spherical particles have been defined and enable the fabrication of particles with specific sizes, shapes, chemistries, and phase morphologies. Synthesis of systematically varied particles, produced with a single method, could enable the undertaking of a detailed study of particle properties *in vivo*. Results from such a study would greatly increase knowledge in the field

of nanoparticle drug delivery as particle properties could be directly linked to circulation rates, biodistribution and tumor accumulation. With this knowledge, identification of ideal particle properties could overcome the lack of the EPR effect seen in human cancer, increase *in vivo* nanoparticle uptake and improve nanoparticle efficacy overall.

Chapter 3 investigates the fabrication and design of electrosprayed polymer nanoparticles for the co-delivery of paclitaxel, an antimicrotubule-chemotherapeutic, and sunitinib, a tyrosine kinase inhibitor. This co-delivery nanoparticle seeks to leverage the role of CSC-MSC interactions in CSC chemoresistance to improve toxicity of paclitaxel to CSC. Electrosprayed nanoparticles with diameters of 150-200 nm successfully encapsulated paclitaxel and sunitinib, demonstrating the feasibility of co-delivery electrospray nanoparticles to target CSC-MSC interactions and improve clinical outcomes. This potential was further evaluated through co-delivery of the free drugs using a 3D hanging drop model to study how this treatment would impact CSC chemoresistance, migration and stemness.

Chapter 4 focuses on studying α-terpineol, an active component of tea tree oil, as an alternative chemotherapeutic. α-terpineol delivered without modification was found to be more toxic to ovarian cancer cells than non-cancerous cells and can be encapsulated in electrosprayed polymer nanoparticles with diameters of 150-200 nm. It is hypothesized that α-terpineol has the potential to serve as a cancer therapy with fewer negative side effects than current ovarian cancer treatments.

Taken together, this work seeks to improve nanoparticle drug delivery through 3 methods: 1) by identifying polymer nanoparticles that are more effective in reaching the tumor site by developing a fabrication method to study particle behavior *in vivo*, 2) by investigating a co-delivery nanoparticle which targets, not just the cancer cells, but a part of the complex tumor

microenvironment, and 3) studying an alternative chemotherapeutic which has the potential to reduce the negative side effects seen in the clinic.

Chapter 2: Wettability Engendered Templated Self-Assembly (WETS) for the Fabrication of Multiphasic, Spherical and Non-spherical Polymer Particles

2.1 Introduction

Nanoparticles have been developed for many medical uses such as drug delivery, imaging, tissue engineering and regenerative medicine[36–39]. However, despite the many benefits of these particles, fabrication of monodisperse particle samples, or more complex particles such as non-spherical, stimuli-responsive, or multiphasic particles has been difficult. Multiphasic particles have many advantages in medical applications, including: 1) a separate compartment for each payload which avoids negative interactions and allows for independent release rates, 2) the means to encapsulate payloads with different solubilities, 3) the ability to combine diagnostic and therapeutic agents, 4) multiple surface chemistries for additional functionality and 5) orientation directed self-assembly[1,40–49]. Stimuli-responsive particles are projected to have a significant impact on a wide range of applications including self-assembled structures[50–52], biosensors/actuators[53–56] and drug delivery[40,57–59]. For drug delivery, specifically, conflicting particle requirements, such as a spherical versus non-spherical shape, are needed for overcoming different biological hurdles, and an *in situ* reconfiguration could potentially increase nanoparticle targeting[58–62]. Finally, polydisperse samples will have varying biodistributions, drug release profiles and degradation rates which can cloud either definitive results or the effectiveness of a medical treatment making monodisperse samples ideal[26,63,64].

Combining several of these challenging designs into one fabrication method also increases the difficulty, and current fabrication methods have yet to include them all in a fully operational manner. Electrospray and emulsion methods can fabricate multiphasic particles at a higher yield and can produce non-spherical particles, but can be challenging to produce small (<100 nm) and monodisperse samples[46,65–68]. Microfluidic devices can easily produce monodisperse samples and multiphasic particles but increasing the yield and maintaining monodispersity is difficult as it requires many parallel devices operating in sync[69,70]. Additionally, microfluidic devices can fabricate non-spherical particles, however stop-flow lithography and cross-linkable polymers must be employed which slows production and limits particle chemistry[71]. A unique method, Particle Replication in Non-wetting Templates (PRINT), uses a mold to create non-spherical, monodisperse particles and has been scaled up to support *in vivo* studies[72,73]. However, methods to create multiphasic PRINT particles have not been scaled beyond a proof of practice and spherical particles cannot be fabricated due to the mold requiring at least one flat face[74,75].

Application of nanoparticles has also been difficult as, despite thousands of publications detailing improvements in nanoparticle design, there has not been an increase in nanoparticle delivery to target locations or in clinical translation[28,29,34,35]. One difficulty lies in the scale up production of nanoparticles from the laboratory to clinical trials. Another challenge is the physiological barriers that nanoparticles face *in vivo*, especially as the enhanced permeability and retention (EPR) effect is not present in most human cancers[32,76,77]. Most nanoparticle designs for the past 30 years have relied on the EPR effect to assist in targeting, and only recently have investigations been made into how nanoparticle properties impact *in vivo* behaviors such as circulation time and accumulation locations. A systematic study of nanoparticle properties *in vivo* is needed, however being able to fabricate particles for such an undertaking has not been possible.

The nanoparticle fabrication method must be able to produce monodisperse particles, spherical and non-spherical particles in a range of sizes, and multiphasic particles with independent control of all characteristics. If the nanoparticles cannot be produced with the same method, or independent control of nanoparticle properties cannot be maintained, then it may be difficult to make definite conclusions. This has led to the development of the Wettability Engendered Templated Self-assembly (WETS) particle fabrication method which was first demonstrated on the microscale to fully develop and understand the process before investigations into reducing particle size and increasing production were initiated.

2.2 Results and Discussion

2.2.1 Non-spherical Microparticle Fabrication

The WETS method (Figure 2.1A) uses patterned wettability templates in order to fabricate non-spherical microparticle assemblies on its surface. The patterned wettability templates have a fluorinated non-wetting background with a low contact angle hysteresis which allows liquids to recede from the surface. The wettable portion of the template forms discrete domains of high energy titanium dioxide (TiO_2) which has a high contact angle hysteresis and prevents liquids from receding. When this patterned substrate is dip-coated into a polymer solution, the polymer solution will self-assemble in the wettable domains, filling the size and shape of the domain, and will recede from the background creating discrete droplets on the surface. Upon evaporation of the solvent, the polymer will take the size and shape of the wettable domain creating a non-spherical polymer layer. The first polymer layer deposited is the release layer, and it will be dissolved to release the particle assemblies from the substrate once the particle is complete. Subsequent polymer layers are deposited by dip-coating the substrate in sequential polymer solutions and each layer forms a new phase of the resulting particle. These additional layers will also recede from the non-wetting

background and thus form directly on top of the previous layer (Figure 2.1B-D). Once all desired layers have been dip-coated, the release layer is dissolved and the particles harvested, after which the substrate can be reused. A final reconfiguration step can be taken to form spherical particles from the non-spherical particles that are collected from the substrate. As the polymer solution completely fills the wettable domain, the size and shape of the particles is determined by the dimensions of this domain. This allows for a very high degree of control of the lateral dimensions of the non-spherical particle and the fabrication of virtually any desired size and shape (Figure 2.1E-H).

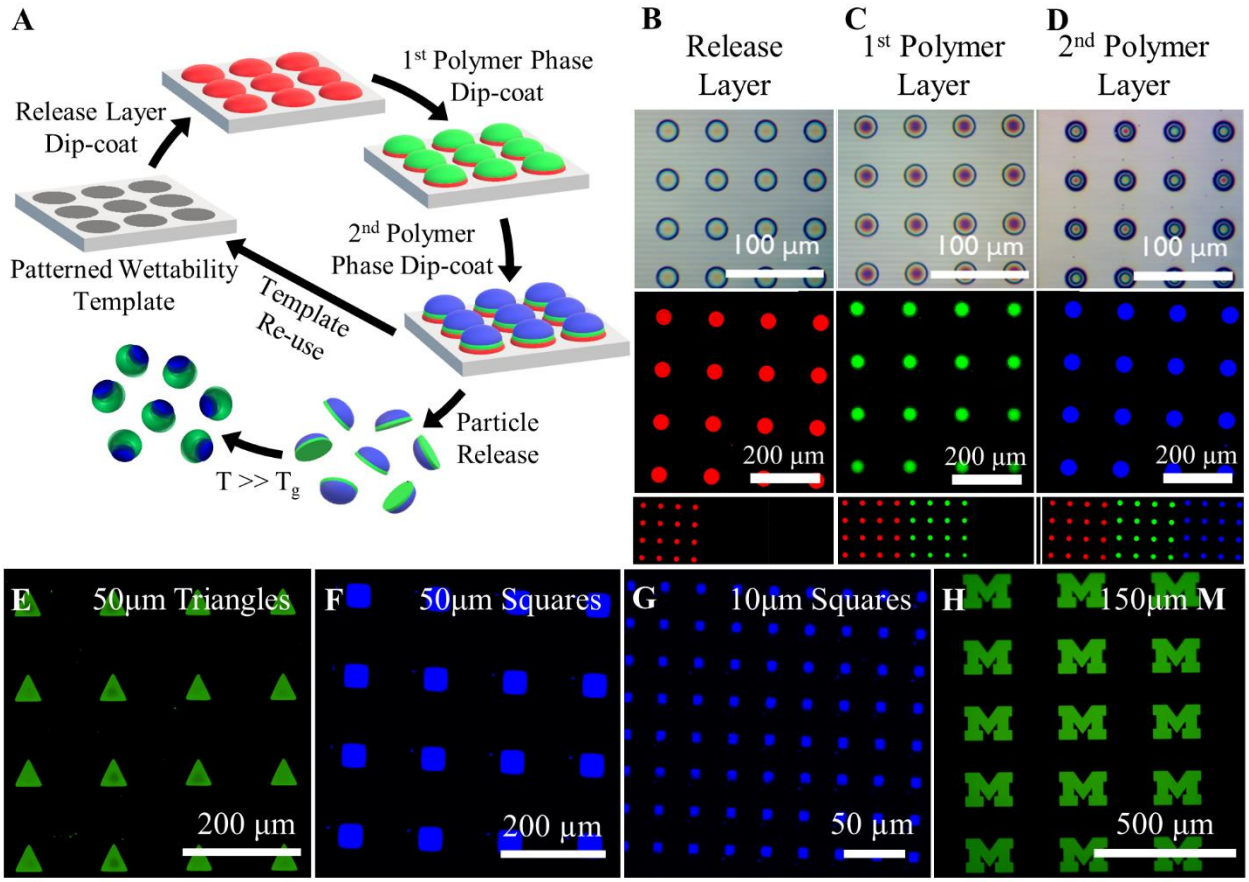

Figure 2.1: WETS fabrication method schematic and non-spherical particle assemblies
A) Schematic depicting the fabrication of biphasic particles using the WETS method. Optical (top) and fluorescent (middle and bottom) microscopy images of the B) release layer, C) first polymer layer and the D) second polymer layer. Fluorescent microscopy images of non-spherical particle assemblies of various sizes and shapes including E) 50 µm triangles, F) 50 µm squares, G) 10 µm squares and H) 150 µm block Ms.

WETS substrates can also be used to fabricate charged, multiphasic polymeric particles by adding polyelectrolyte bilayers to a polymer core. Fabrication of charged particles begins with the same method as mentioned previously: dip-coating of the release layer and then the first polymer layer which serves as the polymer core. After this, the substrate is dip-coated in a polyelectrolyte solution and followed by a water wash. Next the oppositely charged polyelectrolyte is dip-coated and followed by a water wash which then creates one bilayer on the surface of the polymer core (Figure 2.2A). Dip-coating can alternate between the two polyelectrolyte solutions as many times as desired to build up the thickness of the charged phase which can be measured by atomic force microscopy (AFM) (Figure 2.2B-F) and seen with scanning electron microscopy (SEM) (Figure 2.2G, H). By altering the charge of the polymer core and the final layer of the polyelectrolyte bilayer, particles with different surface charges can be fabricated, and highly charged payloads, such as siRNA, can be encapsulated (Figure 2.2I).

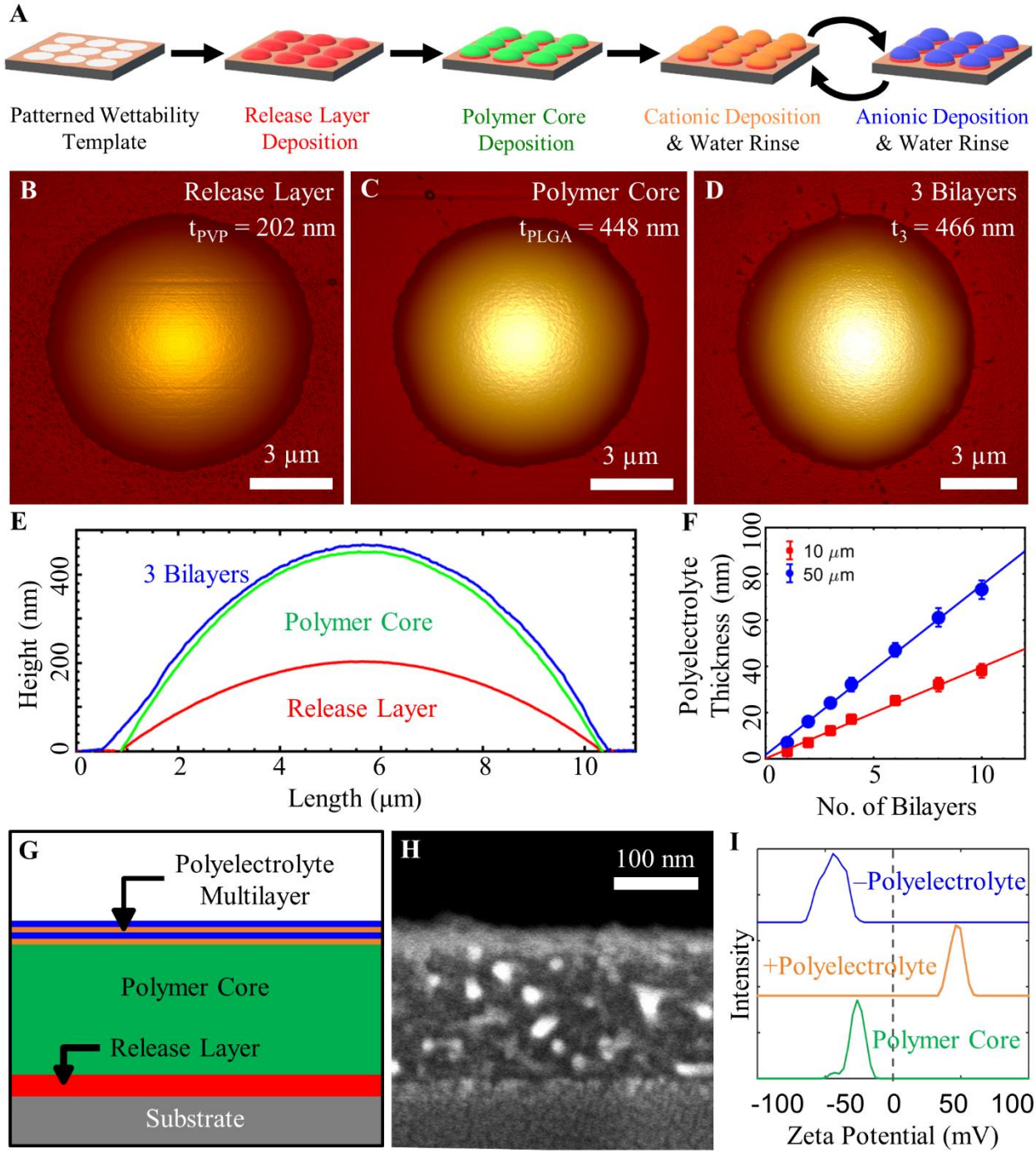

Figure 2.2: Charged, multiphasic particles can be fabricated using the WETS method
A) Schematic of the WETS method incorporating the dip-coating and water washes of polyelectrolyte solutions. AFM scans showing the particle thickness after dip-coating the B) release layer, C) polymer core and D) 3 polyelectrolyte bilayers. E) Compilation of the height profiles from (B), (C) and (D). F) Plot of the linear increase in bilayer phase thickness as the number of bilayers increases as measured with AFM. G) Schematic of the cross section of a particle with two bilayers. H) SEM cross-section of a particle with two polyelectrolyte bilayers. I)

Zeta potential measurements of released particles based on the final layer deposited during dip-coating.

Lateral dimensions of particles fabricated with WETS are controlled by the size and shape of the wettable domain on the substrate. Particle thickness can be measured with AFM, and each added layer can be measured individually knowing that the AFM height will be the combined thickness of all the layers previously deposited and the most recent one (Figure 2.3A-G). The thickness of the polymer layer deposited, *t*, is controlled by the dip-coating parameters and can be modeled with Equation 2.1, where ϕ is the polymer volume fraction of the polymer solution, *W* is the width of the wettable domain, μ is the polymer solution viscosity, *V* is the dip-coating withdrawal rate, γ_{LV} is the surface tension of the polymer solution and *k* is a linear constant (Figure 2.3H).

Equation 2.1 $$t = k\phi W \left(\mu V / \gamma_{LV}\right)^{\frac{1}{3}}$$

As previously seen in Figure 2.2E and also seen in the SEM cross-section in Figure 2.3I, the polymer layers take the shape of a spherical cap and the thickness of the particles is measured in the center which is usually the highest point. The total particle thickness will be the sum of all the layers which comprise the particle. The ability to individually control each layer's chemistry, composition and thickness will allow for exquisite control over the design of multiphasic particles, and in turn help study the impact of each parameter on *in vivo* behavior and effectiveness (Figure 2.3J, K). As the lateral dimensions are controlled by the dimensions of the wettable domain, the thickness of the particle is independently controlled by the dip-coating parameters.

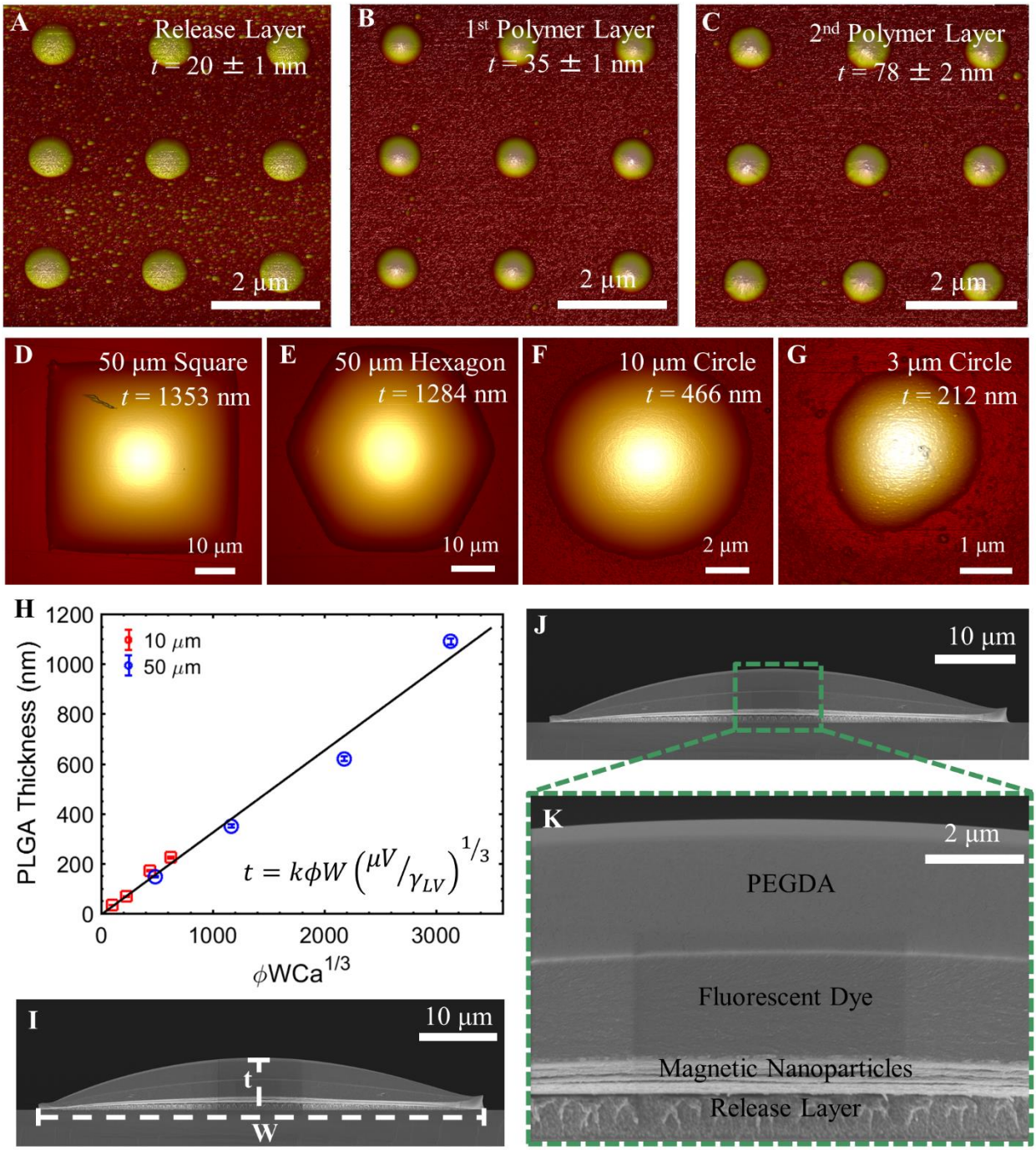

Figure 2.3: The thickness of each polymer layer in a multiphasic WETS particle is individually controlled by the dip-coating parameters of that layer

AFM height scans of particle assemblies as the A) release, B) first polymer and C) second polymer layers are deposited. Thicknesses measured when more than one layer is present is the sum of all previous layers and the most recent. AFM thickness measurements of various particles including a D) 50 µm square, E) 50 µm hexagon, F) 10 µm circle and G) 3 µm circle. H) Plot showing the layer thickness equation for the same polymer solution but on two different wettable domain widths. I) SEM cross-section of a tri-phasic particle assembly showing the spherical cap morphology with *t* measured at the center of the particle and *W*, the width of the domain/particle

on the substrate. J) The same particle shown in (I) but indicating the area of interest K) enlarged to show the three different phases and their payloads.

The non-spherical, multiphasic particle assemblies are released from the substrate by dissolving away the release layer and are then collected for further characterization (Figure 2.4). The WETS substrates are then reused to fabricate another batch of particles. This subsequent batch of particles produced with the same substrate can be exactly the same and added to the first batch to increase the number of particles, or the new particles can be fabricated with different dip-coating parameters to adjust their properties. The wettable domain of the substrate, which dictates the lateral dimensions of the particle, will be the only property that limits how different the second batch of particles can be. Various polymers can be used to alter surface chemistry, a different number of phases can change which combination of cargo are loaded and the thickness of each phase can be adjusted to fine tune the Janus balance, or ratio of phases. Despite the range of purposeful differences between the batches of particles, direct comparisons between the particles can still be made as they will have been fabricated with the same method.

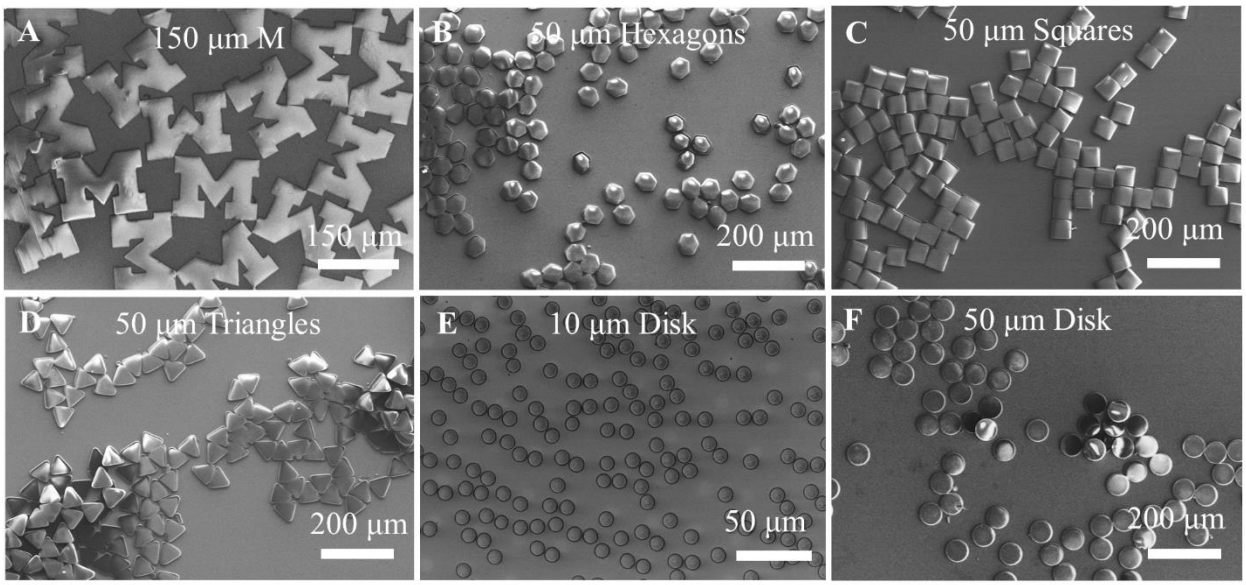

Figure 2.4: Released non-spherical, multiphasic WETS particles of various sizes, shapes and compositions

SEM images of A) 150 μm block Ms, B) 50 μm hexagons, C) 50 μm squares, D) 50 μm triangles, E) 10 μm disks, F) 50 μm disks.

2.2.2 Spherical Microparticle Reconfiguration

Fabrication of spherical particles from non-spherical particles occurs after the non-spherical particles have been released from the reusable WETS templates, and the particles have been collected in a liquid medium, generally water. The liquid medium, and thus the particles are then heated to a temperature above the glass transition of all the polymers comprising the particles and the temperature is maintained until the polymer chains have reconfigured the particle into a sphere. For polymers that have glass transition temperatures above 100°C, a 50% water and 50% glycerol solution was used as the liquid medium. Once the particle reconfiguration is complete, the particle solution is then returned to room temperature and the particles solidified. The liquid medium can then be evaporated or replaced through centrifugation pelleting. During reconfiguration, the non-spherical particles will begin to shrink and fold, which can be seen in partially reconfigured particles that have been frozen (Figure 2.5A, B, D, E). Particles maintained at a higher temperature for longer will continue to fold and shrink until a sphere is formed (Figure 2.5C, F). The volume of the particle is maintained during reconfiguration, and therefore the diameter (d_s) of the resulting spherical particle can be determined by relating the volume of a spherical cap (width d_w and thickness t) to that of a sphere (Equation 2.2, Figure 2.5G, H).

Equation 2.2 $$d_s = \sqrt[3]{\frac{3}{4}d_w^2 t + t^3}$$

As seen in Figure 2.5A-F, reconfiguration is not an instantaneous process, and the time needed will depend on the temperature, size of the particles and the individual glass transition temperatures (Figure 2.5I).

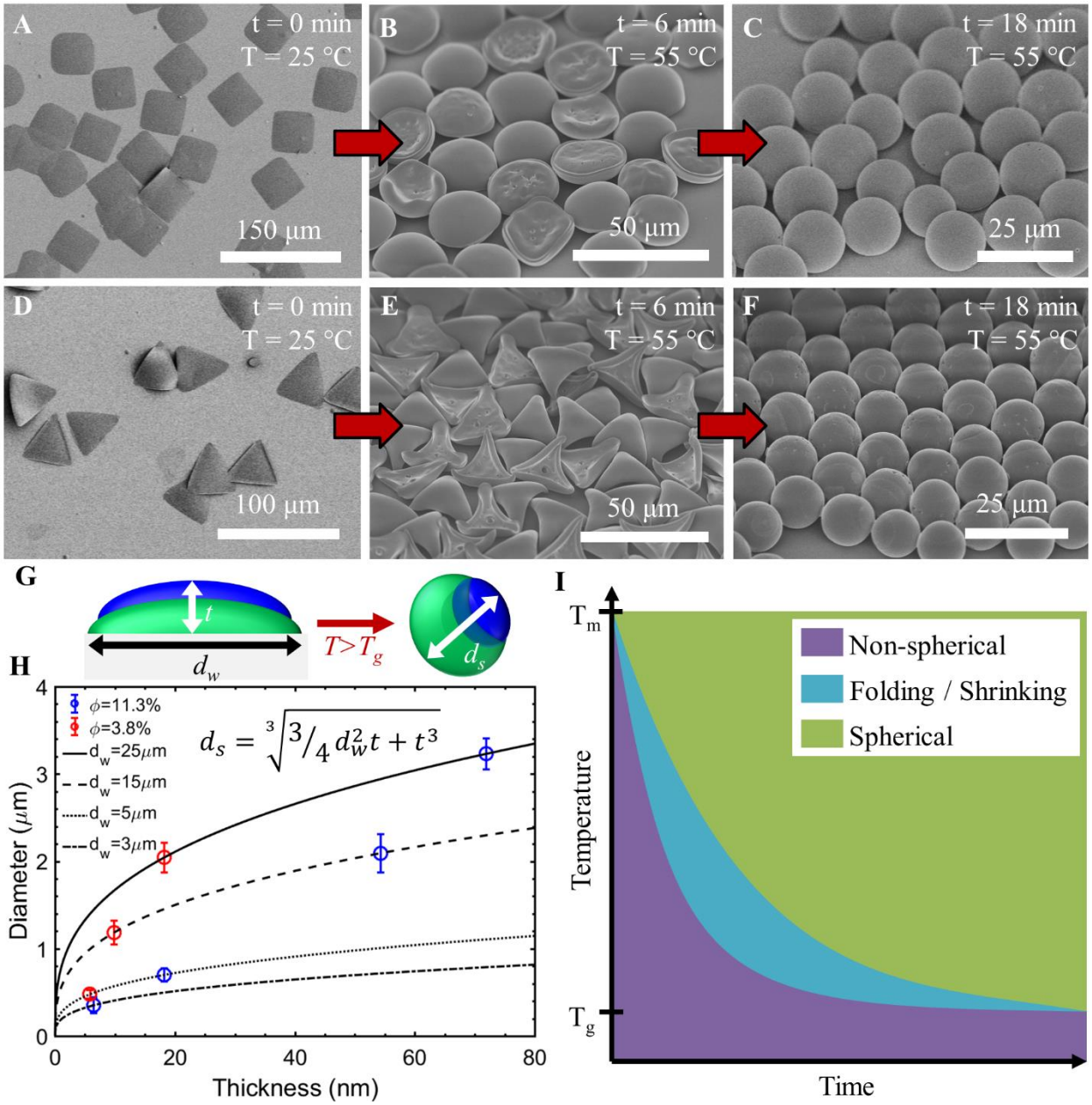

Figure 2.5: Reconfiguration of non-spherical particles to spherical particles
SEM images of A) non-spherical, square particles before reconfiguration, B) after 6 minutes of reconfiguration and C) after 18 minutes of reconfiguration where the particles are now spheres. SEM images of D) non-spherical, triangle particles before reconfiguration, E) after 6 minutes of reconfiguration and F) after 18 minutes of reconfiguration where the particles are now spheres. G) Schematic of a non-spherical particle and the possible spherical particle resulting from reconfiguration. H) Plot showing how the volume of the particles are maintained during reconfiguration and thus the resulting spherical diameter can be predicted based on the known dimensions of the non-spherical particle. I) Suggested phase diagram of particle reconfiguration based on time and temperature.

In addition to volume, particle properties are translatable during the reconfiguration from non-spherical to spherical. For example, the Janus balance can be maintained which is important for co-delivery of drugs in drug delivery applications. By adjusting the polymer volume fraction of the two different polymers during the dip-coating process, the Janus balance can be adjusted (Figure 2.6A-C). Integrity of the two different phases can also be seen post-reconfiguration. To understand the morphology of these multiphasic, spherical particles, individual phases were preferentially dissolved. Figure 2.6D, E depict an SEM image and a schematic of a biphasic particle with a single phase dissolved showing a concave morphology indicating that the dissolved phase was partially encapsulated by the other. In Figure 2.6F, attempted dissolution of a phase shows no change in the particle morphology suggesting that one phase is completely encapsulated by the other phase creating a core-shell morphology. Triphasic particles can also be reconfigured (Figure 2.6G), and Figure 2.6H, I depict selective dissolution of different phases indicating that the phases form a nested, partially encapsulated morphology.

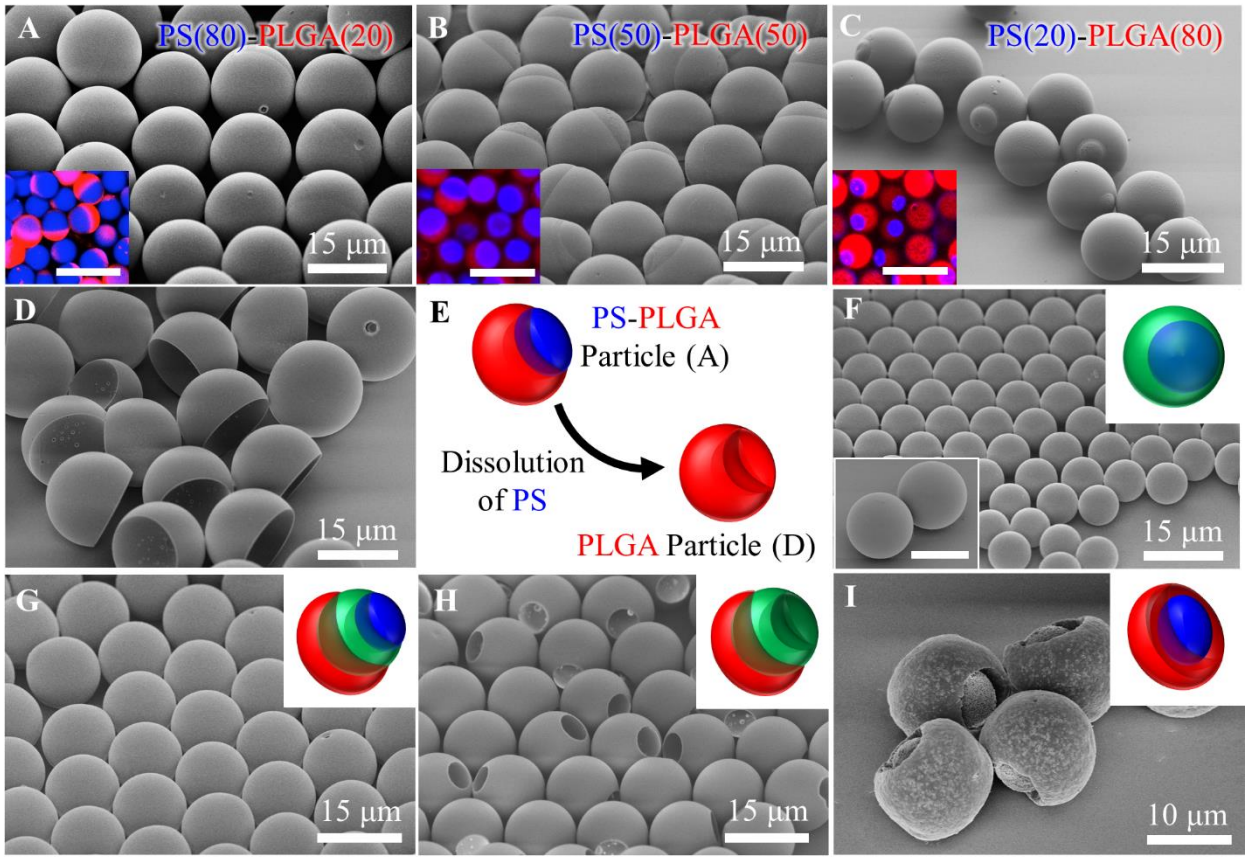

Figure 2.6: Exploring the morphology of reconfigured, multiphasic, spherical particles
SEM images of a biphasic PS(blue)-PLGA(red) particle with different dip-coating parameters of A) 80 vol% PS and 20 vol% PLGA, B) 50 vol% PS and 50 vol% PLGA, and C) 20 vol% PS and 80 vol% PLGA to alter the resulting Janus balance. Insets (A)-(C) are fluorescent microscopy images of the same particles showing the maintained integrity of the different phases. Inset scale bar is 25 µm. D) SEM image of the particles from (A) where the PS phase has been dissolved with cyclohexane showing the morphology of the PLGA phase. E) Schematic of the dissolution of the PS phase and the remaining PLGA phase. F) SEM image of a PMMA-PS core-shell particle where (inset) treating with cyclohexane causes no change in the particle morphology. Inset scale bar is 10 µm. Upper right inset is a suggested schematic of the core-shell particle. G) SEM image of a reconfigured triphasic particle PS(blue)-PLGA(red)-PVAc(green) with a suggested schematic in the upper right. H) Dissolution of the PS phase with cyclohexane of the same particles in (G). Inset depicts a schematic of the particles. I) Particles from (G) treated with ethanol to dissolve the PVAc phase. The inset depicts the morphology of the particles post-dissolution.

Regardless of the starting shape of the non-spherical particle, after reconfiguration the shape will always be a sphere due to the minimization of the interfacial surface energies of all polymer-liquid ($\gamma_{P,L}$) and polymer-polymer ($\gamma_{P1,P2}$) interfaces in the system, and as $\gamma_{P,L}$ is typically much higher than $\gamma_{P1,P2}$. The total interfacial energy for a biphasic particle can be defined in

Equation 2.3, where A is the interfacial area. For a particle system with more phases, more terms would be required.

Equation 2.3 $$E = \gamma_{P_1L}A_{P_1L} + \gamma_{P_1P_2}A_{P_1P_2} + \gamma_{P_2L}A_{P_2L}$$

For a biphasic particle, there are three possible morphologies after reconfiguration: phase separated, partially encapsulated and core-shell (Figure 2.7A). Boundary conditions defined by $\gamma_{P1,P2}$ determine which phase is energetically favorable. For the boundary condition between a core-shell and a partially encapsulated particle (Figure 2.7B), it was assumed that the change in $A_{P1,P2}$ (area of the shared interface of P_1 and P_2) between the two configurations is very small, and the change in $A_{P1,P2}$ can be represented as $\Delta A_{P1,P2} = dA$. Therefore, $\Delta A_{P1,L} = dA$, and $\Delta A_{P2,L} = -dA$ and the difference in surface free energy between the two morphologies can be calculated (Equation 2.4), where E_{CS} and E_{PE} are the core-shell and partially encapsulated energies, respectively.

Equation 2.4 $$E_{CS} - E_{PE} = \gamma_{P_1L}dA + \gamma_{P_1P_2}dA - \gamma_{P_2L}dA$$

For a stable core-shell morphology, the energy can be written as Equation 2.5.

Equation 2.5 $$E_{CS} - E_{PE} = \gamma_{P_1L}dA + \gamma_{P_1P_2}dA - \gamma_{P_2L}dA < 0$$

Where Equation 2.6 can be determined as the boundary condition for a stable core-shell morphology based on Equation 2.4 and Equation 2.5.

Equation 2.6 $$\gamma_{P_1P_2} < \gamma_{P_2L} - \gamma_{P_1L}$$

Similarly, the conditions between a phase separated morphology and a partially encapsulated morphology can be determined when it is assumed that $\Delta A_{P1,P2} = -dA$, $\Delta A_{P1,L} = dA$, and $\Delta A_{P2,L} = dA$ (Figure 2.7C). The difference in energy between E_{PS} (phase separated) and E_{PE} can be written as Equation 2.7 which defines a stable phase separated condition.

Equation 2.7 $$E_{PS} - E_{PE} = \gamma_{P_1L}dA - \gamma_{P_1P_2}dA + \gamma_{P_2L}dA < 0$$

From this, the condition for a stable phase separated morphology can be simplified to Equation 2.8.

Equation 2.8 $$\gamma_{P_1P_2} > \gamma_{P_2L} + \gamma_{P_1L}$$

The conditions for a partially encapsulated morphology can then be determined from Equation 2.9 and Equation 2.10 to give the simplified conditions (Equation 2.11 and Equation 2.12).

Equation 2.9 $$E_{CS} - E_{PE} = \gamma_{P_1L}dA + \gamma_{P_1P_2}dA - \gamma_{P_2L}dA > 0$$

Equation 2.10 $$E_{PS} - E_{PE} = \gamma_{P_1L}dA - \gamma_{P_1P_2}dA + \gamma_{P_2L}dA > 0$$

Equation 2.11 $$\gamma_{P_1P_2} > \gamma_{P_2L} - \gamma_{P_1L}$$

Equation 2.12 $$\gamma_{P_1P_2} < \gamma_{P_2L} + \gamma_{P_1L}$$

Additionally, for partially encapsulated particles, the degree of encapsulation can be defined as the encapsulation ration (*ER*) (Equation 2.13) where *h* is the height of the particle of phase P_2 encapsulated within phase P_1, and D_2 is the diameter of the P_2 phase compartment (Figure 2.7D).

Equation 2.13 $$ER = {}^{h}/_{D_2}$$

With this definition, $h = D_2$ and $ER = 1$ for a core-shell particle and for any particle with $h < D_2$, a portion of P_2 will be exposed and the particle will have a partially encapsulated morphology. For a phase separated particle, $h = 0$ and $ER = 0$, and no portion of P_2 will be encapsulated within P_1.

The encapsulated phase P_2 does not have a perfect spherical shape, but it instead takes a lens shape of a finite angle, α, as seen in (Figure 2.6). This effect comes from the polymers and surrounding liquids forming the shape with the lowest surface area to volume ratio in order to

reduce the total interfacial energy of the system. It is possible to estimate α and θ (the angle between the P_1-P_2 interface and the P_1-L interface) by balancing the interfacial surface tension vectors (Figure 2.7E) at the three phase contact line[78]. This results in Equation 2.14 and Equation 2.15. Note that at the boundary conditions of $\alpha = 0°$ (completely phase separated) and $\alpha = 180°$ (core-shell) corresponds to the limiting conditions given by Equation 2.6, Equation 2.11 and Equation 2.12.

Equation 2.14 $$\cos\theta = \frac{\gamma_{P_1L}^2 - \gamma_{P_1P_2}^2 - \gamma_{P_2L}^2}{2\gamma_{P_1P_2}\gamma_{P_2L}}$$

Equation 2.15 $$\cos\alpha = \frac{\gamma_{P_2L}^2 - \gamma_{P_1P_2}^2 - \gamma_{P_1L}^2}{2\gamma_{P_1P_2}\gamma_{P_1L}}$$

Finally, the total interfacial energy equation (Equation 2.3) can be written as a function of h and D_2, which make up the encapsulation ratio (Equation 2.13), instead of A, thus creating a model which can predict the morphology of a given biphasic particle system upon reconfiguration. For this model, P_2 was assumed to always be a sphere which would make D_2 a constant equal to $2r_2$. The shared interface between P_1 and P_2, ($A_{P1,P2}$) will be the surface area of a spherical cap that will increase with an increase in h (Figure 2.7F, Equation 2.16).

Equation 2.16 $$A_{P_1P_2} = \pi(a^2 + h^2)$$

The radius of the spherical cap, a, can be written as a^2 in terms of h using the equation of a circle (Figure 2.7G). Equation 2.17 and Equation 2.18, show the simplified definitions of a^2 and $A_{P1,P2}$, respectively.

Equation 2.17 $$a^2 = hD_2 - h^2$$

Equation 2.18 $$A_{P_1P_2} = \pi h D_2$$

The area of the interface between P_2 and the liquid medium (L) is $A_{P2,L}$ and will be the surface area of P_2 less the area in contact with P_1 which was previously defined in Equation 2.18. This area will also be a function of h as $A_{P2,L}$ (Equation 2.19) will decrease with an increase in h.

Equation 2.19 $$A_{P_2L} = \pi D_2^2 - \pi h D_2$$

$A_{P1,L}$ is the area of the interface between P_1 and the liquid medium (L) and will change based on the volume of P_2 that is engulfed within P_1. The volume of P_2 that is engulfed, V_{P2cap}, will be the volume of the spherical cap highlighted in Figure 2.7F, however the equation of a sphere (Figure 2.7H) will be used to define a^2 and V_{P2cap} in terms of h as shown in Equation 2.20 and Equation 2.21, respectively. The combined volume of P_1 and V_{P2cap} is $V_{1,2}$ (Equation 2.22) where D_1 is the diameter of P_1 if it was a spherical, single-phase particle.

Equation 2.20 $$a^2 = \frac{1}{2} h D_2 - \frac{1}{2} h^2$$

Equation 2.21 $$V_{P_2 cap} = \frac{1}{4} \pi h^2 D_2 - \frac{1}{12} \pi h^3$$

Equation 2.22 $$V_{1,2} = V_{P_1} + V_{P_2 cap} = \frac{1}{6} \pi D_1^3 + \frac{1}{4} \pi h^2 D_2 - \frac{1}{12} \pi h^3$$

$V_{1,2}$ will take the shape of a spherical cap with a as the radius of the cap and $h_{1,2}$ as the height of the cap (Figure 2.7I) as defined by Equation 2.23 which will be equal to Equation 2.22. Setting Equation 2.22 equal to Equation 2.23 and solving for $h_{1,2}$ in terms of h results in Equation 2.24. $h_{1,2}$ as a function of h can now be substituted into $A_{P1,L}$ to create a definition for the interface area between P_1 and the liquid medium (Figure 2.7I) as a function of h (Equation 2.25).

Equation 2.23 $$V_{1,2} = \frac{1}{6} \pi h_{1,2}^3 + \frac{1}{4} \pi h_{1,2} (h D_2 - h^2)$$

Equation 2.24 $$h_{1,2} = \frac{\sqrt[3]{\sqrt{m^2 + 2n^3} - m}}{2^{\frac{2}{3}}} - \frac{n}{2^{\frac{1}{3}} \sqrt[3]{\sqrt{m^2 + 2n^3} - m}}$$

Equation 2.24a $$m = h^3 - 3h^2 D_2 - 2D_1^3$$

Equation 2.24b $$n = hD_2 - h^2$$

Equation 2.25 $$A_{P_1L} = \pi\left(h_{1,2}^2 + hD_2 - h^2\right)$$

With all three interface terms, $A_{P1,P2}$ (Equation 2.18), $A_{P2,L}$ (Equation 2.19) and $A_{P1,L}$ (Equation 2.25) defined in terms of h, the total interfacial energy, E (Equation 2.3), can be plotted against the encapsulation ratio (ER) and the minimum found. The ER at the minimum E will predict if the particle will be a core-shell ($ER = 1$), partially encapsulated ($1 > ER > 0$), or phase separated ($ER = 0$).

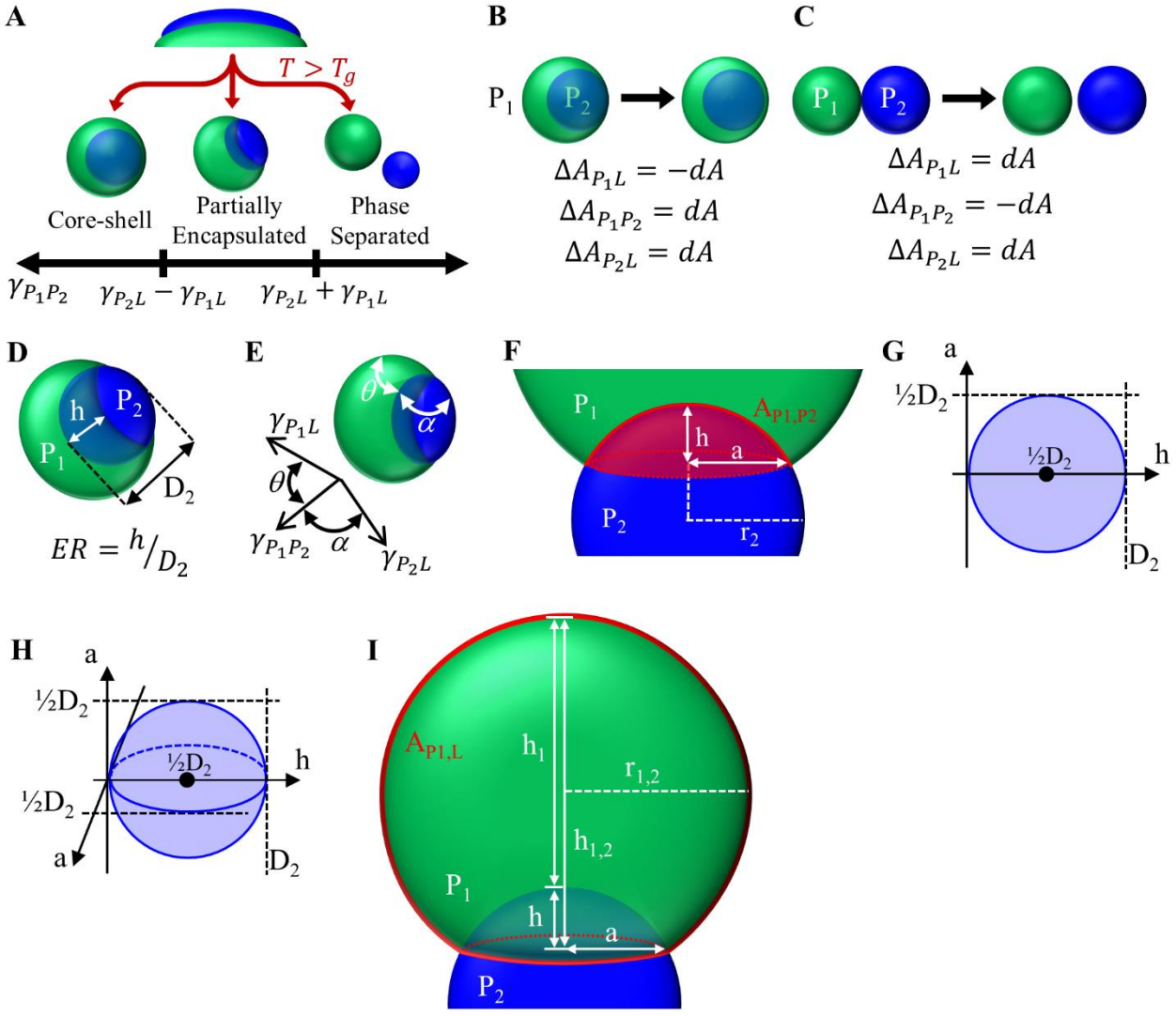

Figure 2.7: Schematics of a spherical biphasic particle used in determining the resulting spherical morphology
A) Schematic of a biphasic, non-spherical particle and the three possible spherical morphologies that it can take upon reconfiguration. B) The boundary condition between a core-shell morphology and a partially encapsulated morphology is determined by this schematic. C) Schematic used to determine the boundary condition between a partially encapsulated morphology and that of a phase separated one. D) Schematic of the dimensions used to define the encapsulation ration (*ER*) of a partially encapsulated particle. E) Schematic of the lens angle between a partially encapsulated phase and the phase surrounding it based on the interfacial surface tension vectors. F) Schematic of the interfacial area $A_{P1,P2}$ (red) between P_1 (green) and P_2 (blue). G) Plot of a circle used in describing the equation of a circle in terms of h and D_2. H) Plot of a sphere used in describing the equation of a sphere in terms of h and D_2. I) Schematic of the interfacial area $A_{P1,L}$ (red) and the defined dimensions.

These predictive models were then applied to biphasic polymer systems to test their accuracy. The first biphasic system included poly(vinyl acetate) (PVAc) and polystyrene (PS), and the second system consisted of poly(methyl methacrylate) (PMMA) and PS. A 50% water and 50% gylcerol solution was utilized as the liquid medium during the shape reconfiguration at ~140°C to accommodate the higher glass transition temperatures. The surface tensions (γ_{lv}) of water and glycerol at 140°C were calculated to be 53.4 mN/m and 52.5 mN/m, respectively, from experimentally determined surface tension values reported in the literature[79,80]. The surface tension of a 50% water-glycerol solution was estimated to be 52.9 mN/m, the average between the surface tensions of water and glycerol at 140°C. The ratio between the polar (γ^p_{lv}) and dispersive (γ^d_{lv}) components was assumed to be constant with temperature[81], and that the polar and dispersive components of the 50% mixture was also the average of the pure water and glycerol values. Table 2.1 lists surface tension values as well as the estimated polar and dispersive components of water, glycerol, and the projected values for a 50% water-glycerol solution. Literature values of polymer surface tensions (γ_{sv}) at 140°C of PS, PVAc and PMMA are listed in Table 2.2[82].

Table 2.1: Liquid Surface tension values and estimated polar and dispersive components at 140°C

Liquid	γ_{lv} **(mN/m)**	γ^d_{lv} **(mN/m)**	γ^p_{lv} **(mN/m)**

Water	53.4[79]	15.6	37.8
Glycerol	52.5[80]	33.6	18.9
50% Water-50% Glycerol	52.9	24.6	28.3

Table 2.2: Polymer surface tension values at 140°C reported by Wu[82]

Polymer	γ_{sv} **(mN/m)**	γ^d_{sv} **(mN/m)**	γ^p_{sv} **(mN/m)**
PS	32.1	26.7	5.4
PVAc	28.6	19.2	9.4
PMMA	32.0	23.0	9.0

To estimate the interfacial surface tension between the 50% water-glycerol mixture and the polymer during the reconfiguration, the harmonic-mean equation was used (Equation 2.26)[81].

Equation 2.26 $$\gamma_{1,2} = \gamma_1 + \gamma_2 - \frac{4\gamma_1^d\gamma_2^d}{\gamma_1^d+\gamma_2^d} - \frac{4\gamma_1^p\gamma_2^p}{\gamma_1^p+\gamma_2^p}$$

Interfacial surface tensions between polymers were reported in the literature by Wu and were used in these calcualtions (Table 2.3)[82]. Based on these values and the boundary conditions determined previously, the PVAc-PS biphasic particle was predicted to have a partially encapsulated morphology and the PMMA-PS particle would be core-shell which is seen in Figure 2.8.

Table 2.3: Interfacial surface tensions of two biphasic particles systems suspended in 50% water-50% glycerol

Particle System (P_1/P_2)	$\gamma_{P1,L}$ **(mN/m)**	$\gamma_{P1,P2}$ **(mN/m)**	$\gamma_{P2,L}$ **(mN/m)**
PVAc/PS	18.3	3.7[82]	19.8
PMMA/PS	15.7	1.7[82]	19.8

Calculating the lens angle in both systems gives $\theta = 72.8°$ and $\alpha = 117.5°$ for the PVAc-PS particle, and $\theta = 0°$ and $\alpha = 180°$ for the PMMA-PS particle. Both of which are in good agreement

with the observed particles (Figure 2.8A, C). Additionally, plotting *E* against *ER* for both particle systems to find E_{min} results in *ER = 0.66* and *ER = 1* for the PVAc-PS and PMMA-PS systems, respectively, which also matches the observed morphology of the particles (Figure 2.8B, D).

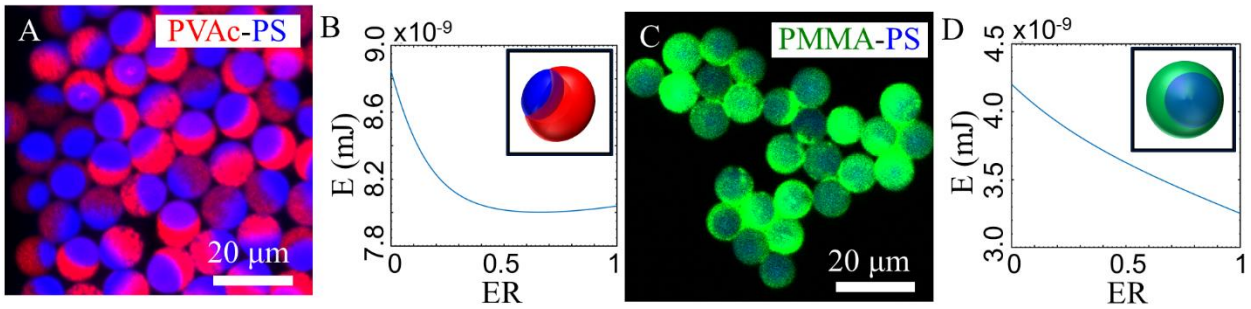

Figure 2.8: Two biphasic particle systems with different spherical morphologies
A) Fluorescent microscopy of PVAc(red)-PS(blue) biphasic particles showing a partially encapsulated morphology. B) *E* vs *ER* plot for the PVAc-PS particles showing $E_{min} \sim 0.66$ with the inset showing a schematic of the morphology. C) Fluorescent microscopy of PMMA(green)-PS(blue) biphasic particles with a core-shell morphology. D) *E* vs *ER* plot for the PMMA-PS particles showing $E_{min} = 1$ indicating a core-shell morphology with a schematic of the morphology in the inset.

2.2.3 Reduction in Particle Size to Nanoscale

The majority of particles fabricated using the WETS method shown up to this point are greater than 1 µm in diameter and are therefore too large to use for a systematic drug delivery study. In order to reduce the overall size of particles produced with WETS, the width of the wettable domains (*W*) would need to be reduced. Several options for reducing *W* were investigated, but first, limits of the current fabrication method were determined. As an ideal target for spherical particles, 100 nm and 200 nm diameter spheres were chosen. The non-spherical particle thickness (Equation 2.1) and the spherical particle diameter (Equation 2.2) equations were used to project what non-spherical particle thicknesses and widths would be required (Figure 2.9). Values from the plot are listed in Table 2.4 and show that for a 200 nm spherical particle, $W \leq 2$ µm would be needed and for a 100 nm particle, $W \leq 750$ nm.

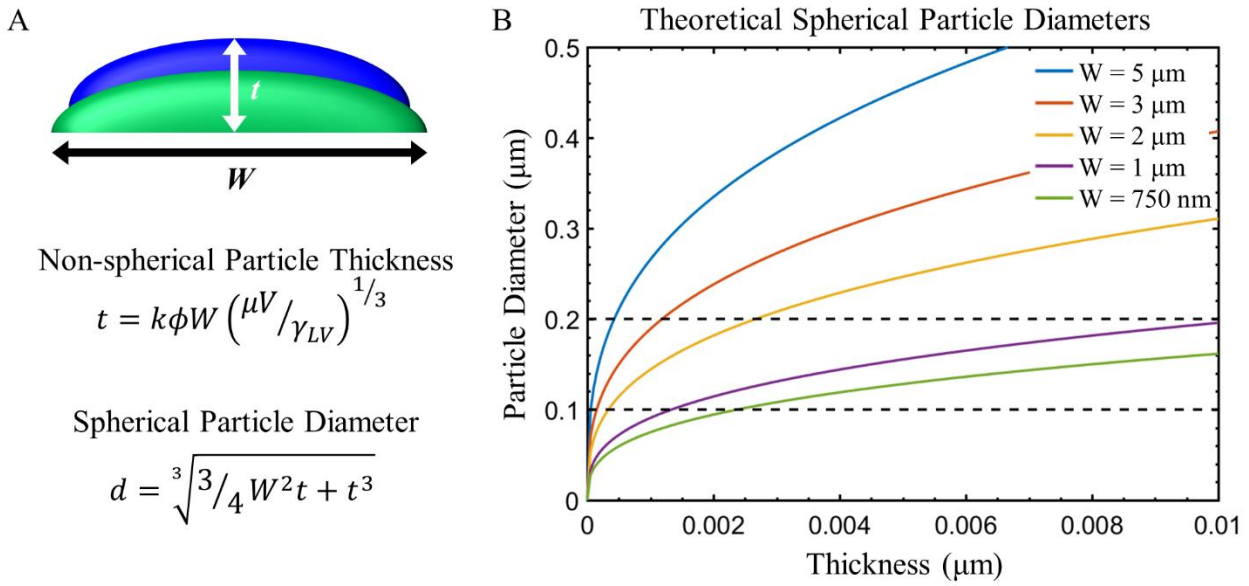

Figure 2.9: Determining required particle thicknesses and domain widths to fabricate 100 nm and 200 nm spherical particles
A) Schematic of a non-spherical particle showing *t*, the particle thickness, and *W*, the width of the domain and particle. Listed below are the equations that define the particle thickness based on dip-coating solutions and parameters, and the spherical particle diameter post-reconfiguration. B) Plot showing how spherical diameter changes for 5 different values of *W* over a thickness of 0 to 10 nm. Dashed lines indicate spherical diameters of 100 nm and 200 nm.

Table 2.4: Required particle thickness for 100 nm and 200 nm spherical particles based on the non-spherical particle width

Spherical Diameter (nm)	**Non-spherical Width (μm)**	**Non-spherical Thickness (nm)**
100	5.00	0
100	3.00	0
100	2.00	0
100	1.00	1
100	0.75	2
200	5.00	0
200	3.00	1
200	2.00	3
200	1.00	11
200	0.75	19

The limit of resolution of standard lithography, the method used to fabricate the WETS surfaces, is 2 μm which could be used to fabricate spherical 200 nm particles. However, this would be the upper limit, and non-spherical particles would be limited to 2 μm as well. One method of reducing W would be to use a stepper in conjunction with standard lithography. The stepper can reduce the pattern of a patterned quartz mask 5 times and to repeat this reduced pattern across the surface of a 4-inch silicon wafer to pattern the entire area. WETS templates were fabricated at the stepper's limit of resolution, 700 nm, and particles were fabricated and analyzed with AFM (Figure 2.10A-D) and SEM (Figure 2.10E-H) showing uniform non-spherical particle assemblies which could be released and collected. Another method investigated used block copolymer lithography to fabricate W = 25 nm WETS templates which was able to produce 25 nm particle assemblies on the templates (Figure 2.10I-P). However, release and collection of the 25 nm particles was difficult and very few particles were able to be harvested making this method unsuitable for larger scale production. Another method investigated but not attempted was e-beam lithography as this method has a limit of resolution of less than 10 nm. Generally, e-beam lithography is used for custom, one-time fabrication as the rate of etching is extremely slow, and as WETS would require a high rate of substrate fabrication this method was deemed non-viable. This left the stepper as the best option for achieving nanoparticles with WETS, even so, the particles would be slightly larger than desired.

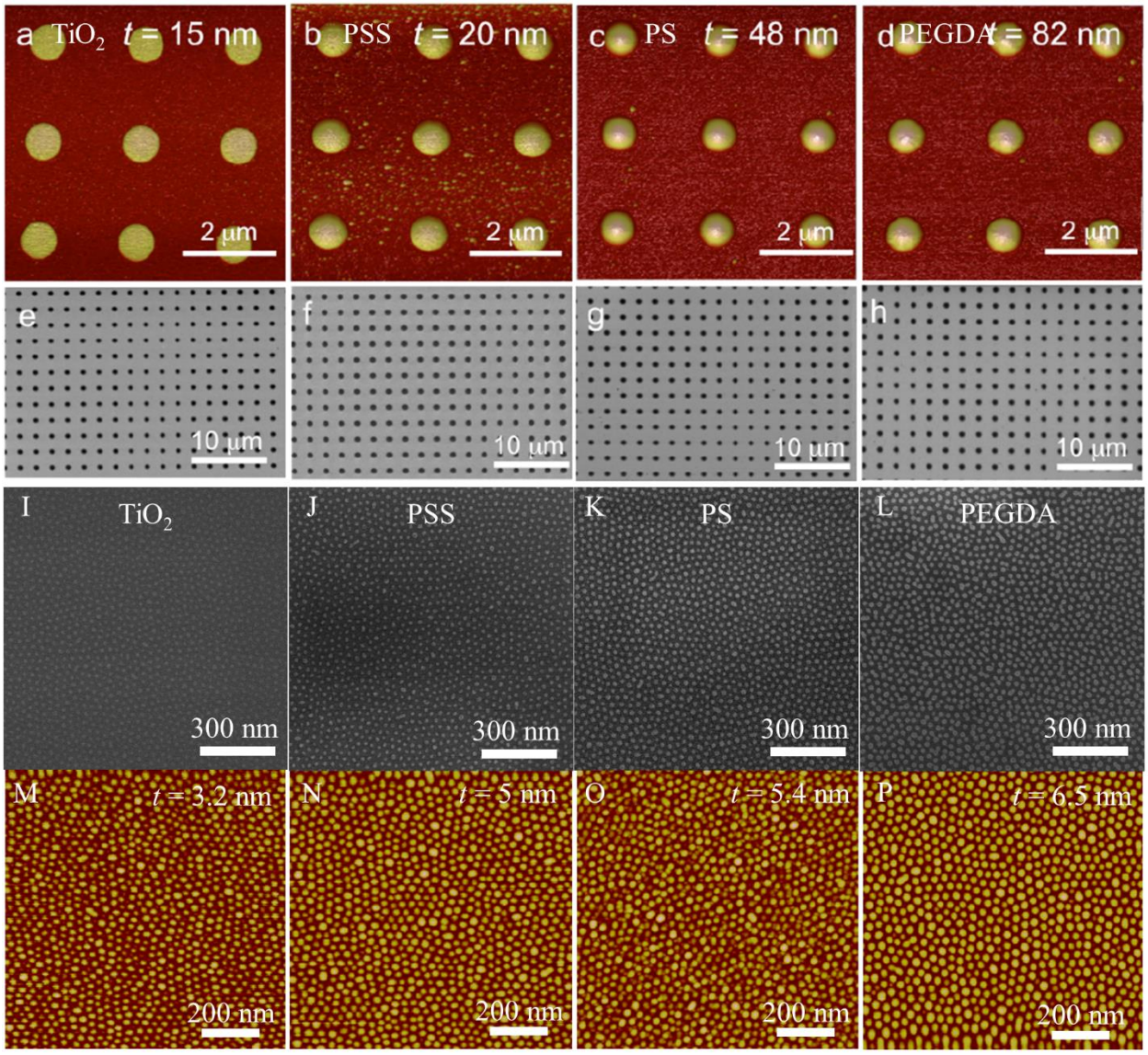

Figure 2.10: 700 nm and 25 nm WETS particles fabricated with stepper lithography and block copolymer lithography

AFM scans of A) 700 nm wettable, TiO_2 domains fabricated with a stepper. B) The release layer PSS deposited on the 700 nm wettable domains. C) PS deposited on top of PSS as the first polymer layer of the WETS particle. D) PEGDA deposited on top of PS and PSS. SEM images of each step of the 700 nm particles: E) 700 nm wettable, TiO_2 domains, F) PSS dip-coated onto the wettable domains, G) PS dip-coated on top of PSS and H) PEGDA dip-coated on top of PS and PSS. SEM images of I) the 25 nm block copolymer fabricated WETS templates with wettable, TiO_2 domains, J) PSS dip-coated onto the wettable domains, K) PS dip-coated onto PSS, L) PEGDA dip-coated onto PS and PSS. AFM scans of M) 25 nm wettable, TiO_2 domains fabricated with block copolymer lithography, N) PSS dip-coated onto the 25 nm wettable domains, O) PS dip-coated onto PSS, P) PEGDA dip-coated onto PS and PSS.

2.2.4 Modification of WETS Substrate for Increased Particle Production

Original production levels of WETS resulted in enough particles for characterization, but not enough for *in vitro* studies which were estimated to need ~10^{12} particles per experiment. In order to increase the number of particles produced with WETS, two different approaches were investigated and combined: 1) increase the reliability and reusability of the WETS substrates, and 2) scale up fabrication of the particles by increasing the size of the WETS substrate. The first method would reduce time needed in fabricating the substrates and would additionally increase the number of usable, monodisperse particle samples. This would also allow for consolidation of different batches as batch-to-batch variability would be removed. The second method would make more particles per batch, thus reducing the time needed to make a sufficient number of particles.

2.2.4.1 Modified Lithography Fabrication

The original WETS substrate fabrication relied on a silicon substrate that was blanketed with TiO_2 through physical vapor deposition, silanized with a non-wetting silane and then the silane was selectively cleaved from the TiO_2 surface with ultraviolet (UV) radiation through a quartz photomask to form the discrete, wettable domains surrounded by a non-wetting background (Figure 2.11A). This substrate fabrication method was faster, however, the high energy state of TiO_2 is not permeant, and re-activation through UV or oxygen plasma would remove the non-wetting background. Over extended uses of the substrate, the size of the wettable domain would shrink, creating particles of smaller and smaller widths until particles no longer patterned on the surface (Figure 2.11B). Additionally, in flawed areas of the silanization, polymer from the dip-coating solution would begin to film across the substrate in larger and larger areas, reducing the number of particles harvested from the substrate with each use (Figure 2.11C).

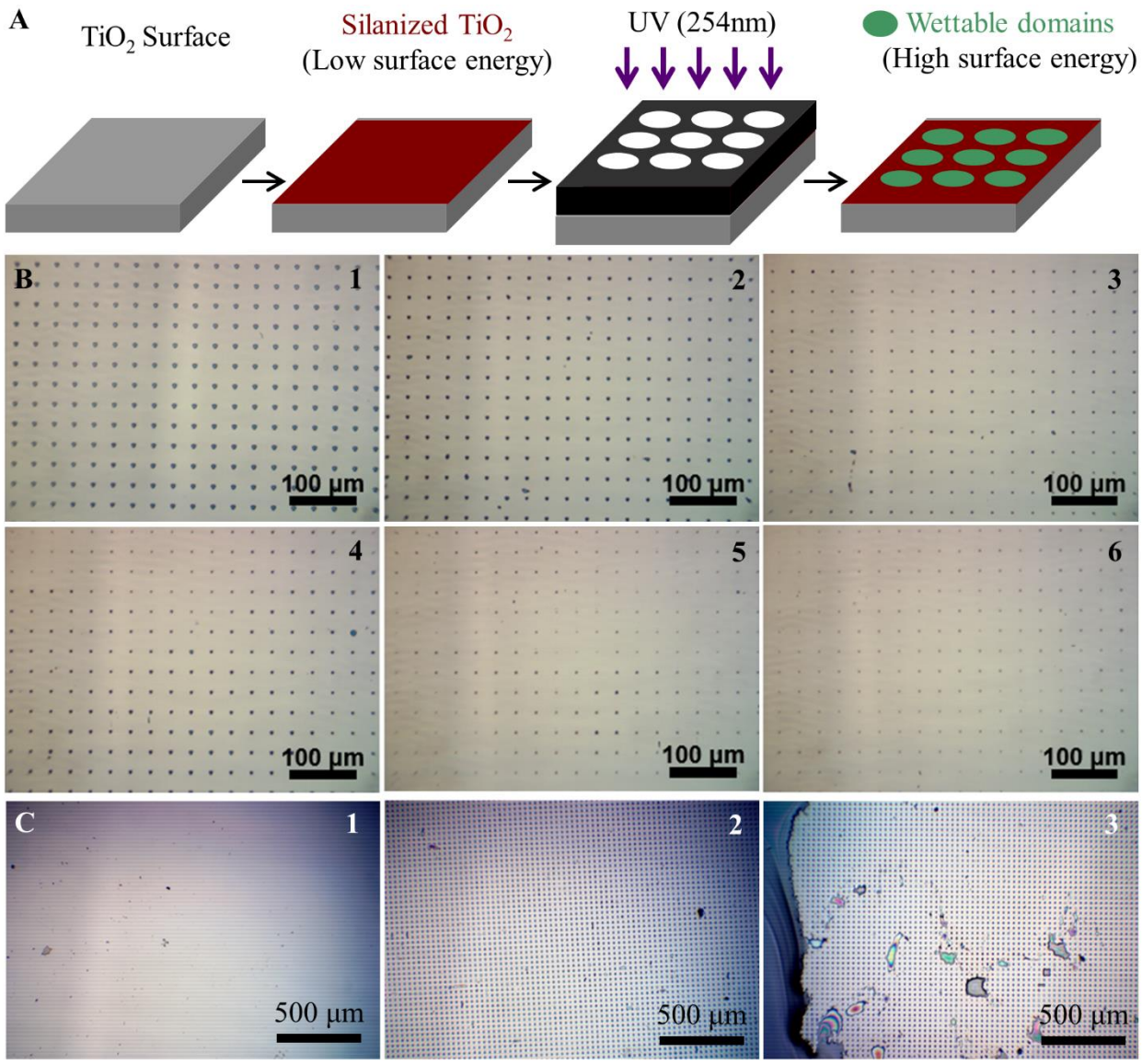

Figure 2.11: Simple WETS substrate fabrication method
A) Original fabrication method of WETS substrates where a silicon wafer was blanketed in 5 nm of TiO_2, silanized to create a non-wetting surface and then exposed to UV radiation through a quartz photomask to pattern discrete wettable domains in the non-wetting background. B) Repeated uses of the same WETS substrate, imaged with optical microscopy, showing the reduction in particle size as the wettable domains slowly revert to non-wetting over time. C) Optical microscopy images of the same WETS substrate imaged over time showing the increase in polymer filming on the surface due to flaws in the silanization of the non-wetting background.

In order to address these short comings, a new photolithography method (Figure 2.12A) was used which would enable WETS substrates to be reusable. This method would use a combination of lift off resist (LOR) and a standard photoresist, 1813, to pattern the wettable

domains, such that when the TiO_2 was deposited it formed discrete domains instead of blanketing the entire silicon wafer (Figure 2.12B). After the photoresist was removed, the substrate was silanized rendering the entire face non-wettable. Then the substrate was exposed to UV radiation which selectively removes the silane from only the TiO_2 domains and activates the domains to become wetting, while leaving the silanized silicon background unchanged. This substrate was now able to be reused as repeated UV exposure would re-activate the TiO_2 and smaller flaws in the silanization of the silicon background can be 'cleaned' as the UV radiation breaks down tiny polymer deposits that may collect there.

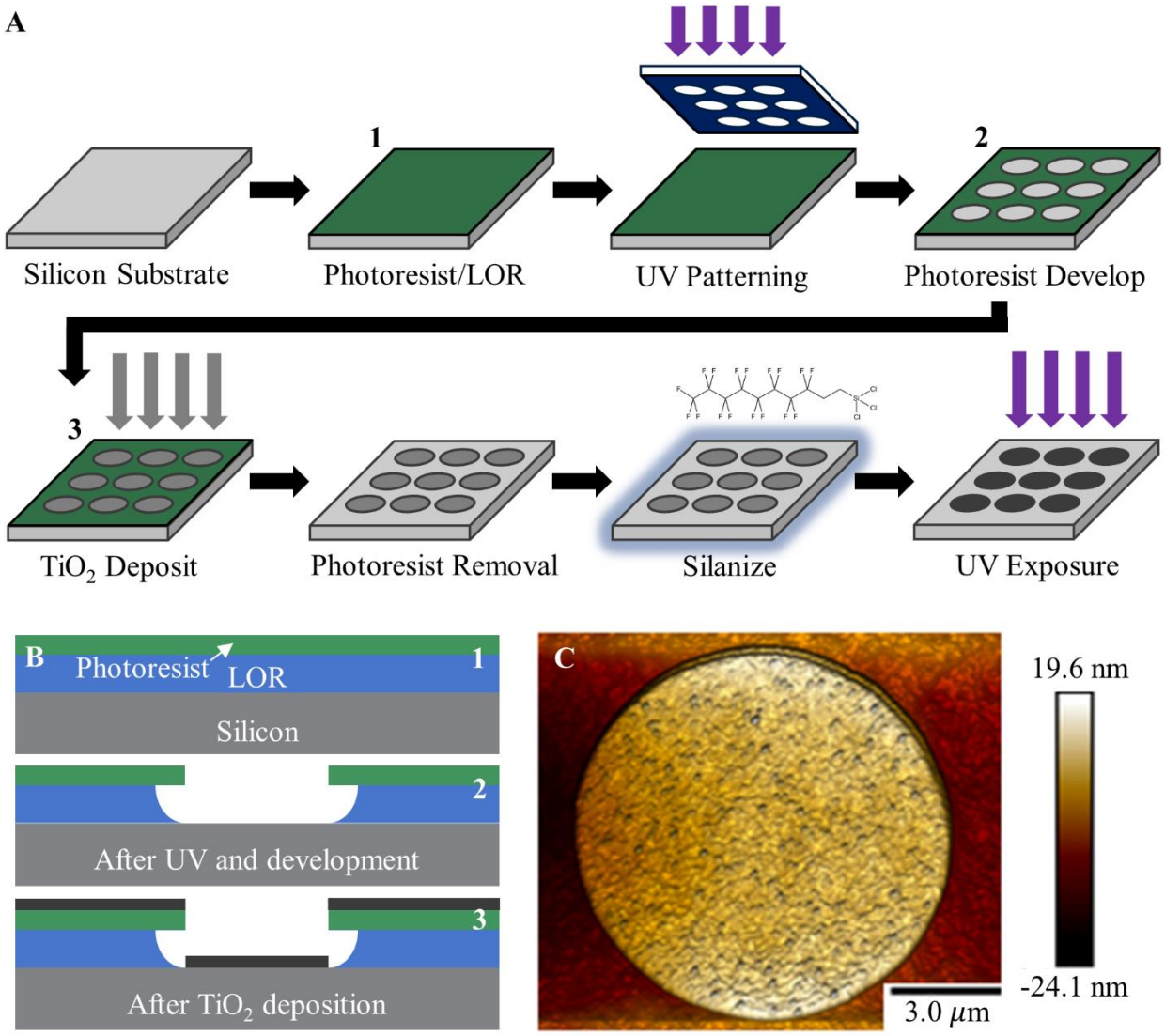

Figure 2.12: New photolithography method to fabricate WETS substrates with discrete TiO_2 domains
A) WETS substrate fabrication method using standard photolithography steps to create discrete TiO_2 domains using 1813 photoresist paired with LOR. The size and shape of the wettable domains were determined by the pattern on the quartz photomask which was used to pattern the photoresist. TiO_2 was deposited on the developed photoresist, and after removal of the photoresist the substrate is silanized. UV radiation selectively removes the non-wetting silane from the TiO_2 domains and makes the domains wettable. B) Cross-section schematic of the LOR/1813 combination used to enable the patterning of TiO_2 domains. Number 1, 2 and 3 correspond to steps labeled in (A). C) AFM scan of an individual, 10 nm tall TiO_2 domain.

With this new method, the WETS substrates were able to be used consistently for multiple uses (Figure 2.13), and were able to be cleaned with solvent washes and UV radiation between batches of particles.

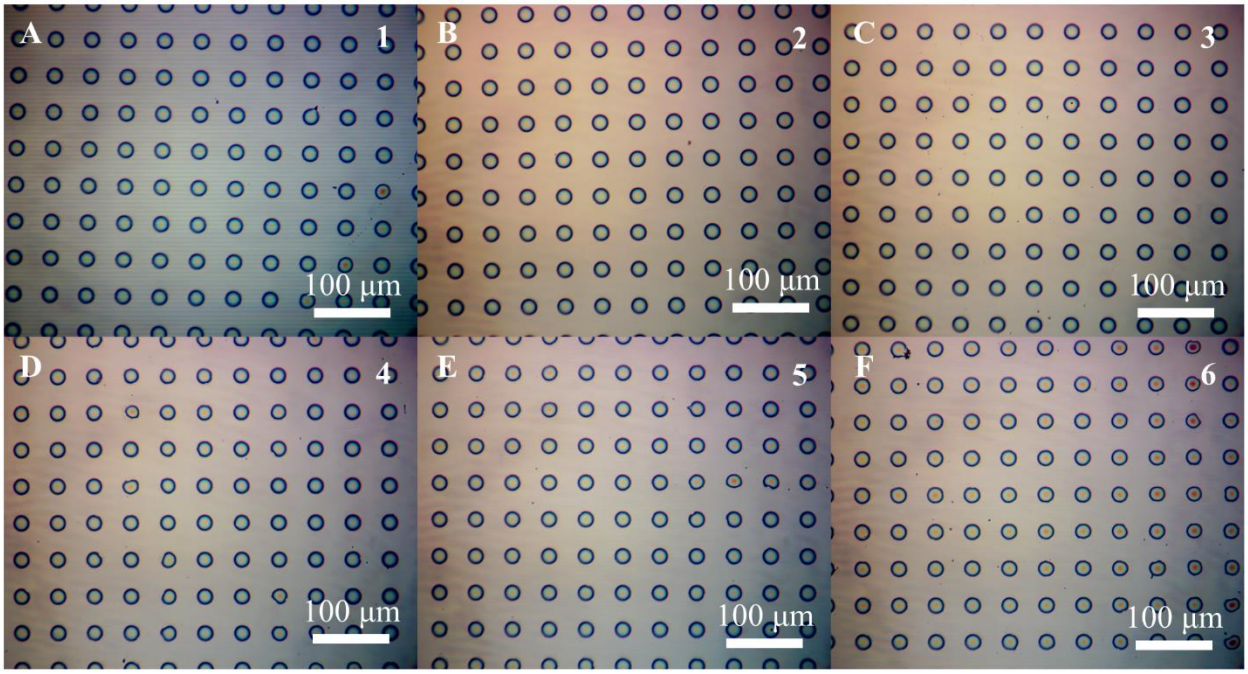

Figure 2.13: Optical images of particles on the new WETS substrates
A) A new WETS substrate with the release layer dip-coated. Successive B) second, C) third, D) fourth, E) fifth and F) sixth uses of the same WETS substrate with the release layer consistently the same size as the first use.

2.2.4.2 Increased Substrate Size

Production of WETS particles is based on the size of the WETS substrate and the density of the particle array on the substrate. Therefore, increasing the size of the substrate and decreasing

the center-to-center distance between wettable domains will increase the number of particles produced in each batch. Particles produced for characterization had originally been produced on substrates that were 1.0 – 2.5 cm^2 and were dip-coated in small glass vials or jars (Figure 2.14A) and were small enough to be accommodated in-house. In order to scale up to using an entire 4-inch silicon wafer, a larger dip-coating chamber had to be fabricated (Figure 2.14B) and several substrate processing steps were moved to a cleanroom as the equipment was able to accommodate the larger wafers. As a part of the scale-up testing, a 20 µm center-to-center photomask was purchased to uniformly pattern a 4-inch wafer. This increased the number of particles able to be produced due to the smaller center-to-center distance and the larger area of the photomask. Table 2.5 lists current in-house photomask patterns and the number of particles which could be patterned on its area. Additionally, 3 theoretical photomasks are listed as these were the next designs planned. Based on published methodologies, the number of nanoparticles delivered for a single condition in an *in vitro* cell study ranged from 10^7 to 10^{27} nanoparticles[83–86], and was ~10^{12} nanoparticles for my electrospray experiments in Chapter 3 and 4. Even with the theoretical, 1.5 µm center-to-center substrate (highest number of particles/substrate), the substrate would have to be dip-coated ~300 times to produce enough particles. This demonstrated that a larger increase in production than the single 4-inch wafer would be needed. Future routes to accomplish this can be done by either reducing the center-to-center spacing further, increasing the size of the wafer to 6 or 12 inches, developing a multiple substrate dip-coating apparatus or designing a roll to roll dip-coating set up similar to that of Liquidia[72].

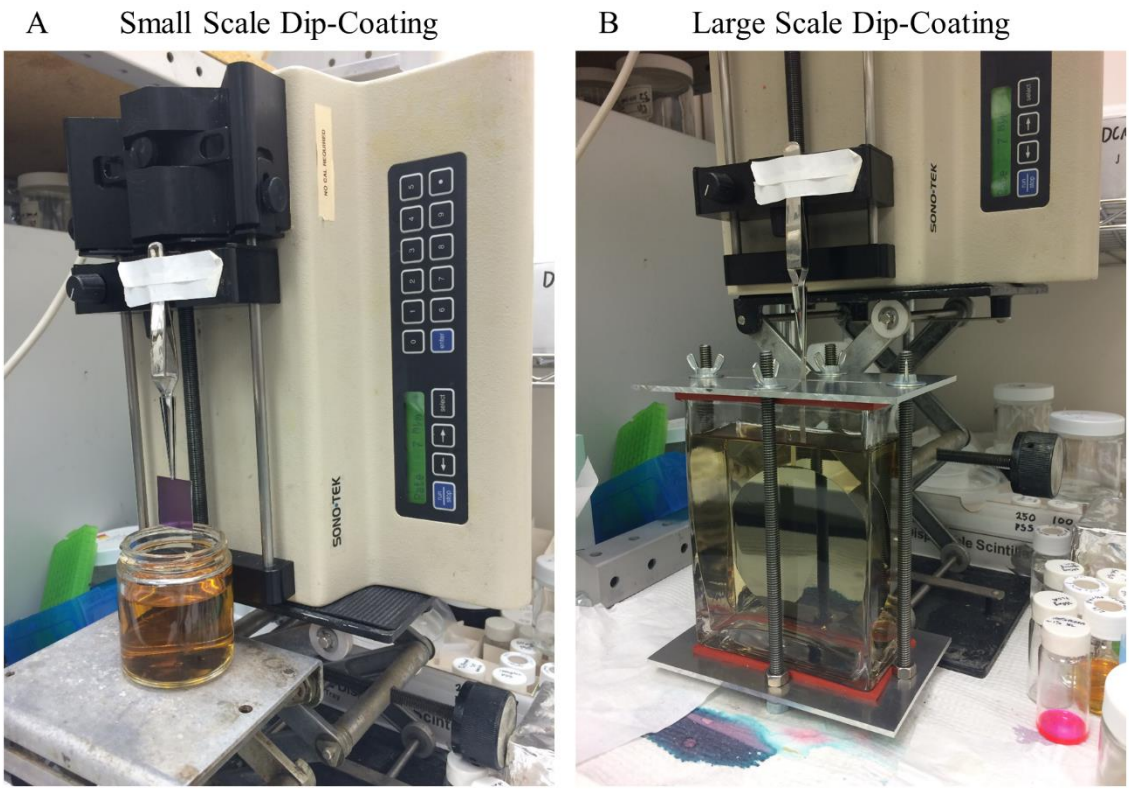

Figure 2.14: Small and large scale dip-coating set ups
A) Small scale dip-coating set up with a syringe pump to withdraw the WETS substrate from the polymer solution at a steady rate. The small substrate could fit in the glass jar which was used as the solution reservoir. B) Large scale dip-coating set up with the same syringe pump to set the withdrawal rate. The dip-coating chamber is a custom designed glass chamber which is large enough to accommodate a 4-inch WETS substrate.

Table 2.5: Photomask center-to-center spacing and particle yield

	Center-to-Center (µm)	**Particles / 2.5cm^2**	**Particles / 4-inch wafer**
In-house Photomasks	50	2.58×10^5	–
	45	3.19×10^5	–
	40	–	5.07×10^7
	30	7.17×10^5	–
	20	–	2.03×10^7
Theoretical	10	–	8.11×10^7
	5	–	3.24×10^8
	1.5	–	3.60×10^9

2.2.5 Nanoscale Fouling of Non-wettable Silane

The highly fluorinated silane which was chosen to form the non-wettable background displayed high contact angles for both aqueous and organic solvents as well as polymer solutions (Table 2.6). In addition, small scale substrates (1.0 – 2.5 cm^2) had been re-used up to 20 times with continued receding of the polymer solution from the non-wettable background during dip-coating.

Table 2.6: Advancing (θ_{Adv}) and receding (θ_{Rec}) contact angles for various liquids and polymer solutions on the non-wettable, fluorinated silane

Liquid	**Contact Angle**	
	$\boldsymbol{\theta_{Adv}}$ **(°)**	$\boldsymbol{\theta_{Rec}}$ **(°)**
Water	120	112
Dimethylformamide (DMF)	76	66
Toluene	72	62
Ethanol	50	38
Hexane	47	33
Acetone	62	47
Methanol	52	39
Isopropanol	56	42
Tetrahydrofuran (THF)	66	53
Chloroform	64	51
PSS – water	108	97
PS – toluene	72	58
PMMA – toluene	70	57
PMMA – DMF	73	60
PEGDA – DMF	78	68
PMMA – chloroform	58	42

However, it was found that when the substrate area was increased from 1.0 – 2.5 cm^2 to a full size 4-inch silicon wafer that the polymer solution would not recede fully from the substrate leaving behind a film of polymer (Figure 2.15A). AFM of the non-wettable background shows

nanoscale polymer fouling of the silane through an increase in roughness (Figure 2.15B-E). Additionally, when the substrate is submerged in a polymer solution for 5 minutes, there is a change in the contact angle, notably a large decrease when submerged in the PSS+H_2O solution (Table 2.7). Decreases in contact angle prevent the solution from receding from the substrate as the solution is more likely to pin which would enable evaporation of the solvent and the polymer would be left behind to form a film. It is suggested that the polymer solutions were able to recede from the small-scale substrates despite the nanoscale fouling because they were on the same length scale as the capillary lengths (l_c) of the polymer solutions, roughly $2l_c$. This would enable cohesion forces to assist in the receding of the solution from the edge of the substrate where with the 4-inch substrate, the width of the substrate was much larger than $2l_c$. This is supported by the polymer film forming ~l_c inside the edge of the 4-inch wafer (Figure 2.15A) and receding between the edge of the wafer and ~l_c. Furthermore, silicon wafers fabricated as 4-inch substrates that were broken down into 1.0 – 2.5 cm^2 substrates and dip-coated, did not exhibit polymer filming as the solution receded from the substrate.

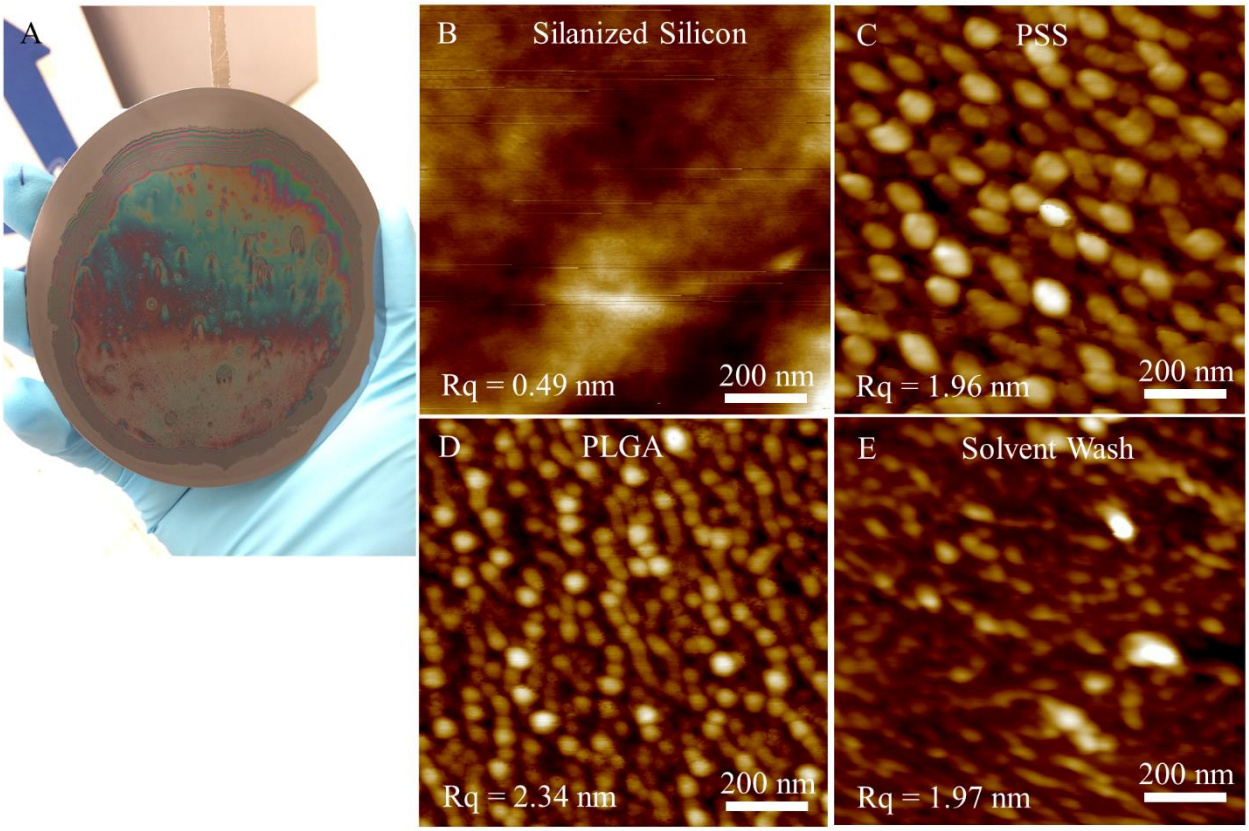

Figure 2.15: Polymer fouling of WETS substrates
A) Picture of a 4-inch WETS substrate where the polymer solution did not recede from the wettable background and formed a film on the substrate. AFM scans of B) the silanized, non-wettable background, C) PSS nanoscale fouling of the non-wettable background after dip-coating, D) PLGA nanoscale fouling of the non-wettable background after PSS and PLGA dip-coating, and E) residual polymer fouling in the non-wettable background after washing the substrate with solvents for PSS and PLGA.

Table 2.7: Changes in contact angle after submerging in various polymer solutions for 5 minutes

Polymer Solution	**Initial Contact Angle**		**Change in Contact Angle**	
	θ_{Adv} (°)	θ_{Rec} (°)	θ_{Adv} (°)	θ_{Rec} (°)
PLGA + Ethyl Acetate	110	74	0	-9
PLGA + Chloroform	110	71	+1	-11
PLGA + Dichloromethane	113	85	+4	+2
PSS + H_2O	99	58	-10	-25

2.3 Conclusions

The WETS method was shown as a viable technique to make multiphasic spherical and non-spherical particles in a large range of sizes and shapes. This versatility is ideal for fabricating particles for a systematic study of how particle properties impact particle behavior *in vivo*. The key factor of the WETS method is the independent control of each property that enables direct comparison between size, shape, and chemistry. Polymer solutions and dip-coating parameters can be adjusted such that particles with exact specifications can be fabricated as predictive models have been developed for both spherical and non-spherical models. Additionally, temperature stimulated particles could also be employed. Nanoparticle fabrication has been demonstrated by using a stepper to reduce the size of the wettable domain on the WETS substrate, and protocols have been developed to accommodate a reusable 4-inch substrate for increased production. However, due to the discovery of nanoscale fouling which renders the 4-inch substrate unusable, investigations into alternate non-wetting silanes, such as 1,3-PDMS, need to be conducted to allow for scaling up of the WETS system. Scale-up of WETS particle production will need to continue past the expansion to a single 4-inch substrate as even with a theoretical center-to-center spacing of 1.5 μm, the substrate would have to be dip-coated hundreds of times. Future work will need to focus on continued scale up by employing larger substrates, multiple substrate dip-coating or another form of automation.

2.4 Materials and Methods

2.4.1 Materials

Heptadecafluoro-1,1,2,2-tetrahydrodecyl)trichlorosilane (HDFTS) was purchased from Gelest Inc. Poly(vinylidene fluoride) (PVDF, Mw = 275kDa), polystyrene (PS, Mw = 1.2kDA, 45kDa and 190kDa), SU-8 (2010), poly(sodium 4-styrenesulfonate) (PSS, Mw = 70 kDa),

poly(vinyl acetate) (PVAc, $M_w \approx 25$ kDa), poly(methyl methacrylate) (PMMA, $M_w \approx 25$ kDa), poly(ethyleneglycol)diacrylate (PEGDA, Mw = 700Da), poly(4-vinylphenol) (PVP, $M_w = 25$ kDa), Poly(*D,L*-lactide-co-glycolide) (PLGA, 24-38 kDa, lactide:glycolide 50:50, acid terminated), poly(allylaminehydrochloride) (PAH, $M_w = 15$ kDa). Rhodamine B, fluorescein isothiocyanate isomer I (FITC), 4', poly[tris(2,5-bis(hexyloxy)-1,4-phenylenevinylene)-*alt*-(1,3-phenylenevinylene)] (PTDPV, blue), 6-diamidino-2-phenylindole dihydrochloride (DAPI). Dimethylformamide (DMF), toluene, ethylene glycol, heptane, ethanol, chloroform propylene glycol monomethyl ether acetate (PGMEA) and perfluorodecalin (PFD) were purchased from Sigma-Aldrich. Ferrofluid (EMG 304) was purchased from Ferrotec. Silicon wafers were obtained from the Lurie Nanofabrication Facility at the University of Michigan.

2.4.2 WETS Substrate Fabrication

2.4.2.1 Blanket TiO_2 Method

A ~5 nm thin film of titanium dioxide (TiO_2) was deposited on to a 4-inch silicon wafer through physical vapor deposition. The TiO_2 coated silicon was then plasma treated for 15 minutes and then silanized with HDFTS through chemical vapor deposition at 100°C for 30 minutes rendering the surface non-wettable. To create patterned wettable domains, the silanized TiO_2 surfaces were radiated with ultraviolet light (UV, 254 nm) for 90-120 minutes through quartz photomasks which were patterned with the wettable domain size and shape. The resulting template had a non-wetting background and patterned wettable domains with controlled geometry and spacing.

2.4.2.2 Discrete TiO_2 Lithography Method

The 4-inch silicon wafer was cleaned with a plasma strip for 6 minutes and then coated with 0.9 μm of lift-off resist (LOR) followed by 1813 with baking between each step. The

photoresist was then UV exposed through a quartz mask patterned with the wettable domain size and shape. Following UV exposure, the photoresist was developed so that the 1813 slightly over hangs the LOR underneath of it. The wafer was then gently cleaned with a plasma descum step for 20 seconds before 10 nm of TiO_2 was deposited with physical vapor deposition. The photoresist was then lifted off and the entire wafer cleaned again with a 6-minute plasma strip. The now activated substrate was silanized with HDFTS at 120°C for 2 hours rendering the entire substrate non-wettable. The HDFTS was then cleaved from the TiO_2, wettable domains by UV radiation for 45 minutes reversing the domains to be completely wettable.

2.4.2.3 Stepper Lithography Method

A plasma cleaned 4-inch silicon wafer was coated in 3 μm of SPR 220 photoresist and baked. The photoresist was then patterned with UV radiation through a quartz masking using a stepper (GCA AS200 Autostep) to create an array of 700 nm discrete domains following development. 15 nm of TiO_2 was then deposited with physical vapor deposition and the photoresist was lifted off. The substrate was then silanized with HDFTS and UV exposed the same as the TiO_2 discrete method listed previously to form a patterned wettability substrate.

2.4.2.4 Block Copolymer Lithography Method

Block copolymer lithography was carried out using an asymmetric block copolymer, polystyrene-block poly(methyl methacrylate) (PS-b-PMMA, MW_{PS} = 46 kDa, MW_{PMMA}= 21 kDA). After thermal annealing and the selective plasma etching of PMMA, PS-b-PMMA formed cylindrical nanostructures with 25 nm diameters in a hexagonally packed array on a 4-inch silicon wafer. 5 nm of TiO_2 was then deposited with physical vapor deposition and the block copolymer removed with a solvent wash. The substrate was then silanized with HDFTS and UV exposed the same as the TiO_2 discrete method listed previously to form a patterned wettability substrate.

2.4.3 Particle Fabrication Method

2.4.3.1 Dip-coating

15 wt% polymer solutions included PSS-water, PVDF-DMF, and PS-toluene. 25 wt% PVP-ethanol, 2.5 wt% PAH-water, 2.5 wt% PSS-water and 10-55 wt% PLGA-chloroform were also used. All solutions were dip-coated using a KD Scientific syringe pump at a constant dip-coating velocity of 0.1 to 1 cm/s.

2.4.3.2 Particle Harvesting

Particles were collected from the WETS substrate by holding the substrate vertically over a collection vial and gently washing with the release layer solvent (generally water). With the dissolution of the particles, the solvent droplet would recede down and off the substrate taking the released particles with it. Harvesting efficiency can be check with optical microscopy.

2.4.3.3 Particle Reconfiguration

Shape reconfiguration of non-spherical particles was carried out by heating a particle-water dispersion above the glass transition temperatures (T_g) of all polymers comprising the particle. In case of particles that have a T_g higher than 100°C a 1:1 glycerol-water mixture was used. Spherical particles can then be collected after particle sedimentation with centrifugation or through water evaporation.

2.4.4 Characterization Methods

2.4.4.1 Contact Angle Measurements

Contact angle was measured using a Ram-Hart 200-F1 goniometer. Advancing contact angle was measured by expelling 2-10 μL of liquid onto a surface and the receding contact angle was measured by removing 2-10 μL of liquid from a surface with a 2 mL micrometer syringe (Gilmont). At least 3 measurements were taken for each sample and typical error was ± 2°.

2.4.4.2 Optical Microscopy

Optical microscopy was conducted with a VistaVision VWR optical microscope.

2.4.4.3 Atomic Force Microscopy (AFM)

Tapping mode AFM was conducted using a Veeco Innova with Veeco TESPA tips and Hi Res C probes.

2.4.4.4 Fluorescent Microscopy

Fluorescent microscopy was carried out with an Olympus BX 51 microscope. Confocal laser scanning microscopy was conducted with a Nikon A1 Confocal with lasers: 405 nm, 488 nm, and 533 nm.

2.4.4.5 Scanning Electron Microscopy (SEM)

SEM imaging was done with a Hitachi SU8000 at 2 or 5kV after gold coating the particles.

Chapter 3: Co-Delivery Nanoparticles to Target Ovarian Cancer Stem Cells and Platelet-Derived Growth Factor Mediated Signaling from Mesenchymal Stem Cells

3.1 Introduction

3.1.1 Cancer Stem Cells Show Increased Chemoresistance, Metastasis and ALDH Expression Due to PDGF Signaling with Mesenchymal Stem Cells

Ovarian cancer stem cells (CSC) have been linked to increased chemoresistance, metastasis and proliferation, and are thought to be the main driver in patient relapse following clinical treatment[6–8,20,87,88]. CSC have been identified to have increased aldehyde dehydrogenases (ALDH) activity and high CD133 expression, and detection of these cells is a predictor of poor patient outcomes[89–94]. In the ovarian cancer microenvironment, CSC interact dynamically with other cells, some of which become CSC-supportive including mesenchymal stem cells (MSC)[9,95]. MSC reprogramming arises from bi-directional signaling between CSC and MSC through IL-6, SDF-1, TGF-β, BMP2, BMP4, CCL5 and platelet-derived growth factor (PDGF)[3,9,15,18,95,96]. Previously, PDGF signaling between CSC and MSC has been shown to increase CSC platinum resistance, migration, epithelial to mesenchymal (EMT) markers and ALDH expression[3]. Additionally, sunitinib, a tyrosine kinase inhibitor which interrupts CSC-MSC communication through PDGF, was shown to negate the increase in platinum resistance, and was suggested as a potential therapy to also reduce ALDH expression, EMT markers and migration potential[3].

3.1.2 Nanoparticles for Co-delivery of Sunitinib and Paclitaxel

Encapsulation of chemotherapeutics in a polymer nanoparticle increases the solubility, circulation and targeting of the delivered drugs. Paclitaxel, an antimicrotuble ovarian cancer therapy, has previously been encapsulated in a nanoparticle and showed increased solubility and cytoxicity[84,97–99]. Sunitinib has also been delivered as a nanoformulation for cancer therapy and found to be effective, but it has not been studied as extensively as paclitaxel[100–102]. Sunitinib and paclitaxel have been delivered together in a 3 patient case study, where paclitaxel was delivered in the form of an albumin nanoparticle and sunitinib was delivered as a free drug. Improvements in all 3 lung cancer patients were observed in the form of reduced tumor mass and a lessening in symptoms with co-delivery[103]. Co-delivery where both drugs were encapsulated in the nanoparticle have generally been found to be more effective, and the first co-delivery formulation was approved by the FDA in 2017[29]. In this work, a polymer nanoparticle which encapsulates both paclitaxel and sunitinib will be fabricated and characterized. In addition, the effectiveness of treating a co-culture of ovarian CSC and MSC with paclitaxel and sunitinib will be studied.

3.2 Results and Discussion

3.2.1 Nanoparticle Fabrication and Characterization

3.2.1.1 Electrospray Parameter Determination

Polymer nanoparticles made of poly (D,L-lactide-co-glycolide) (PLGA) were fabricated using an electrospray system (Figure 3.1) where a syringe pump was placed on top of an aluminum frame such that the syringe would point down towards the collection plate. A voltage was applied to the syringe needle and the collection plate was grounded.

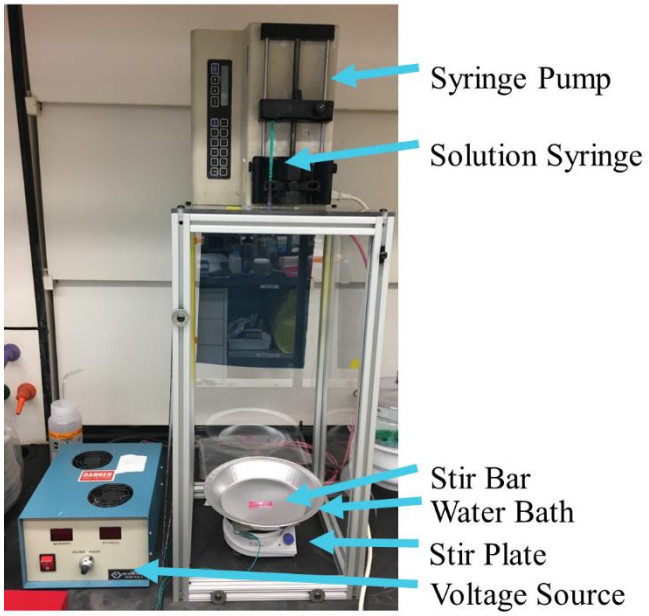

Figure 3.1: Nanoparticle Electrospray set up

Identification of the spray solution was carried out through a systematic study of first the solvents and then the spray conditions in order to determine a formulation, and corresponding parameters, that results in a spherical nanoparticle with an average diameter of 200 nm or less. Various solvent combinations were identified from the literature and tested with 2 vol% PLGA and a flow rate of 0.1 mL/hr. Particles were sprayed onto aluminum pans and imaged with scanning electron microscopy (SEM) to evaluate size and morphology (Figure 3.2). Solvents used include dimethylformamide (DMF), acetonitrile (ACN), chloroform, dimethyl sulfoxide (DMSO), triethylammonium formate (TEAF), 2,2,2-trifluoroethanol (TFE) and sodium chloride (NaCl). Table 3.1 lists the associated solvents and nanoparticle diameters and standard deviations from Figure 3.2. From this test, a solvent combination of 25% ACN, 75% DMF and 10 μL TEAF (Figure 3.2B), which results in uniform, 143 ± 27 nm nanoparticles, was chosen as the best formulation and used as the ‘standard’ recipe for further experiments.

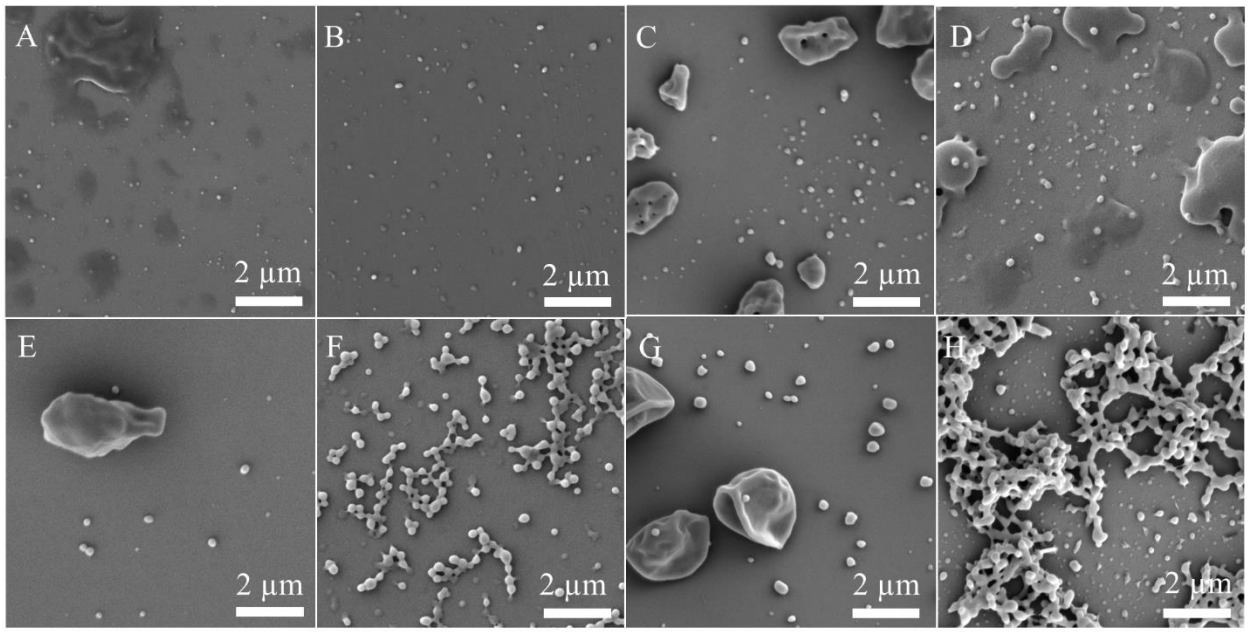

Figure 3.2: SEM images of PLGA nanoparticles with various solvent ratios
A) 5% TEAF and 95% DMF, B) 25% ACN, 75% DMF and 10 µL TEAF, C) 25% TFE and 75% DMF, D) 50% ACN and 50% DMF, E) 25% chloroform and 75% DMF, F) 25% ACN, 75% DMSO and 10 µL TEAF, G) 50% chloroform and 50% DMF, H) 1% NaCl and 99% DMSO

Table 3.1: Solution parameters of PLGA nanoparticles and their diameters

Figure 3.2 Panel	**Solvent (vol%)**	**Voltage (kV)**	**Diameter (nm)**
A	5% TEAF and 95% DMF	7.5	124 ± 20
B	25% ACN, 75% DMF and 10 µL TEAF	8.0	143 ± 27
C	25% TFE and 75% DMF	8.0	195 ± 30
D	50% ACN and 50% DMF	10.0	198 ± 55
E	25% chloroform and 75% DMF	4.5	225 ± 44
F	25% ACN, 75% DMSO, 10 µL TEAF	8.5	250 ± 66
G	50% chloroform and 50% DMF	6.0	269 ± 94
H	1% NaCl and 99% DMSO	6.0	–

The next systematic study included adjustments in the electrospray set up: the addition of an air flow to aid in the nanoparticle drying and the reduction of the flow rate by half to 50 µL/hr

which was hypothesized to reduce the overall nanoparticle size. The air flow consisted of compressed air which entered the spray chamber next to the syringe and flowed down towards the collection plate. Adjustments in the electrospray solution included a reduction in ACN, TEAF and PLGA. Figure 3.3 shows SEM images of the nanoparticles sprayed with the various conditions and the measured nanoparticle diameters and standard deviations. The reduction in ACN by 50 μL from 255 μL to 205 μL did not seem to have an impact on the size of the nanoparticles, 171 ± 54 nm vs 169 ± 48 nm. However, more nanoparticles that had not fully dried were seen in the form of dark, flat disks on the collection pan indicating that 255 μL ACN is needed to increase the rate of evaporation of the solvent. With the reduction in TEAF from 10 μL to 5 μL or 0 μL, the size of the nanoparticles increases to 259 ± 92 nm and 319 ± 398 nm, respectively. Reducing the PLGA vol% from 2 vol% to 1.5 vol% did not seem to have a large impact of the size or morphology of the particles (162 ± 54 nm). When comparing nanoparticles fabricated with the addition of an air flow to those from the standard electrospray set up, there is an increase in the presence of non-spherical particles suggesting that the air flow distorts the spray droplets as they fly towards the collection plate. Reducing the flow rate to 50 μL/hr, which is half that of the standard set up, does not greatly impact particle size (170 ± 40 nm), however, it does double the amount of time needed to fabricate the same number of nanoparticles. From this the standard electrospray solution (25% ACN, 75% DMF and 10 μL TEAF) and set up (no air flow, 0.1 mL/hr solution flow rate) (Figure 3.3A) were identified as the best parameters and used for further experiments due to the production of dry, spherical nanoparticles with an average diameter less than 200 nm.

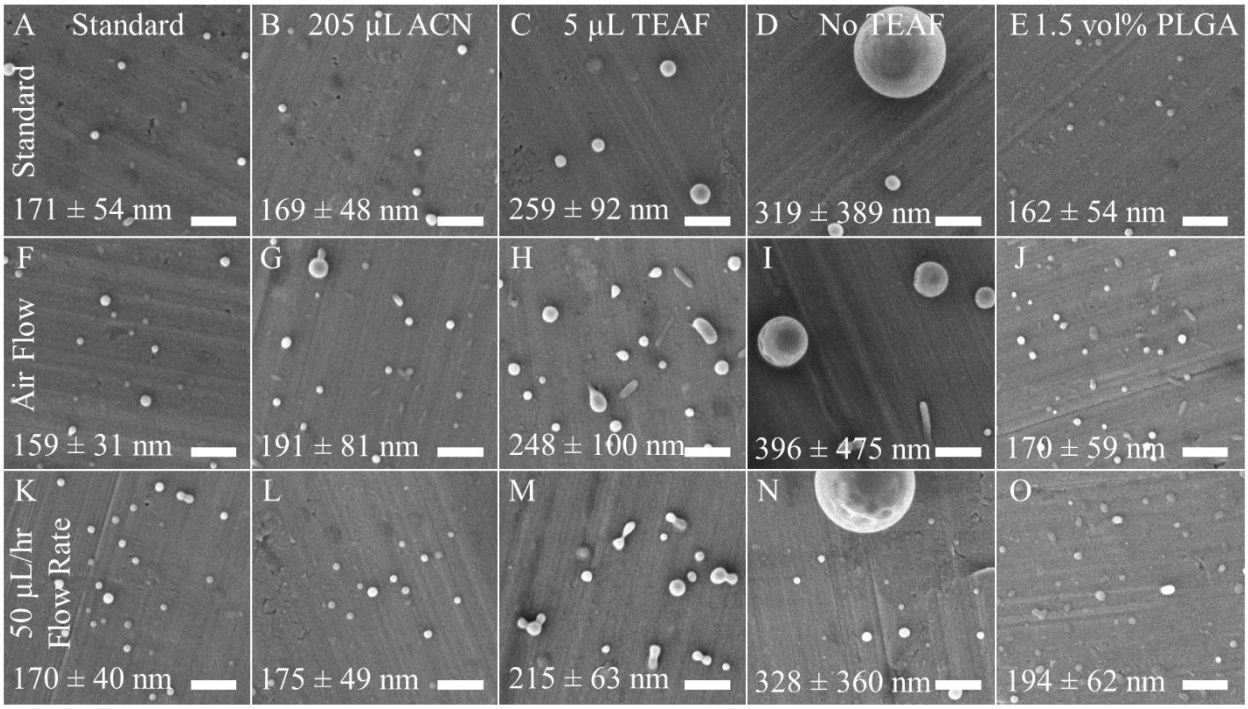

Figure 3.3: SEM images of alterations to the electrospray solution and set up
A) Standard electrospray solution (25% ACN, 75% DMF and 10 µL TEAF) with the standard electrospray set up (no air flow, solution flow rate of 100 µL/hr, B) a reduction of 50 µL of ACN to 205 µL with the standard electrospray set up, C) a 50% reduction of TEAF to 5 µL and the standard electrospray set up, D) no TEAF and the standard electrospray set up, E) 1.5 vol% PLGA instead of 2 vol% and the standard electrospray set up, F) the standard electrospray solution with added air flow during spraying, G) reduced ACN and added air flow, H) reduced TEAF and added air flow, I) no TEAF and added air flow, J) reduced vol% PLGA and added air flow, K) the standard electrospray solution sprayed at 50 µL/hr instead of 100 µL/hr, L) reduced ACN and reduced flow rate during spraying, M) reduced TEAF and reduced flow rate, N) no TEAF and reduced flow rate, O) reduced vol% PLGA and reduced flow rate. Scale bar is 1 µm.

3.2.1.2 Nanoparticle Collection

Nanoparticle collection was carried out in either a ‘water bath’ (stirring 0.01% Tween 20 and water solution) or onto an aluminum pan for a ‘dry’ collection. After a dry collection, the nanoparticles were harvested by scraping the particles off the surface of the pan with a plastic razor blade. Scraping was done within a puddle of ~5 mL 0.01% Tween 20 which would collect the particles removed from the pan. The puddle could then be scraped around the surface of the pan and pipetted off into a centrifuge tube to consolidate repeated scrapings of the same pan. For a water bath collection, once the electrospray is done, the particle suspension in the pan would be

poured off into a centrifuge tube. From this point, both the water bath and dry collection process were the same. The particle suspension in the centrifuge tube was probe sonicated to break up aggregates and then the suspension was poured through a 40 μm filter into a new centrifuge tube. The suspension was centrifuged for 15 minutes at 10,000 x g to pellet particles that are larger than 1 μm and the supernatant was kept and centrifuged again for 60 minutes at 10,000 x g to pellet the nanoparticles. The supernatant was removed, and the nanoparticle pellet was resuspended in either water or cell medium. If there were multiple tubes for one sample, the particles were resuspended, combined, pelleted, and then resuspended a final time.

Evaluation of the collection methods showed that for dry collection, scraping the pans was effective in removing all the nanoparticles from the surface (Figure 3.4A, B). However, this method was very labor and time intensive, and the water bath collection method removed the intermediate step of scraping all the collection pans multiple times. Particles collected with the water bath were centrifuge sorted and then drop casted onto a silicon chip for SEM imaging as they could not be imaged on the pan. The drop-casted particles (Figure 3.4C) were a mix of particles and short fibers. Investigation of the fiber's origin proved that they were not electrospun as the morphology of electrospun fibers was very different (Figure 3.4D) and only rarely seen in an extreme condition of high drug loading when dry collected. Dry collection of particles showed that some of the larger droplets would not be fully dry when they impact the collection pan, and by extension the water bath. In the case of the dry pan, a wet polymer solution droplet would dry as a polymer film on the collection pan (Figure 3.4E). However, in the case of the stirring water bath, the solvents (DMF and ACN) were water soluble and would diffuse out into the water bath leaving behind the polymer which was not water soluble. This diffusion was not instantaneous, and before the solvents diffuse completely, the water current from the stir bar was hypothesized to

elongate the polymer solution droplet. This elongated solution droplet then resulted in a fiber shaped polymer particle upon complete evaporation of the solvents, in addition to the spherical nanoparticles which were formed from completely evaporated polymer solution droplets (Figure 3.4F). From this, the dry collection method was used to collect nanoparticles to ensure spherical nanoparticles.

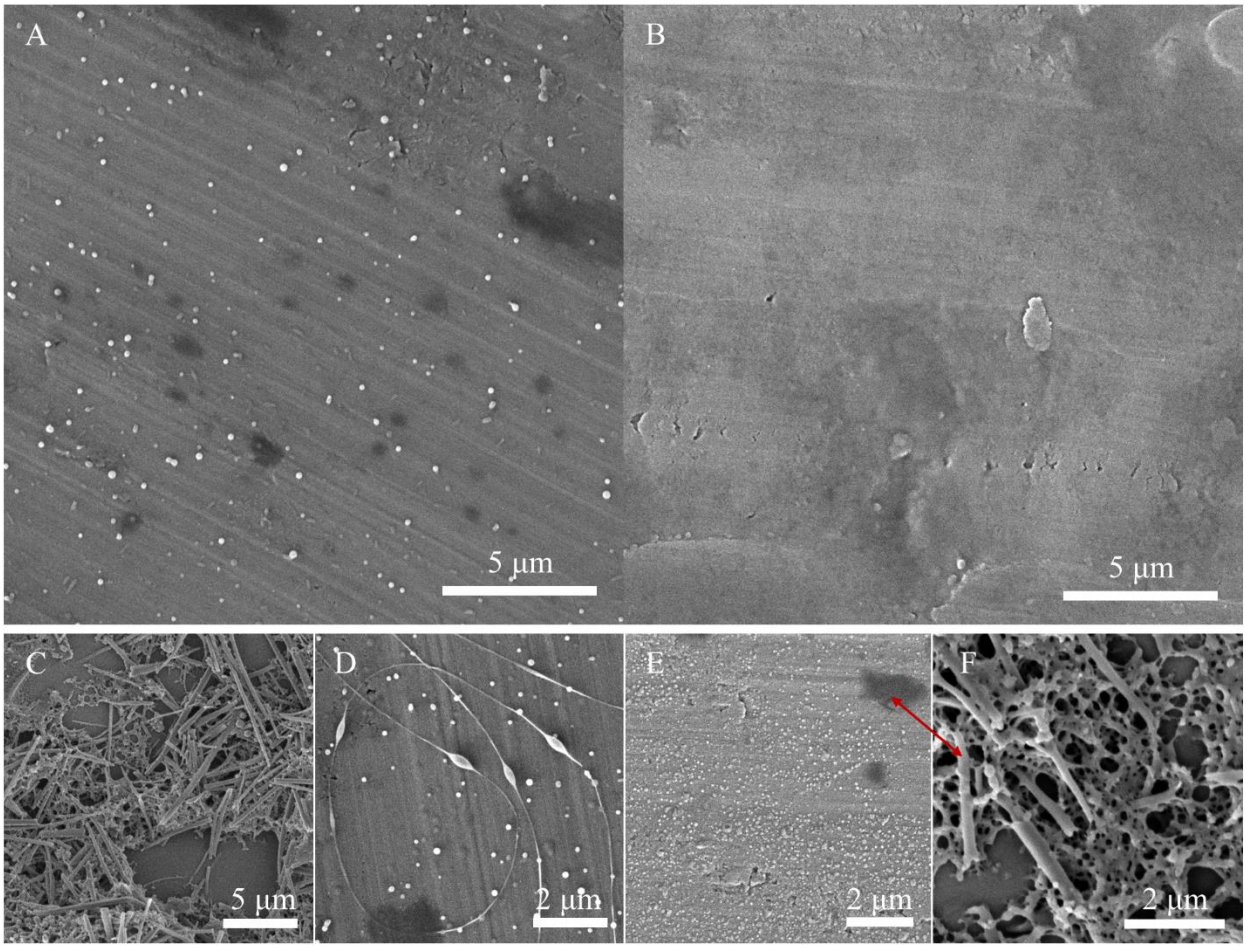

Figure 3.4: SEM images of nanoparticles from the dry and water bath collection methods
A) Nanoparticles on an aluminum pan before collection. B) Image of an aluminum pan after scraping to collect the nanoparticles. C) Drop casted particles that were collected in a water bath. D) Electrospun beaded nanofiber fabricated with a high loading of paclitaxel in an extreme condition. E) Nanoparticles collected dry on an aluminum pan with two polymer films which were made from larger wet droplets that dried on the pan. The red arrow indicates that the films from dry collection may result in F) a fiber-like particle when they impact the stirring water bath instead of the dry pan.

3.2.1.3 Drug Loaded Nanoparticle Characterization

Drug loaded nanoparticles were fabricated by adding powder drug to the electrospray solution and balancing the volume percent by reducing the amount of PLGA in the solution. Drug solutions were then sprayed with the same standard procedure as drug-free solutions and were dry collected to avoid the large fiber-like particles. Figure 3.5A-D show SEM images of control nanoparticles and drug loaded nanoparticles with diameters 100-150 nm. The particles were then collected from the aluminum pans, resuspended in 0.01% Tween 20 in water, centrifuge sorted and then quantified with nanoparticle tracking analysis (NTA). Hydrodynamic diameter was quantified by NTA and the histogram was plotted with the average indicated with a vertical dashed line (Figure 3.5E-H). Even with drug loading, the nanoparticles were less than 200 nm, and variation between the type of nanoparticles was within the range of error. The concentration of the nanoparticle suspensions was also measured with NTA and with the known volume of the suspension, the total number of nanoparticles fabricated with 3 batches was calculated (Table 3.2). Drug loading was done by pelleting a known number of nanoparticles, extracting the drug with ACN and then measuring the amount of drug with liquid chromatography-mass spectrometry (LCMS) as compared to known calibration curves (Figure 3.6). Table 3.2 lists all the data for the nanoparticles and the number of particles fabricated from the compilation of 3 batches and the associated drug loading. Based on the number of particles produced and their drug loading, it is estimated that it would take 746 hours (~4.4 weeks) of non-stop electrospraying to accumulate enough nanoparticles to conduct one cell study replicate. Due to this, nanoparticle cell studies were not conducted at this time as a major scale up in production (construction of ~7 more electrospray stations) would be required. Additionally, drug loading could possibly be improved by increasing the amount of initial drug in the electrospray solution, however this increase will not be linear, and

could eventually lead to fiber formation in paclitaxel loaded particles as seen in Figure 3.4D, and the addition of more drug would be very expensive.

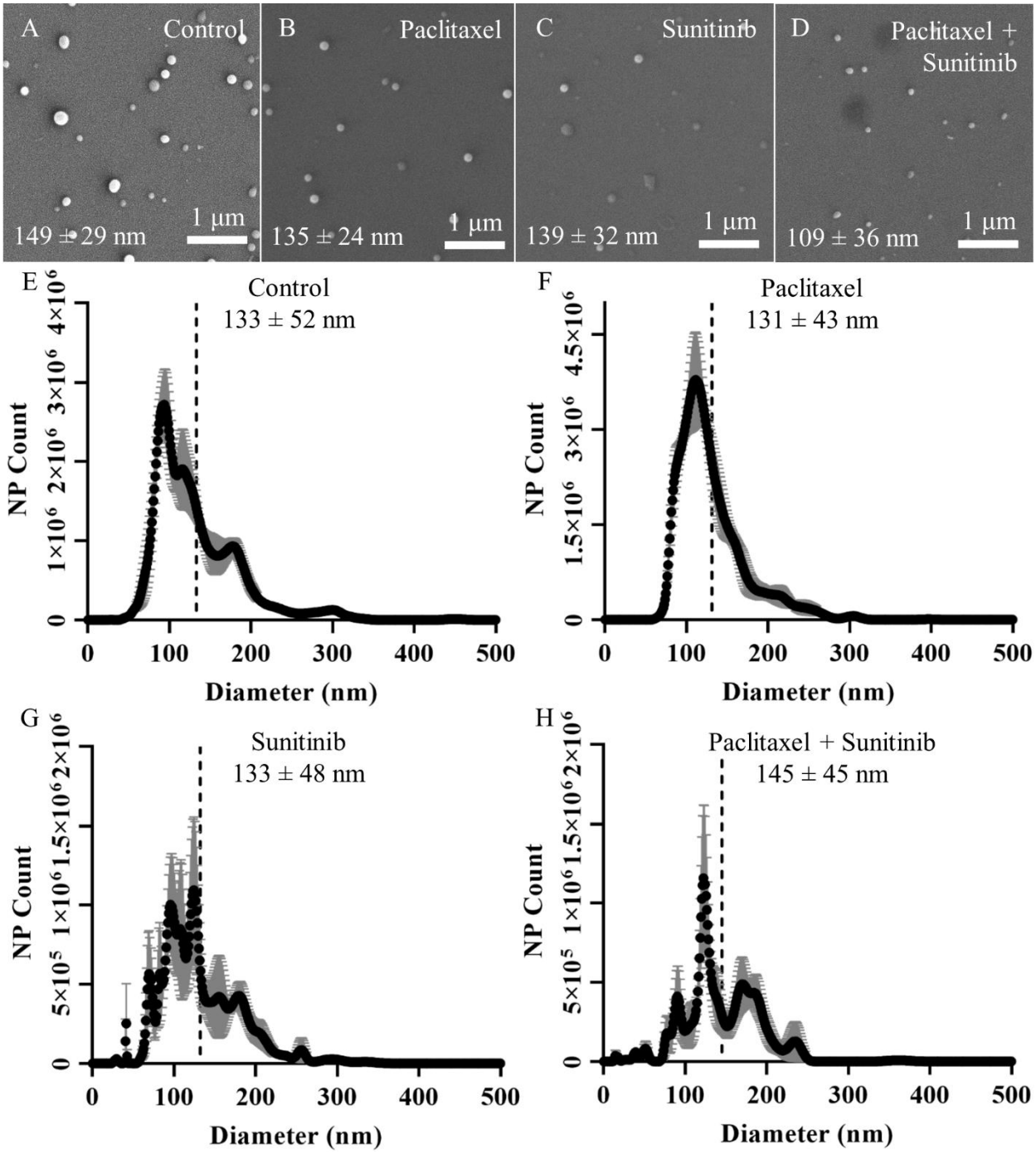

Figure 3.5: Size characterization of control and drug loaded nanoparticles with SEM and NTA SEM images and measurements of A) control nanoparticles, B) paclitaxel loaded nanoparticles, C) sunitinib loaded nanoparticles and D) co-delivery paclitaxel and sunitinib nanoparticles. NTA size histograms, with vertical lines indicating the average, of E) control nanoparticles, F) paclitaxel

loaded nanoparticles, G) sunitinib loaded nanoparticles and H) co-delivery paclitaxel and sunitinib nanoparticles.

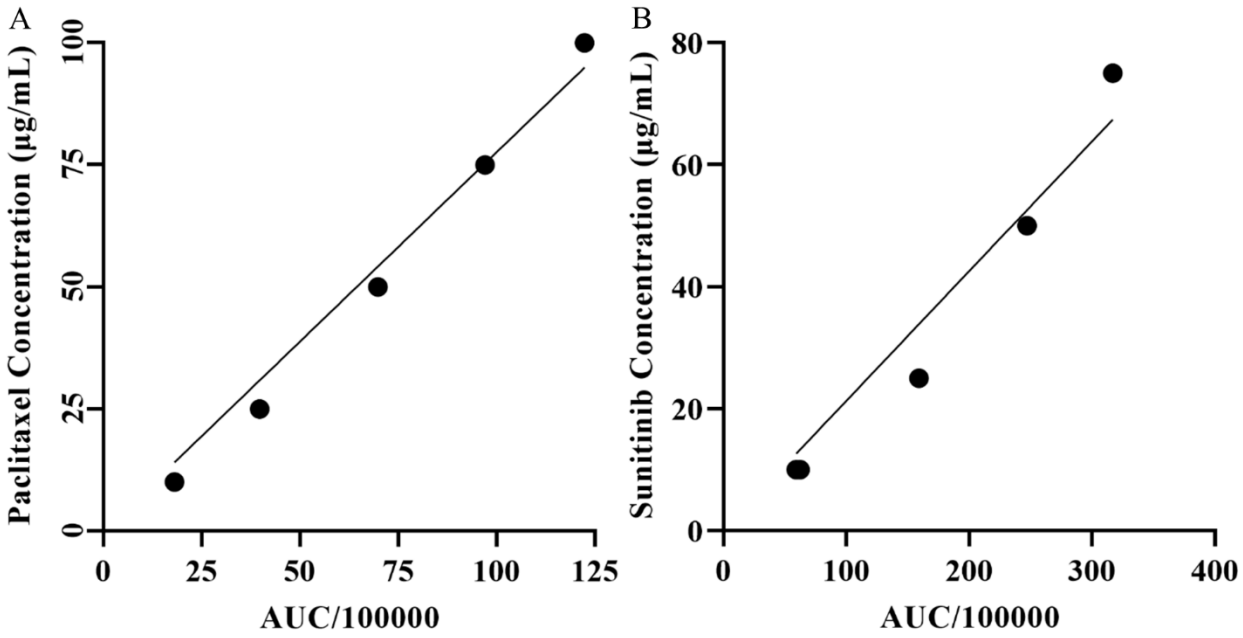

Figure 3.6: LCMS calibration curves of known standards
Calibration curves of known standards for A) paclitaxel and B) sunitinib.

Table 3.2: Compilation of all characterization data for control and drug loaded nanoparticles

Nanoparticle	SEM Diameter (nm)	NTA Diameter (nm)	NTA Nanoparticle Count	Drug Loading (µg/NP)
Control	149 ± 29	133 ± 52	2.0×10^{10}	–
Paclitaxel	135 ± 24	131 ± 43	2.3×10^{10}	3.4×10^{-10}
Sunitinib	139 ± 32	133 ± 48	7.3×10^{10}	5.6×10^{-11}
Paclitaxel + Sunitinib	109 ± 36	145 ± 45	5.0×10^{10}	1.0×10^{-9} + 2.92×10^{-11}

3.2.2 Free Drug Co-culture

Ovarian cancer stem cells (CSC) were represented by a high grade serous ovarian cancer cell line, OVCAR3, which had been sorted for ALDH and CD133 expression and were transducted to express green fluorescent protein (GFP+). Mesenchymal stem cells (MSC) were human adipose-derived mesenchymal stem cells. Cells were cultured in 400 cell spheroids composed of, 300 MSC and 100 CSC for the co-culture, in a 3D hanging drop model. 400 cell CSC spheroids were cultured

simultaneously as controls. Spheroids were incubated for 5 days to allow the cells to come together with 2 μL of fresh culture medium added on day 2 or 3. On day 5, spheroids were treated with 10 μM paclitaxel, 5 μM sunitinib or a combination 10 μM paclitaxel + 5 μM sunitinib. On day 7, the spheroids were analyzed to understand the impact of co-culture and co-delivery on CSC stemness, chemoresistance and migration capacity.

3.2.2.1 qPCR Analysis of CSC and MSC communication

In the CSC-MSC co-cultures, MSC have been shown to produce PDGF which then binds to the CSC PDGF receptors starting a signaling cascade that can lead to increased chemoresistance, metastatic potential and increased ALDH expression[3]. In order to ensure that this communication is occurring in the 3D CSC-MSC co-culture, qPCR was conducted on CSC for PDGF receptor B (*PDGFRB*) and Indian Hedgehog (*IHH*) which have been shown previously to be involved[3]. MSC were removed from the analyzed cells by sorting for GFP+ CSC after the cells were harvested from the plates on day 7 using flow cytometry. As expected, there was an increase in the expression of *PDGFRB* and *IHH* in CSC when co-cultured with MSC (Figure 3.7), however this increase was not significant, less than a 2-fold change from CSC alone. Treating with sunitinib reduced the expression of *PDGFRB* and *IHH* in CSC more in the co-culture than in the CSC single culture, but also not significantly.

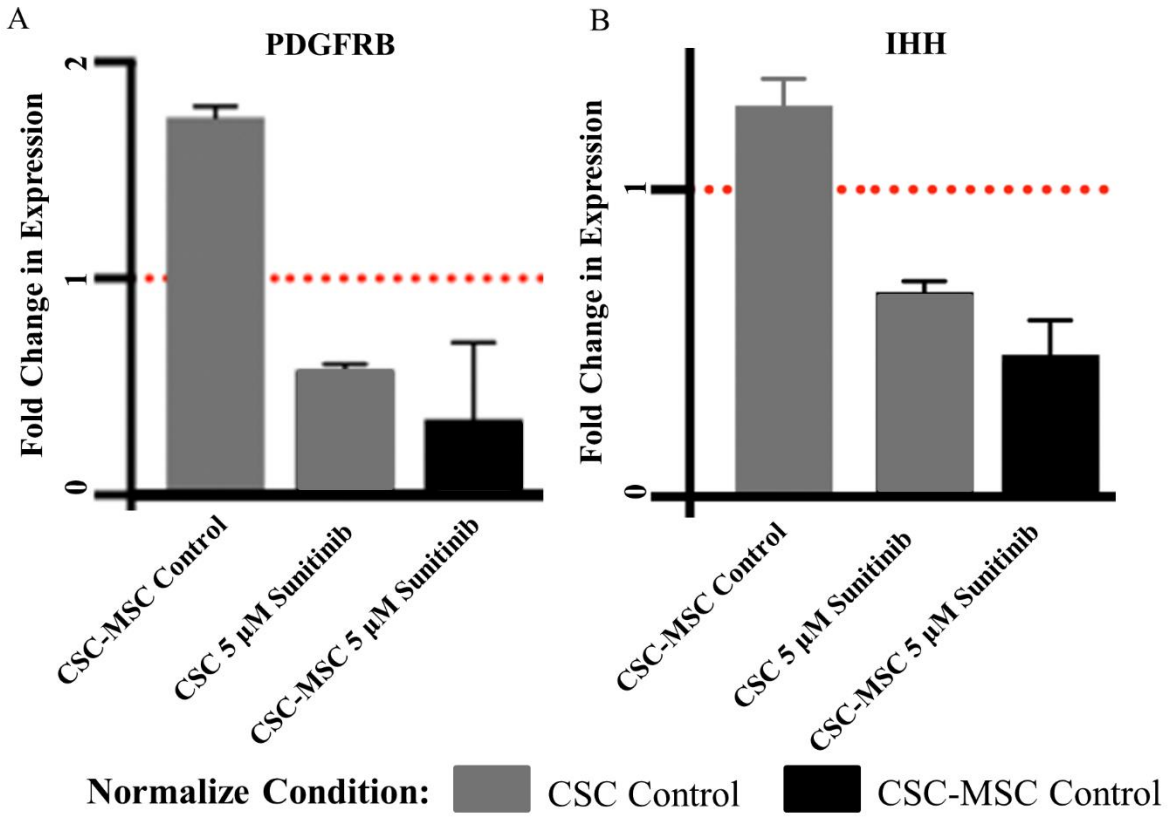

Figure 3.7: Quantification of CSC-MSC signaling with qPCR
qPCR quantified fold change in CSC expression of A) *PDGFRB* and B) *IHH*. The red dotted line indicates the normalized value of the control. Grey bars were normalized to the CSC control condition while the black bars were normalized to the CSC-MSC control condition.

3.2.2.2 Co-culture Live/Dead

Cytotoxicity was evaluated using DAPI exclusion in flow cytometry for CSC single cultures and CSC-MSC co-cultures. MSC do not grow well alone in non-adherent 3D culture, therefore the MSC single culture was tested in a 96 well plate using a plate reader. MSC did not show significant death regardless of treatment, but the sunitinib condition was more alive than the control condition (Figure 3.8A). In the 3D cultures, there were no significant differences in viability, but conditions which were treated with a combination of paclitaxel and sunitinib showed the most death (CSC: 84% ± 8%, CSC-MSC: 88% ± 3%), while paclitaxel alone cased the next amount of death (CSC: 93% ± 5%, CSC-MSC: 91% ± 5%) (Figure 3.8B). Previous studies have shown that MSC co-culture increases chemoresistance to platinum based chemotherapies[3],

however this data indicates that the same trend may not be true with a taxol based treatment. The data does match the observed phase contrast images (Figure 3.9). Visually the CSC-MSC spheroids were smaller than the CSC single cultures. It was expected that the combination treatment would cause more death due to the inhibition of crosstalk between CSC and MSC[3], but as there was no significant up-regulation in *PDGFRB* or *IHH* gene expressions (Figure 3.7), non-significant changes in viability are understandable.

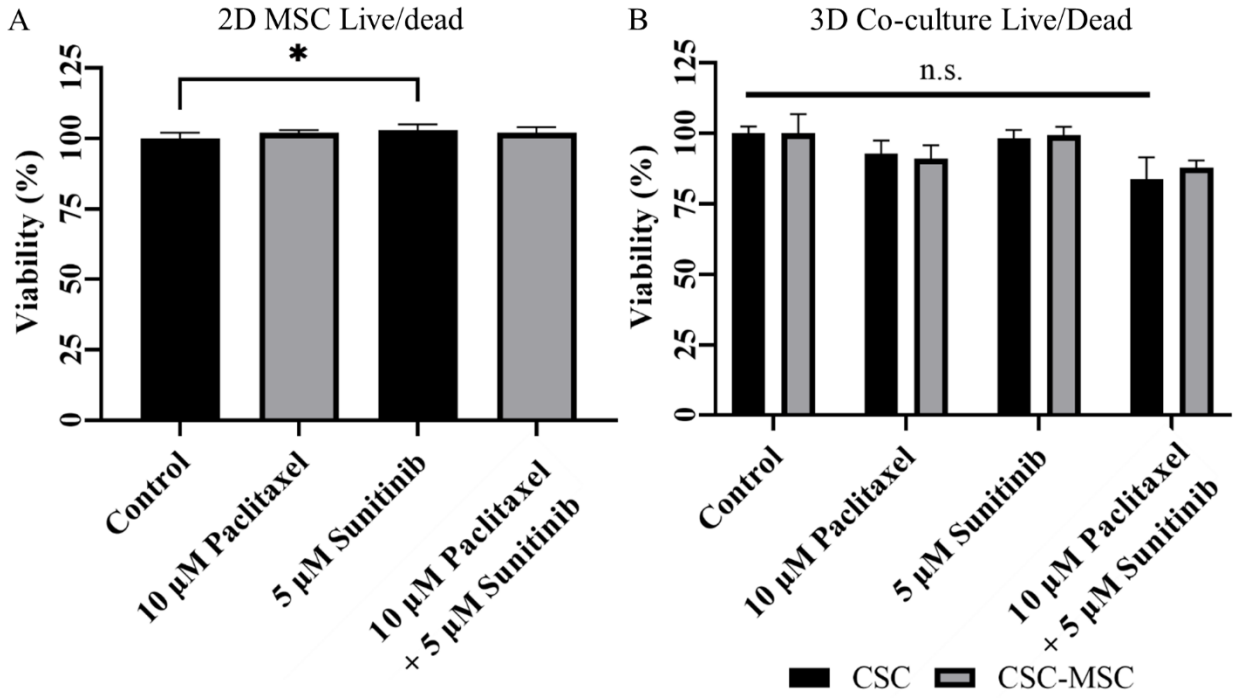

Figure 3.8: Live/Dead plots for MSC, CSC and CSC-MSC
A) Plot of 2D MSC viability quantified from DAPI signal measured on a plate reader. B) Plot of 3D CSC and CSC-MSC viability quantified from DAPI exclusion during flow cytometry.

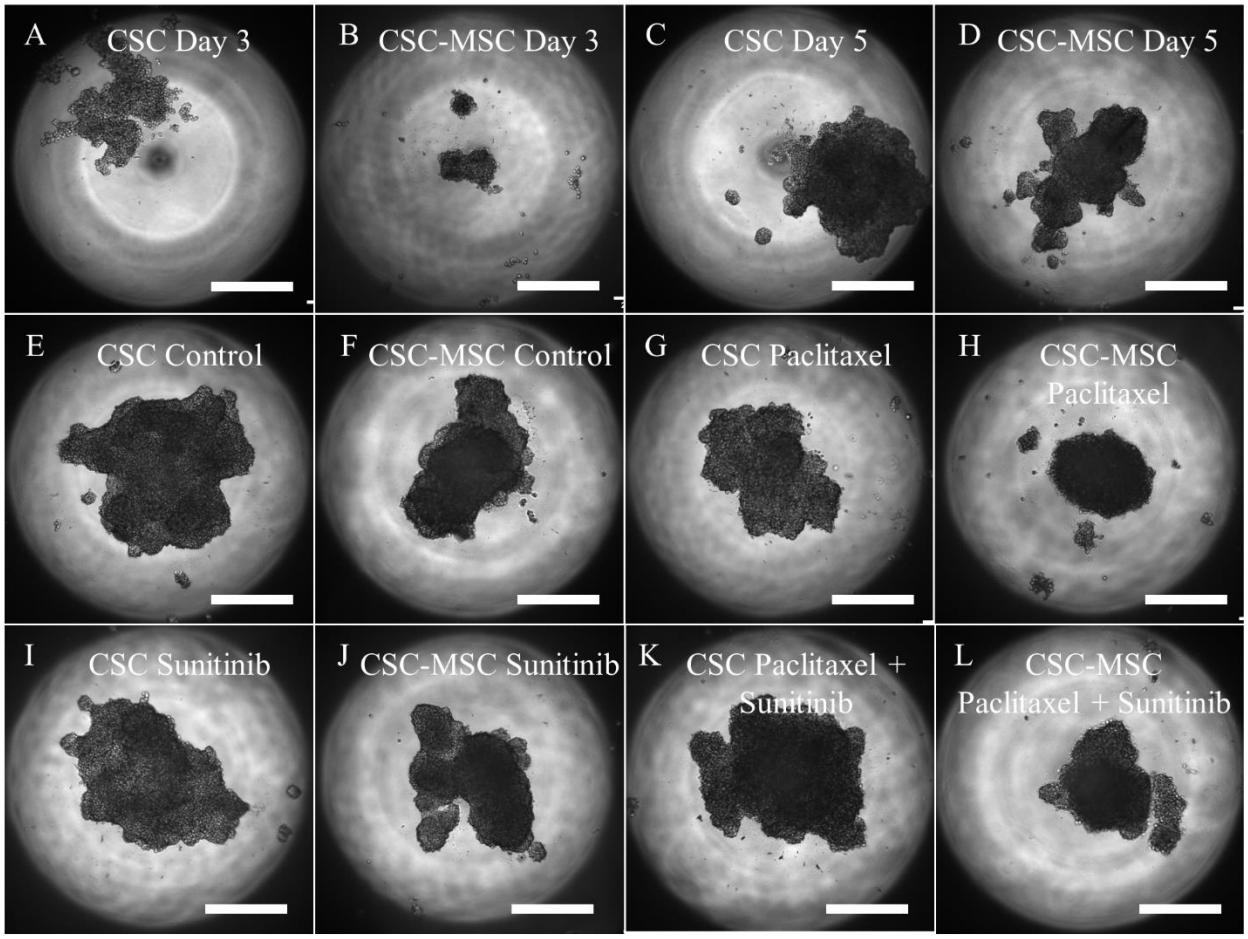

Figure 3.9: Optical microscopy images of 3D CSC and CSC-MSC spheroids
Day 3 images of A) CSC and B) CSC-MSC spheroids. Day 5 images of C) CSC and D) CSC-MSC spheroids. Day 7 images of control E) CSC and F) CSC-MSC spheroids, 10 μM paclitaxel treated G) CSC and H) CSC-MSC spheroids, 5 μM sunitinib treated I) CSC and J) CSC-MSC spheroids and combination 10 μM paclitaxel + 5 μM sunitinib treated K) CSC and L) CSC-MSC spheroids. Scale bar in all images is 400 μm.

3.2.2.3 Changes in Stemness in CSC due to MSC Co-culture

To evaluate CSC ALDH and CD133 expression, both markers of a stem cell phenotype in ovarian cancer cells[89–94], spheroids were harvested on day 7 and then analyzed with flow cytometry and qPCR. For both methods, cells were sorted for GFP+ CSC prior to analysis to remove potential contamination with MSC ALDH or CD133 expression. It was expected that co-culturing CSC with MSC would increase the stem cell-like phenotype in CSC^3, however a non-significant decrease in ALDH activity was observed in flow cytometry (Figure 3.10A) but a small increase of CD133 was

seen with qPCR (Figure 3.10B). In the qPCR plot, the dotted line represents the control condition (CSC or CSC-MSC based on the color) and a significant change would be 2-fold or higher. No change in ALDH activity or CD133 expression was seen with sunitinib treatment in the CSC only condition, but a non-significant decrease in stemness was seen in both flow cytometry and qPCR when the co-culture was treated with sunitinib. While not significant, a reduction in stem cell phenotype markers due to sunitinib treatment indicates that the PDGF signaling pathway between CSC and MSC is being disrupted.

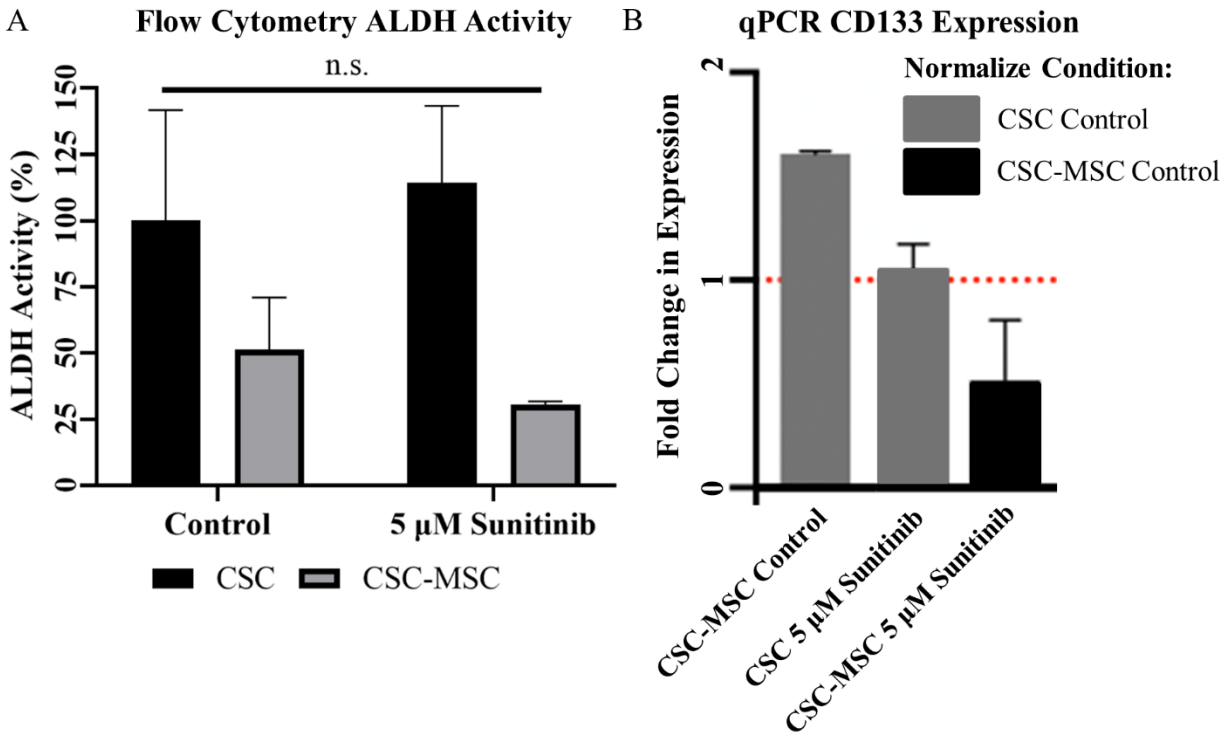

Figure 3.10: Changes in CSC ALDH activity and CD133 expression due to MSC co-culture and sunitinib treatment
A) ALDH activity measured by flow cytometry. B) qPCR quantification of *CD133* gene expression in CSC. The dotted line represents the control condition which is indicated by the color of the bar.

1.2.5 Migration Potential and Epithelial to Mesenchymal Transition of CSC

Migration potential of CSC was evaluated with a scratch assay after 7 days of 3D culture. On day 7, the spheroids were harvested, broken apart, counted and re-plated in a 96 well plate, and

the cells allowed to adhere to the plate. Once the cells were adhered, the monolayer was scratched and imaged at 0 hours and 24 hours to measure the reduced area (reported as a percent) of the scratch which indicates migration potential. MSC cells were not removed from the co-culture and only GFP+ CSC were quantified in the migration images (Figure 3.11A-H). No significant difference was seen between the tested conditions, but there was more migration in the control conditions than the 5 μM sunitinib treated conditions for both CSC and CSC-MSC (Figure 3.11I). This result was expected in the CSC-MSC condition as sunitinib is expected to inhibit PDGF signaling between CSC and MSC, which was previously linked to increased migration and epithelial-to-mesenchymal transition (EMT)[3]. However, it was expected that the CSC-MSC control would have a smaller area percent at 24 hours than the CSC control condition due to MSC mediated increase in migration potential which was not observed. Additionally, EMT potential was quantified by measuring the expression of N-cadherin in CSC using qPCR (Figure 3.11J). Fold change in expression was reported with the dotted line representing the control condition and the control condition denoted by the color of the bar. There was no significant difference in the expression of N-cadherin across the conditions, but there was a small increase in the CSC-MSC control compared to the CSC only control. This increase in N-cadherin is indicative of an increase in EMT in ovarian CSC and was expected to occur to do MSC co-culture[3,104]. Treatment with sunitinib also decreases the expression of N-cadherin in the CSC-MSC condition, aligning with the expected decrease in EMT when PDGF signaling is blocked. These non-significant changes in migration and N-cadherin expression could be due to the low expression of *PDGFRB* seen in CSC indicating that crosstalk between CSC and MSC is not occurring as strongly as previously observed[3].

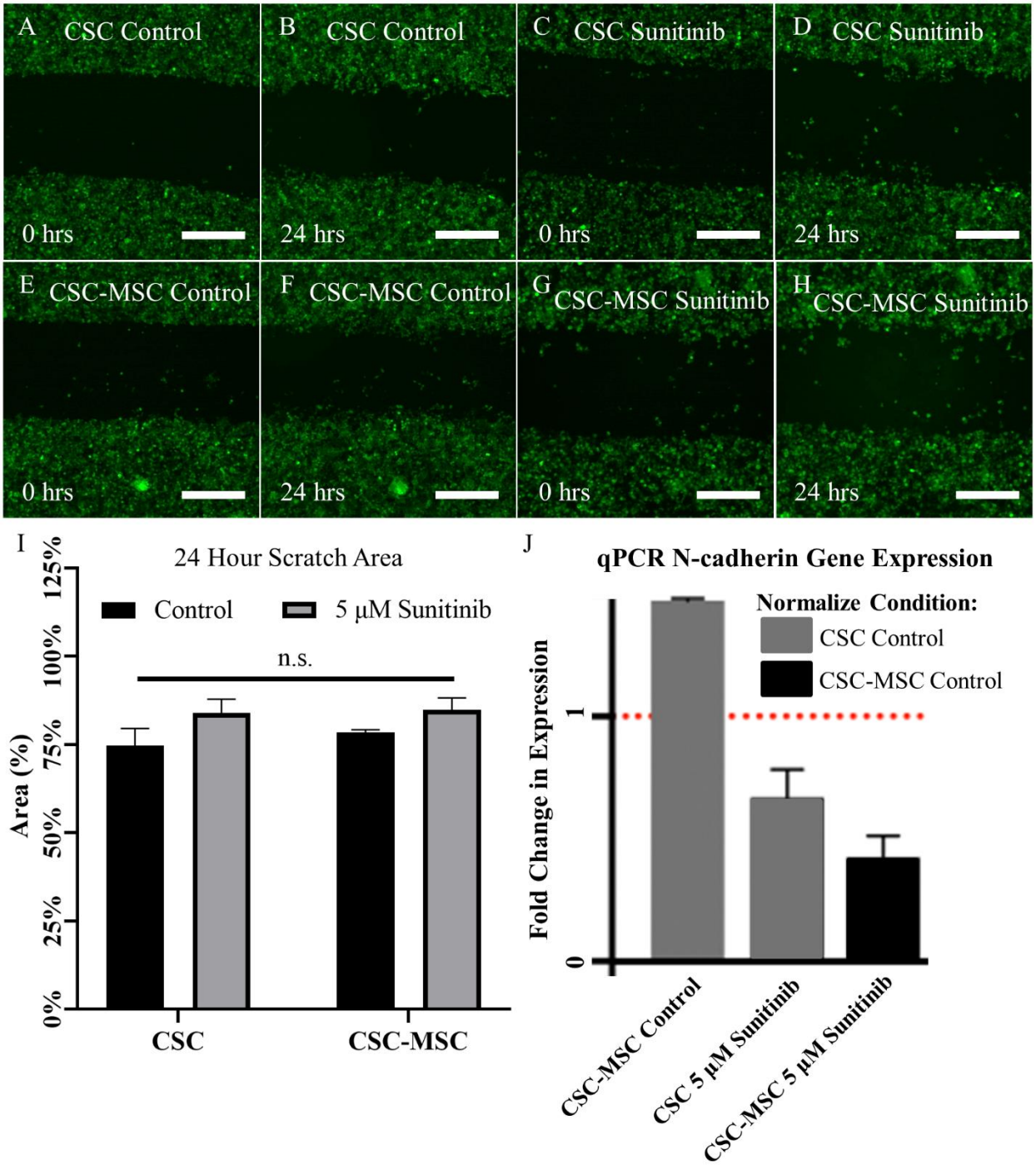

Figure 3.11: Migration and EMT potential of CSC due to MSC co-culture and sunitinib
Scratch analysis images of GFP+ CSC. Control CSC at A) 0 hours and B) 24 hours, 5 μM sunitinib treated CSC at C) 0 hours and D) 24 hours, control CSC-MSC at E) 0 hours and F) 24 hours, and 5 μM sunitinib treated CSC-MSC at G) 0 hours and H) 24 hours. Scale bar is 400 μm in all images. I) Plot quantifying the area percent of the scratch after 24 hours. J) Plot of N-cadherin gene expression in CSC quantified with qPCR. Dotted line represents the control condition with the color of the bar indicating what the control condition was.

3.3 Conclusions

Previous research had identified PDGF signaling between CSC and MSC as a method by which MSC would support CSC and, increase their chemoresistance, ALDH expression and migration potential[3]. Also identified was sunitinib, a tyrosine kinase inhibitor, which had been shown to negate the developed chemoresistance in CSC when delivered with a platinum based chemotherapeutic. In order to create a better delivery system for a chemotherapeutic and sunitinib, a co-delivery nanoparticle was developed using electrospraying. The nanoparticles were between 150 nm and 200 nm and could encapsulate sunitinib, paclitaxel and both drugs together. However, the low nanoparticle yield from electrospraying prevented the testing of the co-delivery formulation at this time. Future work for this part of the project will be focused on increasing the scale of production. This could be accomplished through the construction of ~7 more identical electrospray stations, a multiplex electrospray set up[105], development of a conveyor belt collection method which would increase the automation of the electrospray or a combination of these methods.

Without the nanoparticle formulation, only co-delivery of the free drugs was tested in a 3D hanging drop platform. Single culture CSC were compared to CSC-MSC for *PDGFRB* and *IHH* expression with qPCR and it was found that there was a slight (not significant) increase in expression indicating some communication between CSC and MSC but not the large increase seen previously[3]. This lower amount of communication between CSC and MSC through PDGF is the probable cause for the equally small increases observed in ALDH activity, CD133 expression, migration potential and N-cadherin expression. Future work on this section of the project will be focused on improving the experimental design and understanding the difference between these experiments and those previously conducted in our lab[3].

3.4 Materials and Methods

3.4.1 Cell culture and Materials

Epithelial ovarian cancer cells, OVCAR3 (American Type Culture Collection), were transduced to express green fluorescent protein (GFP+) and were sorted to isolate the subpopulation which expressed CD133 and had high ALDH expression to represent the cancer stem cells (CSC). Human adipose-derived mesenchymal stem cells (MSC) were purchased from Lonza (PT-5006) were used without modification. All cells were used within 10 passages to avoid differentiation. MSC were cultured in 2D prior to plating in 3D in Lonza ADSC basal cell medium (PT-3273) supplemented with 10% fetal bovine serum, 5% Gibco antibiotic-antimycotic (100x), and 2mM of Gibco's 200 mM L-glutamine. CSC were cultured in 2D prior to plating in 3D in Gibco RMPI 1640 cell medium with L-glutamine and phenol red and supplemented with 10% fetal bovine serum and 5% Gibco antibiotic-antimycotic (100x).

To plate in a 384 hanging drop well plate for 3D culture, MSC were removed from 2D culture with Gibco 0.05% Trypsin–EDTA (1x) and the CSC were removed with Gibco 0.25% Trypsin–EDTA (1x). After counting, the cells were resuspended in the proper dilutions in a 50% MSC medium – 50% CSC medium mixture and plated in 20 μL droplets with 400 cells per droplet. The co-culture consisted of 300 MSC and 100 CSC while the single culture consisted of 400 CSC. Spheroids were cultured for 5 days with imaging and feeding (2 μL) on day 2 or 3. On day 5, the spheroids were imaged again, and drug treated. Drug incubation lasted for 2 days, and on day 7 the different conditions were imaged a final time and then the cells were analyzed though various assays.

3.4.2 Flow Cytometry for ALDH Expression and Live/Dead

On day 7, 154 spheroids from each condition were collected, resuspended in FACS buffer, and stained with AldeRed according to the AldeRed ALDH Detection Assay (SCR150, Sigma Aldrich) kit protocol. ALDH expression was analyzed for only GFP+ CSC in order to avoid potential expression from MSC. DAPI exclusion of live cells was used to quantify viability for live/dead analysis by resuspending cells in 1X PBS + 2% FBS + 300 μM 4',6-diamidino-2-phenylindole (DAPI) prior to FACS analysis.

3.4.3 qPCR Assays

308 wells for each condition were collected and resuspended in FACS buffer on day 7 in order to sort for GFP+ CSC using flow cytometry. The cell population with the highest GPF expression was selected as GPF+ CSC. After sorting, the cells were frozen until qPCR was performed. RNA was extracted using the RNeasy extraction kit (74104 Qiagen) and evaluated with a Nanodrop 2000 spectrophotometer (ND-2000 Thermo Fisher Scientific) before following a High-Capacity Reverse Transcriptase cDNA Transcription Kit (4368814 Life Technologies) to transcribe RNA to cDNA. RT-qPCR was performed on a 7900HT system through the University of Michigan Advanced Genomics Core. Data were analyzed using the 2-ΔΔCT method[106].

3.4.4 Migration Assay

After 5 days of 3D culture and 2 days of treatment, 154 spheroids from each condition were collected and broken up, and the cells counted. Cells were then plated in a 96 well plate at 100,000 cells/well in 200 μL of fresh cell medium and allowed to settle overnight. Once settled, a 200 μL pipette tip was used to scrape a horizontal wound in each well. The wound was then imaged using an Olympus optical microscope to identify the migration of the GFP+ CSC into the wound over

24 hours. The area of the wound was measured in ImageJ and the fraction of the original area still clear at 24 hours was calculated as a percent.

3.4.5 Nanoparticle Materials

Acid capped poly (D,L-lactide-co-glycolide) (PLGA) with a ratio of 75:25 (lactide:glycolide) was purchased from Evonik (RG 753H). Tween 20 ultrapure (J20605-AP Thermo Scientific), triethylammonium formate solution (TEAF) (17901 Honeywell), N,N-dimethylformamide (DMF) (D119 Fisher Scientific), acetonitrile (ACN) (A955 Fisher Scientific), paclitaxel (A4393 APExBIO) and sunitinib malate (sunitinib) (HY-10255 Medchem Express) were all used without modification. Additional solvents used were chloroform (C298 Fisher Scientific), dimethyl sulfoxide (DMSO) (D1391 Fisher Scientific), 2,2,2-trifluoroethanol (TFE) (T63002 Sigma Aldrich) and sodium chloride (NaCl) (S271 Fisher Scientific).

1 mL Henke-Ject syringes (1481725 Fisher Scientific) and 30-gauge blunt tip industrial needles (90130100 CML Supply) were used to electrospray the nanoparticle solution. 9” disposable aluminum pie pans (409 Kitchen Dance) were used to collect particles dry and in a water bath. 1.5” plastic razor blades (FM053P2 FOSHIO) were used to scrape nanoparticles off the aluminum pans following a dry collection. 40 μm nylon mesh cell strainers (22363547 Fisher Scientific) were used to filter collected nanoparticle suspensions before centrifuge sorting. 13 mm, 0.2 μm PTFE syringe filters (09720002 Fisher Scientific) were used for preparing samples for liquid chromatography-mass spectrometry.

3.4.6 Electrospray Fabrication of Nanoparticles

The drug free, control nanoparticle formulation consisted of 1.96 vol% PLGA, 72.06 vol% DMF, 25.00 vol% ACN and 0.98 vol% TEAF. The paclitaxel formulation was 0.39 vol% paclitaxel, 1.57 vol% PLGA, 72.06 vol% DMF, 25.00 vol% ACN and 0.98 vol% TEAF. The

sunitinib solution was composed of 0.32 vol% sunitinib, 1.57 vol% PLGA, 72.11 vol% DMF, 25.02 vol% ACN and 0.98 vol% TEAF. The combination paclitaxel + sunitinib solution consisted of 0.32 vol% sunitinib, 0.39 vol% paclitaxel, 1.57 vol% PLGA, 72.06 vol% DMF, 25.00 vol% ACN, 0.98 vol% TEAF. After all components were added together in a glass vial, the solution was vortexed before being loaded into a 1 mL syringe with a 30-guage blunt tipped needle. The syringe was placed in a KD Scientific syringe pump with a flow rate 0.1 mL/hr. The needle was connected to a voltage source and set to 7-10 kV. Below the needle, an aluminum pan was placed for collection with a ground plate just underneath. For a dry collection the set up was left as described, but for a water bath collection, the ground plate and aluminum pan were placed on a stir plate, 100 mL of 0.01% Tween 20 in water was placed in the pan and the bath was stirred constantly during collection.

After all the solution had been expelled from the syringe, the particles were collected. For a dry collection, the pans were left for ~8 hours in the chemical hood to ensure complete evaporation of all solvents. 5 mL of 0.01% Tween 20 in water was pipetted into the pan and a plastic razor blade was used to scrape the particles off the aluminum pan while submerged in the 0.01% Tween 20 puddle. The 0.01% Tween 20 solution would collect the freed particles and the particle suspension was then pipetted out of the pan and into a 50 mL centrifuge tube for centrifuge sorting. Each pan was thoroughly scraped at least twice to ensure all particles were removed. For the water bath collection, after all the solution had been sprayed, the particle suspension was simply poured from the pan into two 50 mL centrifuge tubes for centrifuge sorting.

Once the particles were suspended in 0.01% Tween 20 in 50 mL centrifuge tubes, there no longer was a difference between dry and water bath collection. The particle suspension was probe sonicated, poured through a 40 μm filter to remove large aggregates and then centrifuged for 15

minutes at 10,000 x g to pellet particles larger than 1 μm. The supernatant was then carefully transferred to a fresh centrifuge without disturbing the pellet of larger particles and centrifuged again for 60 minutes at 10,000 x g to pellet all remaining particles in the suspension. After pelleting, the supernatant was removed without disturbing the pellet and then the particles were resuspended in either water or cell medium for further characterization or use. If there was more than 1 tube for a sample then all the samples would be combined, pelleted, and resuspended once more.

3.4.7 Nanoparticle Characterization

3.4.7.1 Scanning Electron Microscopy (SEM)

Nanoparticles imaged with SEM were sprayed directly onto a small silicon chip and then sputter coated with gold for 60 seconds. Imaging was on a Tescan Mira3 FEGSEM with a beam voltage of 3 kV, a beam energy setting of 6 and a working distance of 5 mm.

3.4.7.2 Nanoparticle Tracking Analysis (NTA)

Nanoparticles suspended in water or cell medium were serial diluted between 1 and 4 orders of magnitude and mixed vigorously. The diluted particle suspension was then analyzed with NTA on a Malvern Nanosight NS300 to determine particle size and concentration.

3.4.7.3 Liquid Chromatography-Mass Spectrometry (LCMS)

A known number of particles would be pelleted, the supernatant removed, and the particles dissolved in ACN with vertexing or sonication. The extracted drug in ACN would then be filtered with a 0.2 μm syringe filter and analyzed using an Agilent 6520 Accurate Mass Q-TOF LC/MS with a 250 nm wavelength detector. The injection volume was 2 μL with an aqueous solution of water and 0.1% formic acid, and an organic solution of 95% ACN, 5% water and 0.1% formic acid. The column was an Agilent Zorbax Eclipse Plus C_{18} (959757-902), 2.1 x 50 mm with 1.8 μm

pores. Known standard solutions of paclitaxel or sunitinib in ACN were measured with LCMS first to create a calibration curve which the unknown nanoparticle sample could then be compared.

Chapter 4: Investigating the Essential Oil Component, α-terpineol, in a Nanoparticle Formulation for an Alternative Chemotherapeutic for Ovarian Cancer

4.1 Introduction

The current clinical standard for ovarian cancer therapy consists of surgical de-bulking and platinum-based chemotherapy[107]. However, this treatment has high relapse rates, and a low five year survival rate which is attributed to developed chemoresistance and metastasis of the cancer[20]. With a growing interest in testing the effectiveness of alternative cancer therapies, some essential oils and their individual, active components have been found to be cytotoxic for cancer cells[108]. Of particular interest is the oil from the *Melaleuca alternifolia*, or tea tree which has generally been explored for its antimicrobial properties. Recent research has demonstrated tea tree oil's ability to cause death in breast cancer cells and mouse mesothelioma while also being less potent against non-cancerous cells[109,110]. This specificity towards killing cancer cells over non-cancerous has the potential to make tea tree oil an effective chemotherapeutic. However, there are challenges in developing an essential oil as a chemotherapeutic for internal delivery. One is the natural variability seen in tea tree oil as it is composed of a variety of components and the ratios of these components can change based on the location or year of harvest. Therefore, a single component, isolated from the tea tree oil mixture would be more consistent for analysis and use. Another challenge in the use of tea tree oil as a chemotherapeutic is the hydrophobicity of the oil which requires a form of delivery to increase solubility. To address both challenges, one of the active components of tea tree oil, α-terpineol (αT), was investigated as a chemotherapeutic and a polymer

nanoparticle was used to encapsulate αT to create a more effective delivery method. Additionally, a conjugation reaction was explored in order to tether the hydroxyl group of the αT to the PLGA carboxylic acid end groups in order to create nanoparticle which better encapsulates and stabilizes the volatile, small molecule. Together, this was hypothesized to produce a slow-release nanoparticle which would be more effective than a simple encapsulation nanoparticle or the free αT delivered to ovarian cancer cells.

4.2 Results and Discussion

4.2.1 Comparison of αT IC_{50} Values in Cancerous and Non-cancerous Cells

To test the suitability of αT as a cancer therapy for ovarian cancer, the IC_{50} of αT in cancerous (OVCAR3) and non-cancerous (HFF and IOSE8) cells was investigated. Cells were treated in a 96 well assay and after 24 hours, the number of live and dead cells were counted to give a viability percent. The curve was then analyzed with a non-linear fit in Graphpad Prism to identify the IC_{50} for the 3 cell lines. The OVCAR3 IC_{50} was found to be 466 μM while the non-cancerous IC_{50} values were 1.48 mM and 1.25 mM for IOSE8 and HFF, respectively (Figure 4.1). This indicates that αT is more specific in killing cancer cells as opposed to non-cancerous and cells and has the potential to be used as a chemotherapeutic.

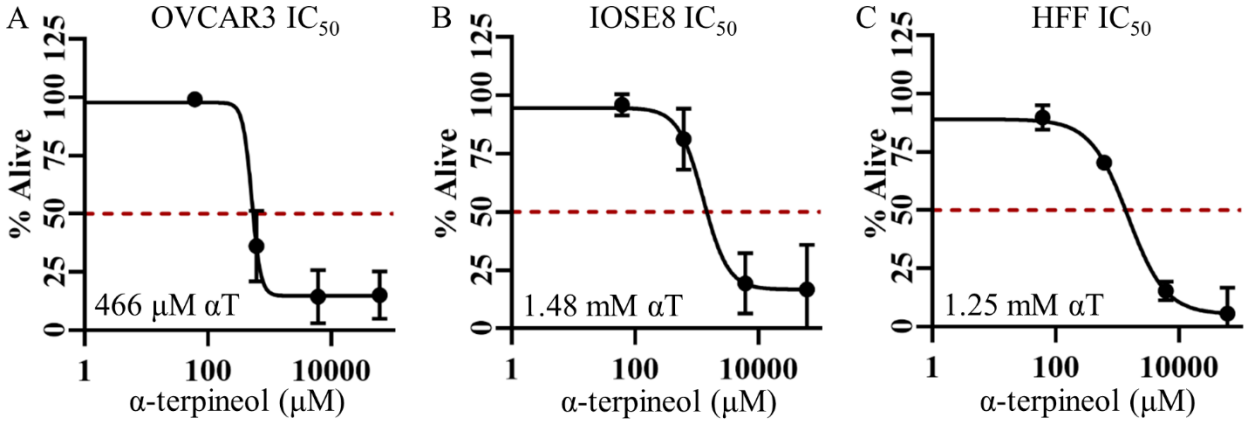

Figure 4.1: IC_{50} plots of αT
IC_{50} plots of A) ovarian cancer cell line OVCAR3, B) non-cancerous ovarian epithelial cell line, IOSE8, and C) non-cancerous fibroblast cell line, HFF.

4.2.2 Investigation of αT-PLGA Conjugation

αT has a very low solubility in aqueous solutions, and thus a delivery method such as a nanoparticle would be needed to deliver αT to internal cancers. However, as αT has a very low molecular weight (~154 g/mol) and is highly volatile, it is presumed that simply encapsulating αT within a polymer nanoparticle will not be very effective as αT will evaporate or diffuse very quickly. Therefore, two methods of tethering the αT to the carboxylic acid end groups of PLGA were investigated with the goal of creating a slow-release formulation of an αT loaded nanoparticle (Figure 4.2).

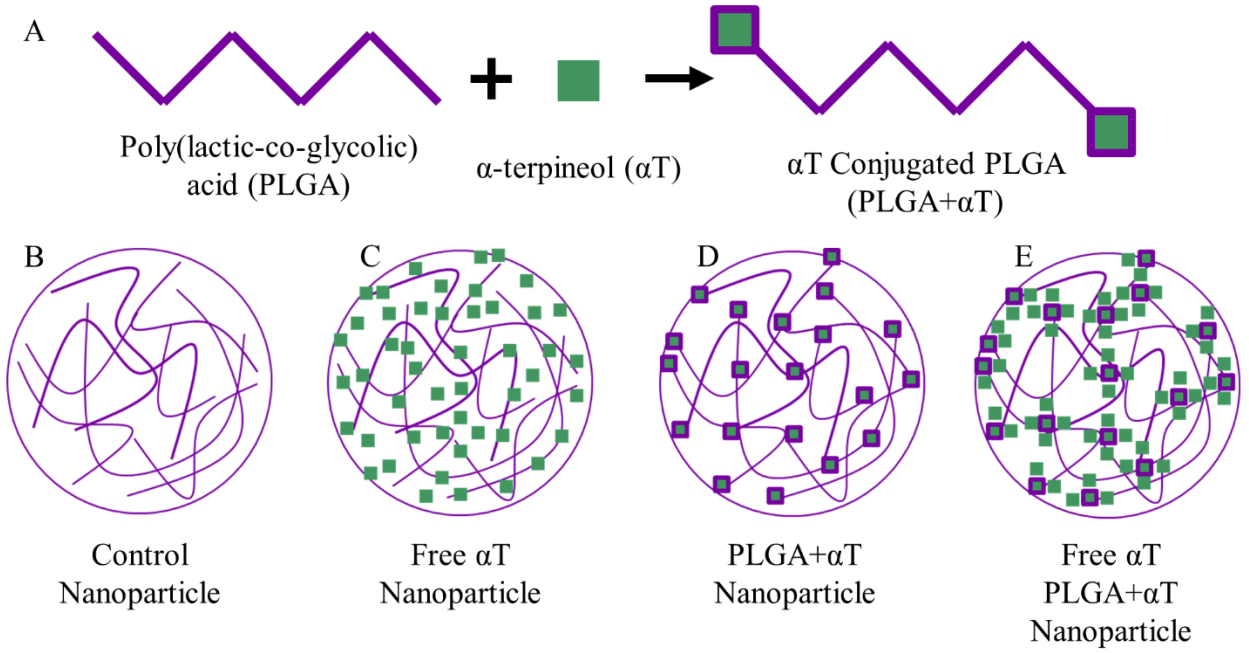

Figure 4.2: Schematic of PLGA nanoparticles designed to encapsulate αT for cancer therapy
A) Schematic of αT tethered to the acid end groups of PLGA. B) Schematic of the control nanoparticle without any αT. C) Schematic of a nanoparticle with free αT encapsulated in a PLGA nanoparticle. D) Nanoparticle fabricated out of the conjugated PLGA+αT polymer shown in (A). E) Nanoparticle fabricated out of conjugated PLGA+αT and encapsulating free αT.

Two methods were investigated to tether the αT to the carboxylic acid end groups of the PLGA chain, one used an isocyanate linker, isophorone diisocyanate (IPDI), between the PLGA and the αT in a two-step reaction (Figure 4.3A, B), and the second directly reacted the αT to the

PLGA through esterification (Figure 4.3C). IPDI is a bifunctional isocyanate and depending on the catalyst, one isocyanate functional group will be more reactive than the other, and by testing different time points, identification of the time needed to bond the more reactive isocyanate can be found (Figure 4.3A). Step two would then be completed as a second reaction and would need to be reacted for longer to ensure that the more unreactive isocyanate arm reacts with αT (Figure 4.3B).

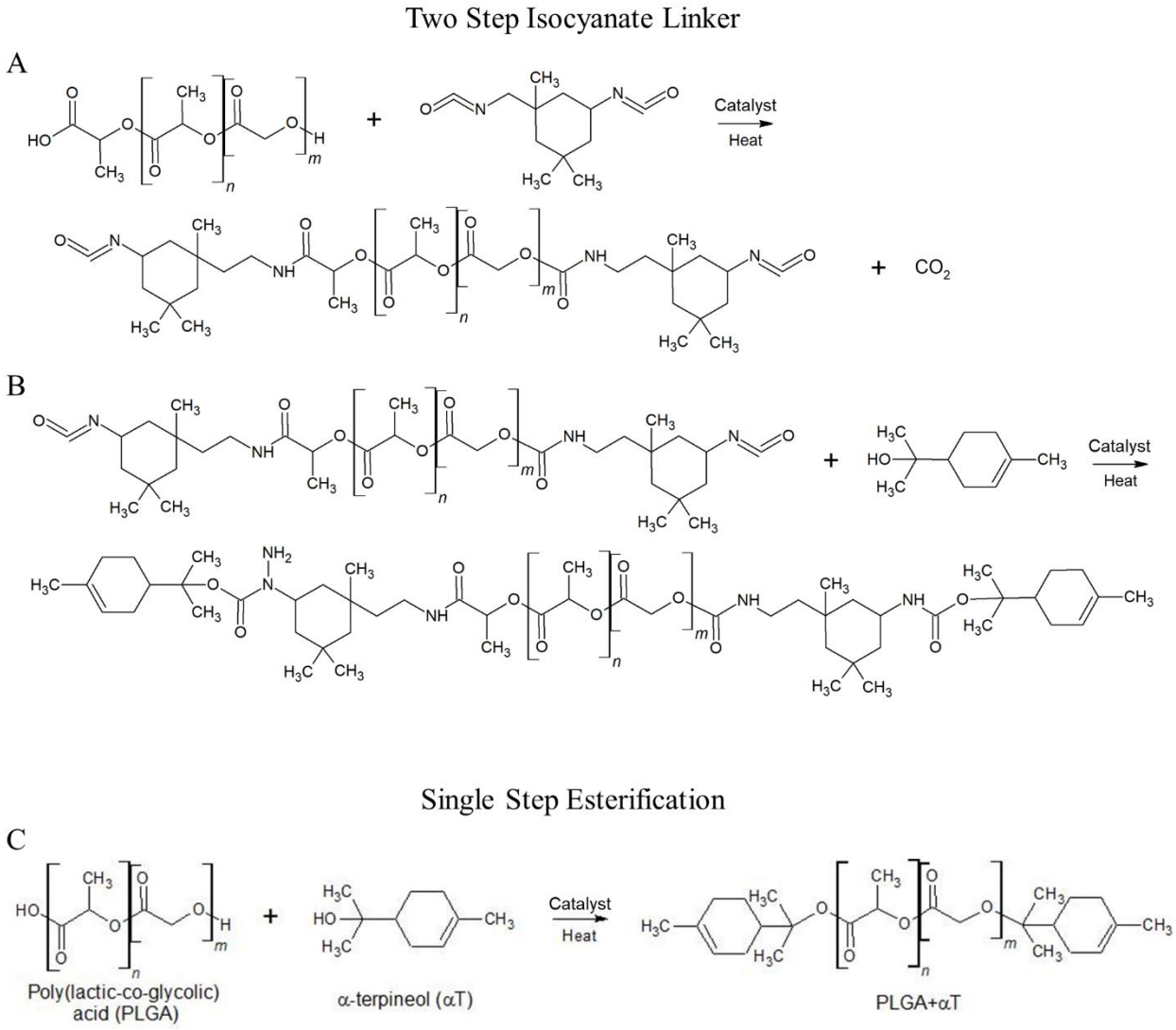

Figure 4.3: Reaction Schemes for tethering αT to PLGA
The two-step isocyanate linker reaction starts with A) reacting IPDI to the carboxylic acid end groups on the PLGA and B) the second step reacts the hydroxyl on the αT to the remaining isocyanate group on the IPDI. C) The singe step esterification reaction between the PLGA carboxylic acid and the αT hydroxyl group.

The first step of the IPDI reaction was carried out under at 35°C with three different catalysts at various time points and analyzed with attenuated total reflection-infrared (ATR-IR) (Figure 4.4) and gel permeation chromatography (GPC) (Table 4.1). ATR-IR allowed for the identification of the IPDI bonding to the PLGA with the appearance of the isocyanate peak at 2260 and the amine peak at 3340 (dotted lines in Figure 4.4). As a negative control, no catalyst was first investigated and evidence of an amine and an isocyanate peak were seen with ATR-IR at 7 days (Figure 4.4A), however, the molecular weight of the polymer after 7 days of reaction (74.1 kDa) is more than double that of unreacted PLGA (33.7 kDa). This indicates that chain to chain reaction of PLGA with the IPDI linker occurs with a high frequency without the use of a catalyst.

Di-n-butyltin dilaurate (DBTL) was the first catalyst investigated as it is the most commonly used catalyst with IPDI reactions, and has shown a high selectivity for the secondary isocyanate carbon[111,112]. The amine and isocyanate peaks appear within 4 hours when DBTL is used (Figure 4.4B), however within 4 hours the molecular weight has also increased by ~5 kDa and continues to slowly increase as the time of reaction also increases. This large increase in molecular weight was unexpected as the molecular weight of IPDI is ~222 Da and an increase of ~444 Da (2 IPDI per PLGA chain) would be within the error of the GPC. Further investigation of DBTL's mechanism of reaction revealed a carboxylic acid substitution (Figure 4.5) which could easily lead to DBTL linking PLGA chains together and causing an increase in the average molecular weight despite its previous use with carboxylic acid reactants[113,114].

Triethylamine (TEA) was investigated as an alternative catalyst to DBTL, and with TEA, the primary isocyanate is more reactive[115]. The TEA reaction is slower than the DBTL reaction as evidenced by the isocyanate peak requiring 24 hours to reach the same intensity as 4 hours with DBTL (Figure 4.4C). The amine peak is much larger than expected for simply the IPDI-PLGA

bond and is due to TEA which was ineffectually removed during the polymer wash steps. The molecular weight of the reacted polymer also increases with TEA as the catalyst (Table 4.1). Another alternative to DBTL which was tested was magnesium chloride hexahydrate ($MgCl_2$) as it had been shown to improve reaction selectively with sterically hindered carboxylic acids[114]. Within the system tested here however, the isocyanate peak did not increase over a reaction time of 24 hours and a broad amine peak formed which suggested the formation of a byproduct instead of the PLGA-IPDI compound (Figure 4.4D). Additionally, the molecular weight increase seen in the $MgCl_2$ catalyzed reactions was the largest of the tested catalysts (Table 4.1).

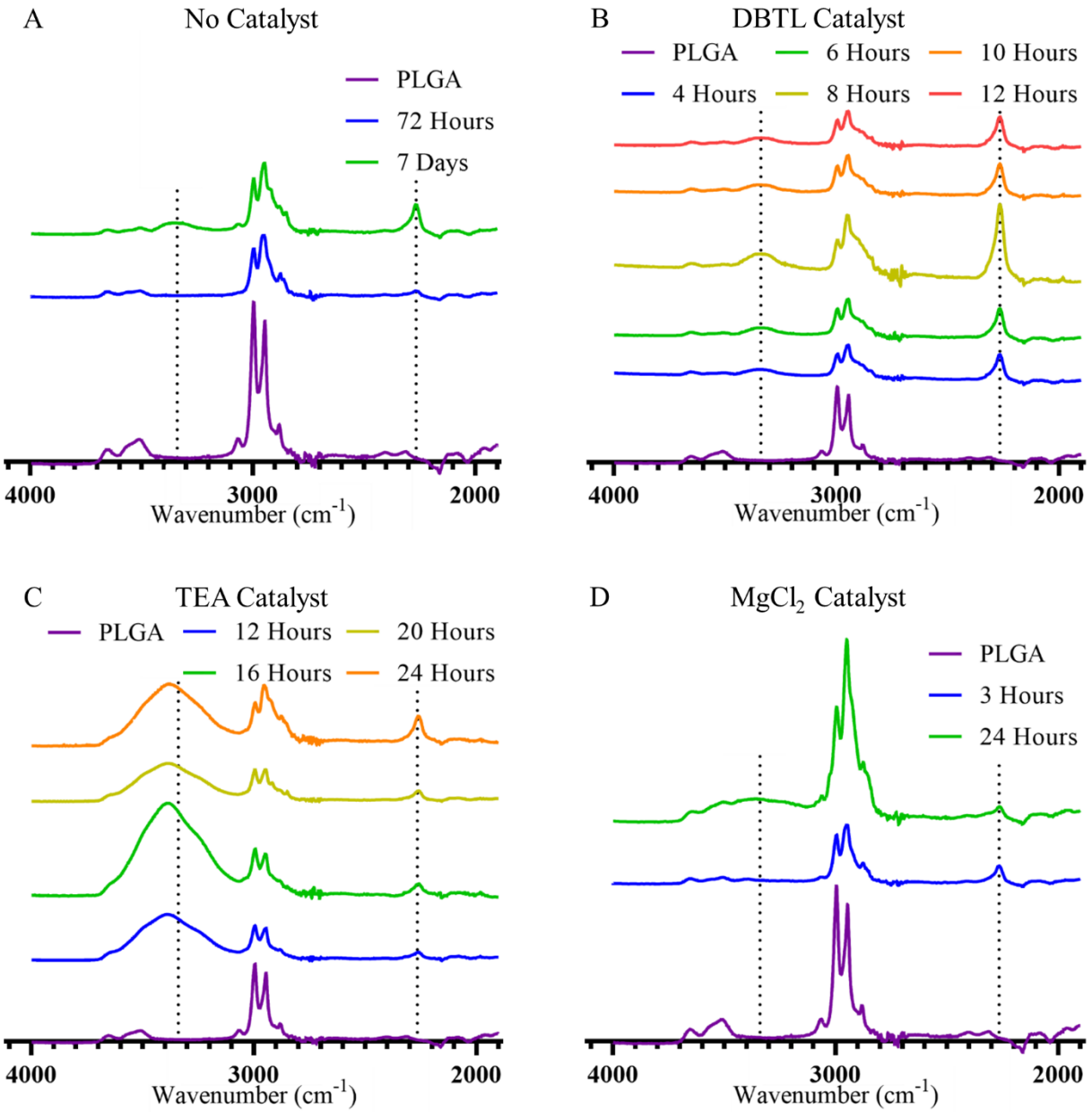

Figure 4.4: ATR-IR spectra of the region of interest for the PLGA+IPDI reaction
Spectra resulting from the reaction of PLGA and IPDI A) without a catalyst for 72 hours and 7 days, B) with DBTL as the catalyst over a range of 4 to 12 hours, C) with TEA as the catalyst over a range of 12 to 24 hours, and D) with $MgCl_2$ as the catalyst at 3 and 24 hours. Dotted lines are at the location of the amine at 3340 and the isocyanate at 2260 which appear when the reaction has occurred.

Table 4.1: PLGA molecular weights measured with GPC

Catalyst	Time (hrs)	MW (kDa)	PDI
–	–	33.7	1.83

None	72	37.2	1.85
None	168	74.1	2.13
DBTL	4	42.2	1.76
DBTL	6	40.8	1.76
DBTL	8	44.0	1.95
DBTL	10	46.1	1.92
DBTL	12	45.2	1.95
TEA	12	42.9	1.95
TEA	16	42.7	2.08
TEA	24	44.1	2.14
$MgCl_2$	3	54.3	1.88
$MgCl_2$	24	76.5	2.21

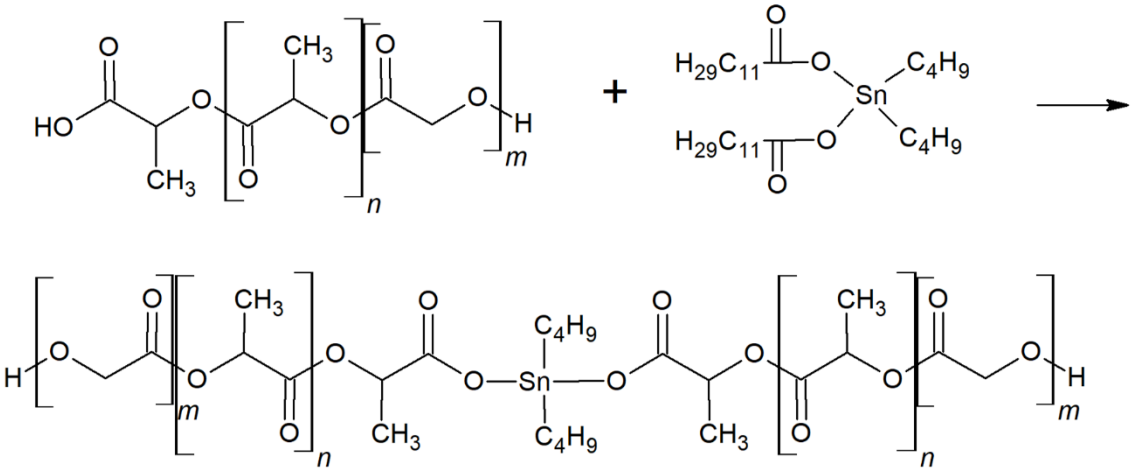

Figure 4.5: Suggested reaction scheme for DBTL reacting to two PLGA chains

With the catalysts tested, a high enough isocyanate selectivity was not achieved to prevent PLGA from linking to itself and so the second method of esterification was investigated (Figure 4.3C). Two different types of catalyst were tested: 1) tosylation, which functionalizes the αT hydroxyl, and 2) metallic catalysts which functionalize the PLGA carboxylic acid[116,117]. Tosylation used p-toluenesulfonyl chloride as the catalyst and pyridine as the solvent, while the metallic catalysts tested included iron (III) nitrate nonahydrate ($Fe(NO_3)_3$), aluminum nitrate nonahydrate

($Al(NO_3)_3$) and zinc nitrate hexahydrate ($Zn(NO_3)_2$). Following the reactions, the polymer was washed and dried and then characterized with ATR-IR (Figure 4.6) and GPC (Table 4.2). Spectra obtained from ATR-IR were analyzed for peak formation at 1675 due to the presence of the αT alkene and the reduction of the 1425 PLGA carboxylic acid peak from esterification. Of the catalysts tested, none showed a reduction in the carboxylic acid peak intensity suggesting that the reaction did not occur despite the alkene peak formation with the $Fe(NO_3)_3$ and $Al(NO_3)_3$ catalysts (Figure 4.6). The alkene peak formation with these two catalysts is thought to be a byproduct of the reaction as there was no corresponding αT hydroxyl peak at 3370 (data not shown). GPC measurements of molecular weight (Table 4.2) show that all reactions cause a reduction in PLGA molecular weight indicating that the reaction conditions favored the breaking of ester bonds as opposed to the formation. The $Al(NO_3)_3$ reaction did not show a reduction in molecular weight after a 3 hour reaction but did after 5 hours. The ATR-IR spectra at 3 hours (Figure 4.6) and 5 hours (not shown) were identical and did not indicate that the reaction had occurred.

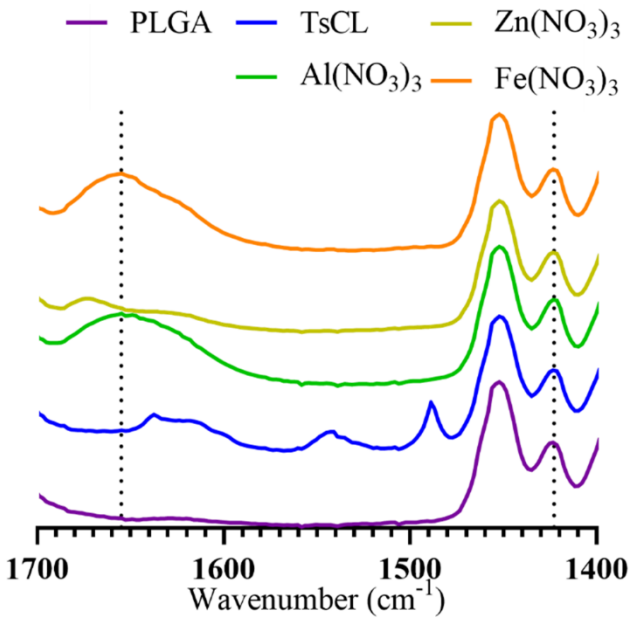

Figure 4.6: ATR-IR spectra of 4 esterification catalyzed reactions of PLGA and αT
Dotted lines at 1675 and 1425 indicate the αT alkene peak and the PLGA carboxylic acid peak, respectively.

Table 4.2: GPC measured molecular weight of PLGA following PLGA+αT esterification reactions

Catalyst	Time (hrs)	MW (kDa)	PDI
–	–	33.7	1.83
TsCl	3	30.5	1.93
$Al(NO_3)_3$	3	33.9	1.99
$Al(NO_3)_3$	5	23.9	1.98
$Zn(NO_3)_2$	3	28.2	2.00
$Fe(NO_3)_3$	3	11.8	1.82

As none of the reaction schemes, IPDI linker or esterification, tested up to this point yielded a complete reaction without effecting the PLGA molecular weight, PLGA nanoparticles were fabricated without using a conjugated PLGA-αT polymer.

4.2.3 Nanoparticle Characterization

PLGA nanoparticles were fabricated in the same method as described in Chapter 3. Briefly, an electrospray method was optimized for solvent composition, spray parameters and the collection method as it was found that the stirring water bath would extend wet droplets into fiber-like particles. Thus, a dry collection method was used for the αT nanoparticles as well. Imaging of the nanoparticles with scanning electron microscopy (SEM) was carried out by placing a small silicon chip under the electrospray for ~3 hours and then imaging (Figure 4.7A, B). After spraying 3 batches of both control and αT loaded nanoparticles, the nanoparticles were collected from the aluminum pans, sorted using centrifugation and then their size and concentration was measured using nanoparticle tracking analysis (NTA) (Figure 4.7C, D). Loading of αT in the nanoparticles was measured by taking a known number of nanoparticles and dissolving them in acetonitrile. The extracted αT was then measured using liquid chromatography-mass spectrometry (LCMS) against a known standard calibration curve (Figure 4.7E). All measurements for the αT and control

nanoparticles are listed in Table 4.3. The control and αT nanoparticles were of similar sizes and through LCMS, it was confirmed that the electrosprayed PLGA nanoparticles could be used to encapsulate αT. However, the fabrication rate and αT loading were very low and the production time required to have enough nanoparticles of a simple *in vitro* viability assay would be about 63 hours of continuous production. Therefore, the effect of delivering αT via nanoparticle was not investigated at this time.

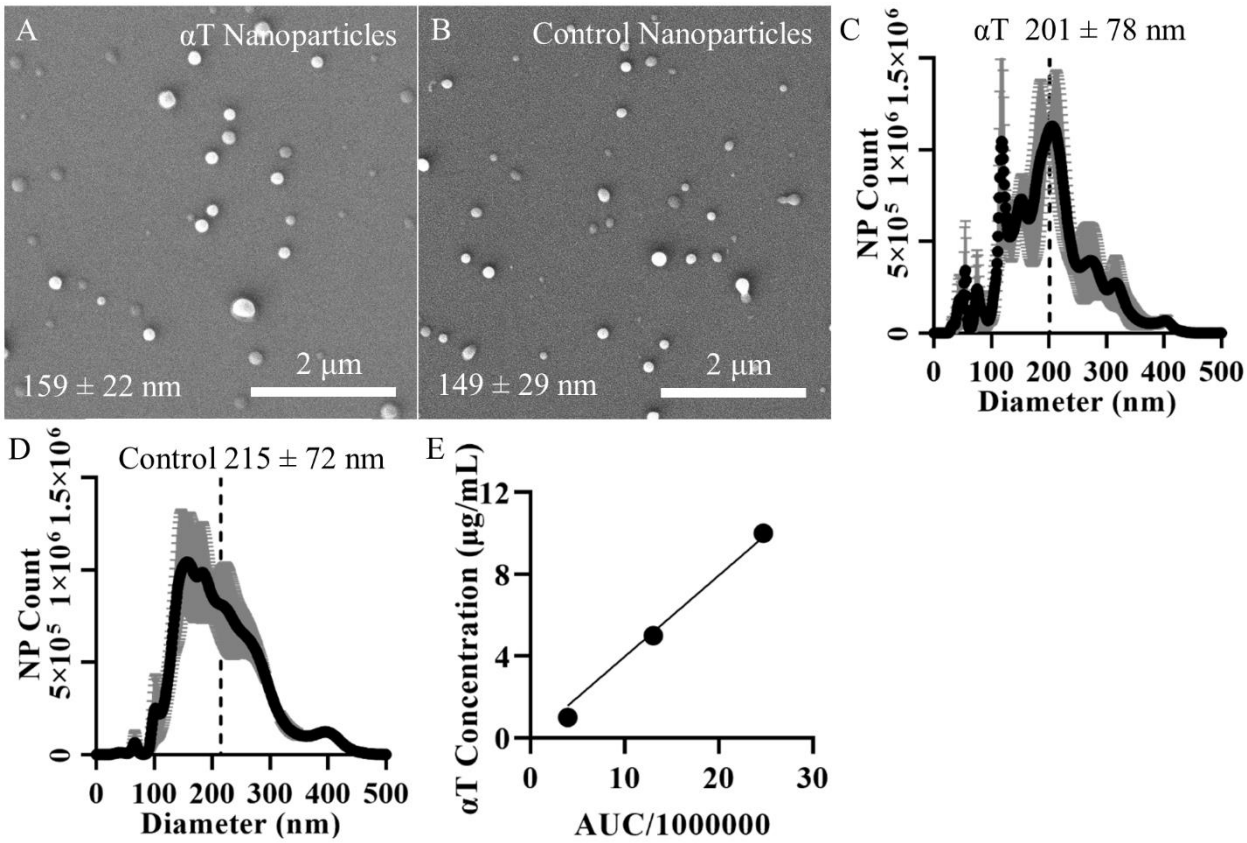

Figure 4.7: Characterization of αT loaded PLGA nanoparticles
A) SEM image of αT nanoparticles. B) NTA size histogram of αT nanoparticles. C) Known standard calibration curve of αT for LCMS measurements of αT loading. D) SEM image of control nanoparticles. E) NTA size histogram of control nanoparticles.

Table 4.3: Tabulation of αT loaded nanoparticle parameters

Nanoparticle	SEM Diameter (nm)	NTA Diameter (nm)	NTA Nanoparticle Count	αT Loading (µL/NP)
αT	159 ± 22	201 ± 78	1.65×10^{9}	2.54×10^{-10}
Control	149 ± 29	215 ± 72	1.6×10^{10}	–

4.2.4 *In vitro* OVCAR3 αT Viability

Without a method to tether αT to the PLGA carboxylic acid end groups, and with the extensive amount of time required to fabricate enough αT loaded nanoparticles, only free αT was delivered to OVCAR3 cells in a 3D viability *in vitro* assay. OVCAR3 were plated in 20 μL droplets on a 384-hanging drop plate with 100 cells/droplet. The spheroids were cultured for 5 days (Figure 4.8A) and then treated with 500 μM αT or served as the control (Figure 4.8B, C). After 2 days of treatment, cell viability was measured with an MTS assay (Figure 4.8D). Significant death was seen in the 500 μM αT treated condition and the treated spheroids were smaller than the control spheroids. This suggests that αT could be used as a chemotherapeutic for ovarian cancer.

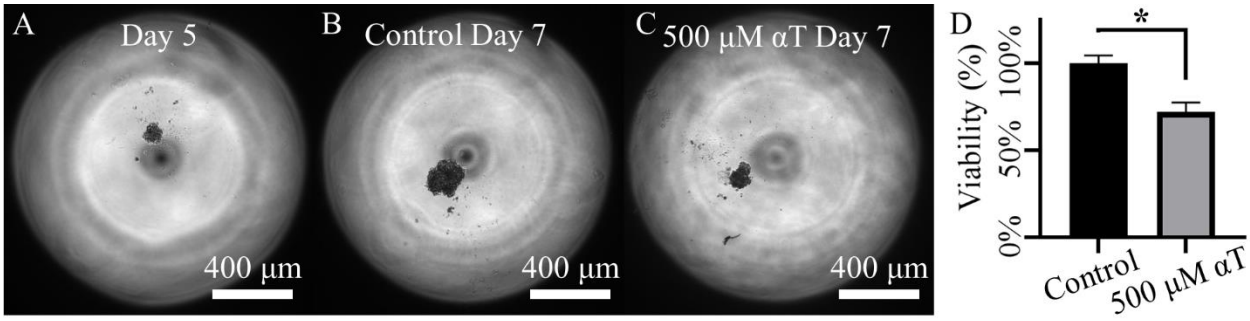

Figure 4.8: *in vitro* evaluation of OVCAR3 treated with free αT in a 3D hanging drop model Optical microscopy images of A) OVCAR3 spheroid on day 5, B) control spheroid imaged on day 7, C) spheroid treated with 500 μM αT imaged on day 7. D) Viability results of control spheroids compared to those treated with 500 μM αT (N = 3, *$p<0.05$).

4.3 Conclusions

One of the active components of tea tree oil, α-terpineol (αT), has been shown to be a potential cancer therapy for ovarian cancer. When comparing the IC_{50} value between cancerous and non-cancerous cells, ovarian cancer cells had an IC_{50} of about half that of non-cancerous cells indicating an inherent specificity in αT. Additionally, in a physiologically relevant 3D *in vitro* assay, significant death was seen when OVCAR3 were treated with 500 μM αT. It was hypothesized that encapsulating the hydrophobic αT in a PLGA based nanoparticle would increase

the solubility and deliverability of αT for internal cancers. Electrosprayed PLGA nanoparticles were fabricated encapsulating αT, and the αT loaded nanoparticles were comparable in size and morphology to control nanoparticles. However, electrospray fabrication has a low production rate, and this led to a time restriction in producing enough nanoparticles to conduct a 3D *in vitro* assay comparing αT nanoparticles and free αT, and so this has not been investigated yet. Lastly, it was hypothesized that conjugation of the αT to the carboxylic acid end groups of PLGA would create a stabilizing effect on the encapsulated αT, thus creating a slow-release formulation with a higher initial loading. Two reaction methods were explored, an isocyanate linker and esterification, however, neither method resulted in a completed reaction that did not also alter the molecular weight of the PLGA. Therefore, the effect of αT stabilization within the PLGA nanoparticle was not explored at this time. Future work focused on the scale-up of electrospray nanoparticle fabrication similar to Chapter 3 could be used to produce enough αT loaded nanoparticles for *in vitro* studies. Additionally, alternate essential oils could be tested for cancer cell cytotoxicity and in synthesizing a PLGA-essential oil conjugated polymer for a slow-release nanoparticle.

4.4 Materials and Methods

4.4.1 Cell Culture and Materials

Epithelial ovarian cancer cells, OVCAR3 (American Type Culture Collection), as well as non-cancerous cells, HHF (fibroblasts) and IOSE8 (ovarian epithelial) were maintained in 2D growth culture in Gibco RMPI 1640 cell medium with L-glutamine and phenol red, supplemented with 10% fetal bovine serum and 5% Gibco antibiotic-antimycolic (100x). The MTS assay was purchased from Abcam and the manufacturer protocols followed.

2D culture analysis was in a 96 well plate with 500 cells/well with a maximum volume of 200 μL. Cells were removed from 2D growth culture with Gibco 0.25% Trypsin–EDTA (1x),

counted and seeded. Cells were allowed to settle overnight and then treated the following day. After 24 hours of treatment, both live and dead cells were collected from the wells and counted with trypan blue on a hemocytometer to obtain a viability percent.

To plate in a 384 hanging drop well plate for 3D culture, OVCAR3 were removed from 2D growth culture with Gibco 0.25% Trypsin–EDTA (1x). After counting, the cells were resuspended in the proper dilutions and plated in 20 µL droplets with 100 cells per droplet. Spheroids were cultured for 5 days with imaging and feeding on day 3. On day 5, the spheroids were imaged again, and drug treated. Drug incubation lasted for 2 days, and on day 7 the different conditions were imaged a final time and then the cell viability was measured with an MTS assay.

4.4.2 2D IC_{50} Quantification

Determination of the IC_{50} value of αT for OVCAR3 and 2 non-cancerous cell lines was conducted in 2D. Cells were plated at 500 cells/well and the cells allowed to settle overnight. The next day, αT was delivered over a range of 60 µM to 60 mM and after 24 hours the number of live and dead cells was counted using trypan blue on a hemocytometer. Identification of the IC_{50} was done using a non-liner fit in Graphpad Prism 9.0.0.

4.4.3 3D Cell Viability Assay

On day 7 of the 3D viability assay, 2 µL of the MTS reagent was added to each well and the plate incubated for 4 hours and then read on a BioTek Synergy HT microplate reader. Analysis of the data was then carried out in Graphpad Prism 9.0.0.

4.4.4 Nanoparticle Materials

Acid capped poly (D,L-lactide-co-glycolide) (PLGA) with a ratio of 75:25 (lactide:glycolide) was purchased from Evonik (RG 753H). Tween 20 ultrapure (J20605-AP Thermo Scientific), triethylammonium formate solution (TEAF) (17901 Honeywell), N,N-

dimethylformamide (DMF) (D119 Fisher Scientific), acetonitrile (ACN) (A955 Fisher Scientific), and α-terpineol (αT) (W304522 Sigma-Aldrich) were all used without modification.

1 mL Henke-Ject syringes (1481725 Fisher Scientific) and 30-gauge blunt tip industrial needles (90130100 CML Supply) were used to electrospray the nanoparticle solution. 9" disposable aluminum pie pans (409 Kitchen Dance) were used to collect particles. 1.5" plastic razor blades (FM053P2 FOSHIO) were used to scrape nanoparticles off the aluminum pans. 40 μm nylon mesh cell strainers (22363547 Fisher Scientific) were used to filter collected nanoparticle suspensions before centrifuge sorting. 13 mm, 0.2 μm PTFE syringe filters (09720002 Fisher Scientific) were used for preparing samples for liquid chromatography-mass spectrometry.

4.4.5 Electrospray Fabrication of Nanoparticles

The drug free, control nanoparticle formulation consisted of 1.96 vol% PLGA, 72.06 vol% DMF, 25.00 vol% ACN and 0.98 vol% TEAF. The αT formulation was 3.79 vol% αT, 1.52 vol% PLGA, 69.60 vol% DMF, 24.15 vol% ACN and 0.95 vol% TEAF. After all components were added together in a glass vial, the solution was vortexed before being loaded into a 1 mL syringe with a 30-guage blunt tipped needle. The syringe was placed in a KD Scientific syringe pump with a flow rate 0.1 mL/hr. The needle was connected to a voltage source and set to 7-10 kV. Below the needle, an aluminum pan was placed for collection with a ground plate just underneath.

After all the solution had been expelled from the syringe, the particles were left for ~8 hours in the chemical hood to ensure complete evaporation of all solvents. The particles were then collected by pipetting 5 mL of 0.01% Tween 20 in water into the pan and a plastic razor blade was used to scrape the particles off the aluminum pan while submerged in the 0.01% Tween 20 puddle. The 0.01% Tween 20 solution would collect the freed particles and the particle suspension could

then be pipetted out of the pan and into a 50 mL centrifuge tube for centrifuge sorting. Each pan would be thoroughly scraped at least twice to ensure all particles were removed.

Once the particles were suspended in 0.01% Tween 20, the particle suspension would be probe sonicated, poured through a 40 μm filter to remove large aggregates and then centrifuged for 15 minutes at 10,000 x g to pellet particles larger than 1 μm. The supernatant was then carefully transferred to a fresh centrifuge without disturbing the pellet of larger particles and centrifuged again for 60 minutes at 10,000 x g to pellet all remaining particles in the suspension. After pelleting, the supernatant was removed without disturbing the pellet and then the particles were resuspended in either water or cell medium for further characterization or use. If there was more than 1 tube for a sample then all the samples were combined, pelleted, and resuspended once more.

4.4.6 Nanoparticle Characterization

4.4.6.1 Scanning Electron Microscopy (SEM)

Nanoparticles imaged with SEM were sprayed directly onto a small silicon chip and then sputter coated with gold for 60 seconds. Imaging was on a Tescan Mira3 FEGSEM with a beam voltage of 3 kV, a beam energy setting of 6 and a working distance of 5 mm.

4.4.6.2 Nanoparticle Tracking Analysis (NTA)

Nanoparticles suspended in water or cell medium were serial diluted between 1 and 4 orders of magnitude and mixed vigorously. The diluted particle suspension was then analyzed with NTA on a Malvern Nanosight NS300 to determine particle size and concentration.

4.4.6.3 Liquid Chromatography-Mass Spectrometry (LCMS)

A known number of particles would be pelleted, the supernatant removed, and the particles dissolved in ACN with vertexing or sonication. The extracted drug in ACN would then be filtered with a 0.2 μm syringe filter and analyzed using an Agilent 6520 Accurate Mass Q-TOF LC/MS

with a 250 nm wavelength detector. The injection volume was 2 μL with an aqueous solution of water and 0.1% formic acid, and an organic solution of 95% ACN, 5% water and 0.1% formic acid. The column was an Agilent Zorbax Eclipse Plus C_{18} (959757-902), 2.1 x 50 mm with 1.8 μm pores. Known standard solutions of αT in ACN were measured with LCMS first to create a calibration curve which the unknown nanoparticle sample could then be compared to.

4.4.7 αT+PLGA Conjugation Materials

Acid capped poly (D,L-lactide-co-glycolide) (PLGA) with a ratio of 75:25 (lactide:glycolide) was purchased from Evonik (RG 753H). N,N-dimethylformamide (DMF) (D119 Fisher Scientific), acetonitrile (ACN) (A955 Fisher Scientific), dichloromethane (DCM) (D37 Fisher Scientific), hexane (H302 Fisher Scientific), pyridine (P368 Fisher Scientific), isophorone diisocyanate (IPDI) (317624 Aldrich Chemistry), tetrahydrofuran (THF) (T397 Fisher Scientific), triethylamine (TEA) (157911000 ARCOS Organics), di-n-butyltin dilaurate (DBTL) (71130 Alfa Aesar), p-toluenesulfonyl chloride (TsCl) (T0272 TCI), iron (III) nitrate nonahydrate ($Fe(NO_3)_3$) (216828 Sigma-Aldrich), aluminum nitrate nonahydrate ($Al(NO_3)_3$) (AC218281000 ARCOS Organics), Zinc nitrate hexahydrate ($Zn(NO_3)_2$) (228737 Sigma-Aldrich), aluminum chloride hexahydrate ($AlCl_3$) (237078 Sigma-Aldrich), calcium chloride dihydrate ($CaCl_2$) (BP510 Fisher Scientific), magnesium chloride hexahydrate ($MgCl_2$) (M33 Fisher Scientific) and α-terpineol (αT) (W304522 Sigma-Aldrich) were all used without modification

4.4.8 αT+PLGA Reaction Schemes

4.4.8.1 Isocyanate Linker Schemes

No Catalyst – 88.2 wt% PLGA was dissolved in 11.7 wt% DCM and 0.1 wt% IPDI was added to a 100 mL round bottom flask with a stir bar. The reaction was heated in a heat jacket with a variable outlet to 35°C and reacted for the desired amount of time. When done, the reaction was

halted by crashing the solution in hexane at a concentration of 12.5 vol% or less in a 50 mL centrifuge tube. The crashed solution was then centrifuged for 2 minutes at 10,000 x g to pellet the polymer. The supernatant was removed, and the polymer was dried under vacuum. Once dry, the polymer was dissolved in DCM at about 2% w/v, and if there were multiple tubes of the same polymer, they were combined at this step. The polymer solution was then washed again by crashing at ~12.5 vol% in hexane, centrifuged for 2 minutes at 10,000 x g, the supernatant removed, and the polymer dried under vacuum.

DBTL Catalyst – 88.1 wt% PLGA was dissolved in 11.7 wt% DCM and 0.1 wt% IPDI and DBTL were added to a 100 mL round bottom flask with a stir bar. The reaction was heated in a heat jacket with a variable outlet to 35°C and reacted for the desired amount of time. When done, the reaction was halted by crashing the solution in hexane at a concentration of 12.5 vol% or less in a 50 mL centrifuge tube. The crashed solution was then centrifuged for 2 minutes at 10,000 x g to pellet the polymer. The supernatant was removed, and the polymer was dried under vacuum. Once dry, the polymer was dissolved in DCM at about 2% w/v, and if there were multiple tubes of the same polymer, they were combined at this step. The polymer solution was then washed again by crashing at ~12.5 vol% in hexane, centrifuged for 2 minutes at 10,000 x g, the supernatant removed, and the polymer dried under vacuum.

TEA Catalyst – 88.1 wt% PLGA was dissolved in 11.7 wt% DCM and 0.1 wt% IPDI and TEA were added to a 100 mL round bottom flask with a stir bar. The reaction was heated in a heat jacket with a variable outlet to 35°C and reacted for the desired amount of time. When done, the reaction was halted by crashing the solution in hexane at a concentration of 12.5 vol% or less in a 50 mL centrifuge tube. The crashed solution was then centrifuged for 2 minutes at 10,000 x g to pellet the polymer. The supernatant was removed, and the polymer was dried under vacuum. Once

dry, the polymer was dissolved in DCM at about 2% w/v, and if there were multiple tubes of the same polymer, they were combined at this step. The polymer solution was then washed again by crashing at ~12.5 vol% in hexane, centrifuged for 2 minutes at 10,000 x g, the supernatant removed, and the polymer dried under vacuum.

$MgCl_2$ – 75.0 wt% PLGA was dissolved in 10.0 wt% DCM and 0.1 wt% IPDI and 15.0 wt% $MgCl_2$ were added to a 100 mL round bottom flask with a stir bar. The reaction was heated in a heat jacket with a variable outlet to 35°C and reacted for the desired amount of time. When done, the reaction was halted by crashing the solution in hexane at a concentration of 12.5 vol% or less in a 50 mL centrifuge tube. The crashed solution was then centrifuged for 2 minutes at 10,000 x g to pellet the polymer. The supernatant was removed, and the polymer was dried under vacuum. Once dry, the polymer was dissolved in DCM at about 2% w/v, and if there were multiple tubes of the same polymer, they were combined at this step. The polymer solution was then washed again by crashing at ~12.5 vol% in hexane, centrifuged for 2 minutes at 10,000 x g, the supernatant removed, and the polymer dried under vacuum.

Esterification Schemes

TsCl – 62.4 wt% PLGA and 31.2 wt% TsCl were dissolved in 5.5 wt% pyridine and 1.0 wt% αT in a glass vial with a stir bar. The reaction was heated in a sand bath to 65°C and stirred for 3 hours. After 3 hours, the reaction was halted by crashing the solution in hexane at a concentration of 12.5 vol% or less in a 50 mL centrifuge tube. The crashed solution was then centrifuged for 2 minutes at 10,000 x g to pellet the polymer. The supernatant was removed, and the polymer was dried under vacuum. Once dry, the polymer was dissolved in DCM at about 2% w/v, and if there were multiple tubes of the same polymer, they were combined at this step. The

polymer solution was then washed again by crashing at ~12.5 vol% in hexane, centrifuged for 2 minutes at 10,000 x g, the supernatant removed, and the polymer dried under vacuum.

$Al(NO_3)_3$ – 44.7 wt% PLGA and 50.8 wt% $Al(NO_3)_3$ were dissolved in 3.8 wt% DMF with 0.7 wt% αT in a glass vial with a stir bar. After 3 hours, the reaction was halted by crashing the solution in cold water at a concentration of 12.5 vol% or less in a 50 mL centrifuge tube. The crashed solution was then centrifuged for 30 minutes at 10,000 x g to pellet the polymer. The supernatant was removed, and the polymer was dissolved in DCM at about 2% w/v, and if there were multiple tubes of the same polymer, they were combined at this step. The polymer solution was then washed again by crashing at ~12.5 vol% in hexane, centrifuged for 2 minutes at 10,000 x g, the supernatant removed, and the polymer dried under vacuum.

$Zn(NO_3)_2$ – 50.0 wt% PLGA and 45.0 wt% $Zn(NO_3)_2$ were dissolved in 4.2 wt% DMF with 0.8 wt% αT in a glass vial with a stir bar. After 3 hours, the reaction was halted by crashing the solution in cold water at a concentration of 12.5 vol% or less in a 50 mL centrifuge tube. The crashed solution was then centrifuged for 30 minutes at 10,000 x g to pellet the polymer. The supernatant was removed, and the polymer was dissolved in DCM at about 2% w/v, and if there were multiple tubes of the same polymer, they were combined at this step. The polymer solution was then washed again by crashing at ~12.5 vol% in hexane, centrifuged for 2 minutes at 10,000 x g, the supernatant removed, and the polymer dried under vacuum.

$Fe(NO_3)_3$ – 43.0 wt% PLGA and 52.7 wt% $Fe(NO_3)_3$ were dissolved in 3.7 wt% DMF with 0.7 wt% αT in a glass vial with a stir bar. After 3 hours, the reaction was halted by crashing the solution in cold water at a concentration of 12.5 vol% or less in a 50 mL centrifuge tube. The crashed solution was then centrifuged for 30 minutes at 10,000 x g to pellet the polymer. The supernatant was removed, and the polymer was dissolved in DCM at about 2% w/v, and if there

were multiple tubes of the same polymer, they were combined at this step. The polymer solution was then washed again by crashing at ~12.5 vol% in hexane, centrifuged for 2 minutes at 10,000 x g, the supernatant removed, and the polymer dried under vacuum.

4.4.9 αT+PLGA Conjugation Characterization

4.4.9.1 Attenuated Total Reflection-Infrared (ATR-IR) Spectroscopy

Once the polymer had been washed and dried under vacuum, a ~10 mg piece of the polymer was removed and analyzed using ATR-IR on a Thermo-Nicolet IS-50 with a diamond crystal over a range of 4000 cm^2 to 400 cm^2. Spectra were then normalized and analyzed for changes in peaks at points of interest based on which reaction scheme was being used.

4.4.9.2 Gel Permeation Chromatography (GPC)

After the polymer was washed and dried, a small piece would be dissolved at a concentration of 10% w/v in THF and filtered through a 0.45 μm PVDF syringe filter. The dissolved polymer's molecular weight would then be measured with a Shimadzu GPC.

Chapter 5: Conclusions and Future Directions

This work was focused on designing polymer nanoparticles which would improve treatment options for ovarian cancer. The development and exploration of the wettability engendered templated self-assembly (WETS) method aimed to enable the undertaking of a systematic study of nanoparticle properties. By manufacturing nanoparticles with the same method and a systematic range of properties, studies of nanoparticle biodistributions, circulation half-lives and efficacy could be studied. This would increase the general understanding of nanoparticle drug delivery for the field, not just ovarian cancer. Co-delivery of drugs using a nanoparticle was studied as a method to treat ovarian cancer holistically. Cancer stem cells (CSC) dynamically interact with non-cancerous cells in their environment, and many of these interactions increase the malignancy of the cancer. Platelet derived growth factor (PDGF) was previously identified as a communication pathway between ovarian CSC and mesenchymal stem cells (MSC) which was implicated in higher CSC chemoresistance, ALDH activity and migration potential. Sunitinib, a tyrosine kinase inhibitor, was suggested as a potential treatment to stop this communication. PLGA nanoparticles encapsulating paclitaxel and sunitinib were electrosprayed and characterized in order to create a co-delivery nanoparticle which would be effective in reducing the effect that PDGF mediated MSC support would have on CSC. The nanoparticles could encapsulate both paclitaxel and sunitinib and were ~150-200 nm in diameter. Additionally, the effect of paclitaxel and sunitinib delivered in a 3D hanging drop *in vitro* model was investigated and found small trends suggesting that co-delivery could be an effective therapy for ovarian cancer. Nanoparticles were also designed to

encapsulate α-terpineol (αT), one of the active components of tea tree oil. αT has been shown to be more selective in killing cancerous cells than non-cancerous cells in ovarian cancer and when delivered as a free oil *in vitro,* caused significant death in OVCAR3. Electrosprayed nanoparticles can encapsulate αT which would increase the solubility and deliverability of the volatile, small molecule, however investigations to develop a method to conjugate αT to the PLGA carboxylic acid end groups were not successful.

5.1 WETS Future Directions

Drawbacks in the WETS method that were identified include: 1) the non-wetting, fluorinated silane was found to permit nanoscale fouling which rendered the background wettable on large scale substrates, 2) fabrication of nanoscale WETS substrates is difficult and 3) scale-up of WETS particle production needs to be greatly increased. Future work on WETS will need to focus on solving these issues as production will be extremely slow or impossible unless all three are addressed.

The fluorinated silane used in this work will need to be replaced completely with a silane that does not foul upon submersion in a polymer solution and can also fit within the existing WETS substrate lithography method. Suggested silanes to try include 1,3-PDMS, monochloro-flourinated silanes, and alkyl silanes as these silanes have shown promising contact angles and can be deposited using chemical vapor deposition. If the silane does not cleave from TiO_2 upon exposure to UV, the photoresist pattern will need to be reversed and patterned on a blanket of TiO_2. This method will be similar to the original WETS substrate fabrication except that the photomask pattern will need to be inverted, or the photoresist will need to undergo an image reversal protocol. Once the photoresist has been developed on a blanket of TiO_2, the substrate domains will be covered by the photoresist and the non-wetting background will be exposed. Silanize the non-

wetting background, then remove the photoresist to reveal the domains and expose to UV to make them wettable.

In order to optimize the stepper protocol to consistently fabricate nanoparticles with WETS, new masks will need to be designed with the appropriate guiding marks for a stepper. However, due to the photoresist and TiO_2 patterning, these guiding marks will also pattern polymer particles after dip-coating and steps will need to be taken to either remove the guiding marks before dip-coating or the larger particles will need to be removed after dip-coating. As the wettable domain gets smaller, the release layer will probably need to become thicker to ensure complete collection of the particles from the substrate.

Scale-up of WETS production will require larger substrates, however the cleanroom at the University of Michigan cannot support 6-inch or 12-inch wafers which would be the first next step. A collaboration with a cleanroom with larger capabilities might be possible if the stepper and silane protocols are finalized. Another method of scale up would be dip-coating multiple substrates at the same time into a larger polymer solution container, however the substrates faces would need to be held more than $2l_c$ apart in order to ensure that the solution recedes from all the substrates. One other method of scale-up would be to develop a roll-to-roll process similar to what is used by the particle replication in non-wetting templates (PRINT) technology[72,118].

With the WETS method currently, investigation into other applications such as biological sensors, optical devices, nanomotors and self-assembly could be beneficial. These uses might require fewer and larger particles which WETS is currently capable of.

5.2 Co-delivery Nanoparticles Future Directions

The limitation of slow fabrication is also present in electrospraying, however not as much as with WETS. Nanoparticle production through electrospraying can be increased through the

construction of ~7 more electrospray stations which can all be run in parallel to fabricate particles. A multiplex electrospray system, one with multiple needle outlets could be used to increase the rate of production at a single station[105]. The multiplex needle might need to be custom built and then would also require more frequent changes of the collection pan. An ideal set up would have a multiplex spray with a large solution syringe that sprayed onto a slow-moving conveyor belt for collection. This system would need a stable spray, but then could run without monitoring overnight or for a day to produce more particles easily. Two syringes on the same syringe pump, to roughly model a multiplex spray, was attempted, however the spray was not stable either due to each needle needing its own voltage source or the needles being too close together. An emulsion (much higher production yield) could also be tested to see if both drugs can be encapsulated, however removal of the poly(vinyl alcohol) emulsifier is extremely difficult which leads to particles that are 'glued' together after freeze drying. With an increase in nanoparticle fabrication, cell studies can be undertaken to study the efficacy of co-delivery.

Future work for the 3D hanging drop model needs to investigate the differences between the work here and that done previously in our lab[3]. One difference is the number of cells/well, where previously 12 cells/well were tested and in this work 400 cells/well were used in order to conduct experiments in a shorter time frame. The ratio (1:3) of CSC to MSC was maintained, but the large change in number of cells could have some effect and might be worth investigating. Another difficulty was the slow rate at which MSC grow and the ease with which they die compared to the CSC. One method of addressing this could be do use MSC condition media instead of a co-culture. Cell-cell connections and reciprocal signaling will be removed from the culture but using conditioned media could also help identify more specifics of how CSC and MSC communicate.

5.3 α-terpineol Nanoparticle Future Directions

Increased production of electrosprayed nanoparticles outlined in section 5.2 is also applicable to increasing the production of αT loaded nanoparticles for this work. Additionally the encapsulation of other essential oil components could be used for many applications other than cancer drug delivery including antimicrobial uses, cosmetics, antivirals, and antioxidants[119–122]. Further investigation of reaction schemes for a conjugated PLGA+αT could also look at other essential oil components such as perillyl alcohol as they may be better candidates for reacting. Perillyl alcohol was also tested against non-cancerous and ovarian cancer cells and was found to be more toxic towards non-cancerous cells so it was not fully investigated for conjugation. Future work on αT as a chemotherapeutic would need to explore and consider other factors such as metabolism, biodistribution, developed drug resistance and *in vivo* toxicity limit which could make αT unsuitable.

Bibliography

(1) Kobaku, S. P. R.; Kwon, G.; Kota, A. K.; Karunakaran, R. G.; Wong, P.; Lee, D. H.; Tuteja, A. Wettability Engendered Templated Self-Assembly (WETS) for Fabricating Multiphasic Particles. *ACS Appl. Mater. Interfaces* **2015**, *7* (7), 4075–4080. https://doi.org/10.1021/am507964k.

(2) Kobaku, S. P. R.; Snyder, C. S.; Karunakaran, R. G.; Kwon, G.; Wong, P.; Tuteja, A.; Mehta, G. Wettability Engendered Templated Self-Assembly (WETS) for the Fabrication of Biocompatible, Polymer–Polyelectrolyte Janus Particles. *ACS Macro Lett.* **2019**, *8* (11), 1491–1497. https://doi.org/10.1021/acsmacrolett.9b00493.

(3) Raghavan, S.; Snyder, C. S.; Wang, A.; McLean, K.; Zamarin, D.; Buckanovich, R. J.; Mehta, G. Carcinoma-Associated Mesenchymal Stem Cells Promote Chemoresistance in Ovarian Cancer Stem Cells via PDGF Signaling. *Cancers (Basel)* **2020**, *12* (8). https://doi.org/10.3390/cancers12082063.

(4) Siegel, R. L.; Miller, K. D.; Jemal, A. Cancer Statistics, 2020. *CA: A Cancer Journal for Clinicians* **2020**, *70* (1), 7–30. https://doi.org/10.3322/caac.21590.

(5) Thibault, B.; Castells, M.; Delord, J.-P.; Couderc, B. Ovarian Cancer Microenvironment: Implications for Cancer Dissemination and Chemoresistance Acquisition. *Cancer Metastasis Rev* **2014**, *33* (1), 17–39. https://doi.org/10.1007/s10555-013-9456-2.

(6) Al-Alem, L. F.; Pandya, U. M.; Baker, A. T.; Bellio, C.; Zarrella, B. D.; Clark, J.; DiGloria, C. M.; Rueda, B. R. Ovarian Cancer Stem Cells: What Progress Have We Made? *The International Journal of Biochemistry & Cell Biology* **2019**, *107*, 92–103. https://doi.org/10.1016/j.biocel.2018.12.010.

(7) Lupia, M.; Cavallaro, U. Ovarian Cancer Stem Cells: Still an Elusive Entity? *Molecular Cancer* **2017**, *16* (1), 64. https://doi.org/10.1186/s12943-017-0638-3.

(8) Steg, A. D.; Bevis, K. S.; Katre, A. A.; Ziebarth, A.; Alvarez, R. D.; Zhang, K.; Conner, M.; Landen, C. N. Stem Cell Pathways Contribute to Clinical Chemoresistance in Ovarian Cancer. *Clin Cancer Res* **2012**, *18* (3), 869–881. https://doi.org/10.1158/1078-0432.CCR-11-2188.

(9) Coffman, L. G.; Choi, Y.-J.; McLean, K.; Allen, B. L.; Magliano, M. P. di; Buckanovich, R. J. Human Carcinoma-Associated Mesenchymal Stem Cells Promote Ovarian Cancer Chemotherapy Resistance via a BMP4/HH Signaling Loop. *Oncotarget* **2016**, *7* (6), 6916–6932. https://doi.org/10.18632/oncotarget.6870.

(10) Raghavan, S.; Mehta, P.; Xie, Y.; Lei, Y. L.; Mehta, G. Ovarian Cancer Stem Cells and Macrophages Reciprocally Interact through the WNT Pathway to Promote Pro-Tumoral and Malignant Phenotypes in 3D Engineered Microenvironments. *Journal for ImmunoTherapy of Cancer* **2019**, *7* (1), 190. https://doi.org/10.1186/s40425-019-0666-1.

(11) Álvarez-Teijeiro, S.; García-Inclán, C.; Villaronga, M. Á.; Casado, P.; Hermida-Prado, F.; Granda-Díaz, R.; Rodrigo, J. P.; Calvo, F.; del-Río-Ibisate, N.; Gandarillas, A.; Morís, F.; Hermsen, M.; Cutillas, P.; García-Pedrero, J. M. Factors Secreted by Cancer-Associated Fibroblasts That Sustain Cancer Stem Properties in Head and Neck Squamous Carcinoma

Cells as Potential Therapeutic Targets. *Cancers (Basel)* **2018**, *10* (9). https://doi.org/10.3390/cancers10090334.
(12) Bregenzer, M. E.; Horst, E. N.; Mehta, P.; Novak, C. M.; Raghavan, S.; Snyder, C. S.; Mehta, G. Integrated Cancer Tissue Engineering Models for Precision Medicine. *PLOS ONE* **2019**, *14* (5), e0216564. https://doi.org/10.1371/journal.pone.0216564.
(13) Nowak, M.; Klink, M. The Role of Tumor-Associated Macrophages in the Progression and Chemoresistance of Ovarian Cancer. *Cells* **2020**, *9* (5). https://doi.org/10.3390/cells9051299.
(14) Dasari, S.; Fang, Y.; K. Mitra, A. Cancer Associated Fibroblasts: Naughty Neighbors That Drive Ovarian Cancer Progression. *Cancers (Basel)* **2018**, *10* (11). https://doi.org/10.3390/cancers10110406.
(15) McLean, K.; Gong, Y.; Choi, Y.; Deng, N.; Yang, K.; Bai, S.; Cabrera, L.; Keller, E.; McCauley, L.; Cho, K. R.; Buckanovich, R. J. Human Ovarian Carcinoma–Associated Mesenchymal Stem Cells Regulate Cancer Stem Cells and Tumorigenesis via Altered BMP Production. *J Clin Invest* **2011**, *121* (8), 3206–3219. https://doi.org/10.1172/JCI45273.
(16) Castells, M.; Milhas, D.; Gandy, C.; Thibault, B.; Rafii, A.; Delord, J.-P.; Couderc, B. Microenvironment Mesenchymal Cells Protect Ovarian Cancer Cell Lines from Apoptosis by Inhibiting XIAP Inactivation. *Cell Death Dis* **2013**, *4* (10), e887. https://doi.org/10.1038/cddis.2013.384.
(17) Zhang, Y.; Dong, W.; Wang, J.; Cai, J.; Wang, Z. Human Omental Adipose-Derived Mesenchymal Stem Cell-Conditioned Medium Alters the Proteomic Profile of Epithelial Ovarian Cancer Cell Lines in Vitro. *OncoTargets and Therapy* **2017**. https://doi.org/10.2147/OTT.S129502.
(18) Ding, D.-C.; Liu, H.-W.; Chu, T.-Y. Interleukin-6 from Ovarian Mesenchymal Stem Cells Promotes Proliferation, Sphere and Colony Formation and Tumorigenesis of an Ovarian Cancer Cell Line SKOV3. *J Cancer* **2016**, *7* (13), 1815–1823. https://doi.org/10.7150/jca.16116.
(19) Paoletti, X.; Lewsley, L.-A.; Daniele, G.; Cook, A.; Yanaihara, N.; Tinker, A.; Kristensen, G.; Ottevanger, P. B.; Aravantinos, G.; Miller, A.; Boere, I. A.; Fruscio, R.; Reyners, A. K. L.; Pujade-Lauraine, E.; Harkin, A.; Pignata, S.; Kagimura, T.; Welch, S.; Paul, J.; Karamouza, E.; Glasspool, R. M.; for the Gynecologic Cancer InterGroup (GCIG) Meta-analysis Committee. Assessment of Progression-Free Survival as a Surrogate End Point of Overall Survival in First-Line Treatment of Ovarian Cancer: A Systematic Review and Meta-Analysis. *JAMA Network Open* **2020**, *3* (1), e1918939–e1918939. https://doi.org/10.1001/jamanetworkopen.2019.18939.
(20) Ghoneum, A.; Afify, H.; Salih, Z.; Kelly, M.; Said, N. Role of Tumor Microenvironment in Ovarian Cancer Pathobiology. *Oncotarget* **2018**, *9* (32), 22832–22849. https://doi.org/10.18632/oncotarget.25126.
(21) Tsai, L.-Y.; Tsai, J.-M.; Tsay, S.-L. Life Experiences and Disease Trajectories in Women Coexisting with Ovarian Cancer. *Taiwanese Journal of Obstetrics and Gynecology* **2020**, *59* (1), 115–119. https://doi.org/10.1016/j.tjog.2019.11.032.
(22) Matsumura, Y.; Maeda, H. A New Concept for Macromolecular Therapeutics in Cancer Chemotherapy: Mechanism of Tumoritropic Accumulation of Proteins and the Antitumor Agent Smancs. *Cancer Res* **1986**, *46* (12 Part 1), 6387–6392.
(23) Strebhardt, K.; Ullrich, A. Paul Ehrlich's Magic Bullet Concept: 100 Years of Progress. *Nature Reviews Cancer* **2008**, *8* (6), 473–480. https://doi.org/10.1038/nrc2394.

(24) Acharya, S.; Sahoo, S. K. PLGA Nanoparticles Containing Various Anticancer Agents and Tumour Delivery by EPR Effect. *Advanced Drug Delivery Reviews* **2011**, *63* (3), 170–183. https://doi.org/10.1016/j.addr.2010.10.008.
(25) Maeda, H.; Fang, J.; Inutsuka, T.; Kitamoto, Y. Vascular Permeability Enhancement in Solid Tumor: Various Factors, Mechanisms Involved and Its Implications. *International Immunopharmacology* **2003**, *3* (3), 319–328. https://doi.org/10.1016/S1567-5769(02)00271-0.
(26) Sharma, S.; Parmar, A.; Kori, S.; Sandhir, R. PLGA-Based Nanoparticles: A New Paradigm in Biomedical Applications. *TrAC Trends in Analytical Chemistry* **2016**, *80*, 30–40. https://doi.org/10.1016/j.trac.2015.06.014.
(27) Young, S. W. S.; Stenzel, M.; Jia-Lin, Y. Nanoparticle-SiRNA: A Potential Cancer Therapy? *Critical Reviews in Oncology/Hematology* **2016**, *98*, 159–169. https://doi.org/10.1016/j.critrevonc.2015.10.015.
(28) Anselmo, A. C.; Mitragotri, S. Nanoparticles in the Clinic. *Bioeng Transl Med* **2016**, *1* (1), 10–29. https://doi.org/10.1002/btm2.10003.
(29) Anselmo, A. C.; Mitragotri, S. Nanoparticles in the Clinic: An Update. *Bioengineering & Translational Medicine* **2019**, *4* (3), e10143. https://doi.org/10.1002/btm2.10143.
(30) Lammers, T.; Kiessling, F.; Hennink, W. E.; Storm, G. Drug Targeting to Tumors: Principles, Pitfalls and (Pre-) Clinical Progress. *Journal of Controlled Release* **2012**, *161* (2), 175–187. https://doi.org/10.1016/j.jconrel.2011.09.063.
(31) Park, K.; Bae, Y. H.; Mrsny, R. J. The Missing Components Today and the New Treatments Tomorrow. In *Cancer Targeted Drug Delivery: An Elusive Dream*; Bae, Y. H., Mrsny, R. J., Park, K., Eds.; Springer: New York, NY, 2013; pp 689–707. https://doi.org/10.1007/978-1-4614-7876-8_26.
(32) Danhier, F. To Exploit the Tumor Microenvironment: Since the EPR Effect Fails in the Clinic, What Is the Future of Nanomedicine? *Journal of Controlled Release* **2016**, *244*, 108–121. https://doi.org/10.1016/j.jconrel.2016.11.015.
(33) Petros, R. A.; DeSimone, J. M. Strategies in the Design of Nanoparticles for Therapeutic Applications. *Nature Reviews Drug Discovery* **2010**, *9* (8), 615–627. https://doi.org/10.1038/nrd2591.
(34) Wilhelm, S.; Tavares, A. J.; Dai, Q.; Ohta, S.; Audet, J.; Dvorak, H. F.; Chan, W. C. W. Analysis of Nanoparticle Delivery to Tumours. *Nat Rev Mater* **2016**, *1* (5), 1–12. https://doi.org/10.1038/natrevmats.2016.14.
(35) Dai, Q.; Wilhelm, S.; Ding, D.; Syed, A. M.; Sindhwani, S.; Zhang, Y.; Chen, Y. Y.; MacMillan, P.; Chan, W. C. W. Quantifying the Ligand-Coated Nanoparticle Delivery to Cancer Cells in Solid Tumors. *ACS Nano* **2018**, *12* (8), 8423–8435. https://doi.org/10.1021/acsnano.8b03900.
(36) Vedhanayagam, M.; Nidhin, M.; Duraipandy, N.; Naresh, N. D.; Jaganathan, G.; Ranganathan, M.; Kiran, M. S.; Narayan, S.; Nair, B. U.; Sreeram, K. J. Role of Nanoparticle Size in Self-Assemble Processes of Collagen for Tissue Engineering Application. *International Journal of Biological Macromolecules* **2017**, *99*, 655–664. https://doi.org/10.1016/j.ijbiomac.2017.02.102.
(37) Fathi-Achachelouei, M.; Knopf-Marques, H.; Ribeiro da Silva, C. E.; Barthès, J.; Bat, E.; Tezcaner, A.; Vrana, N. E. Use of Nanoparticles in Tissue Engineering and Regenerative Medicine. *Front Bioeng Biotechnol* **2019**, *7*. https://doi.org/10.3389/fbioe.2019.00113.

(38) Pu, K.; Chattopadhyay, N.; Rao, J. Recent Advances of Semiconducting Polymer Nanoparticles in in Vivo Molecular Imaging. *Journal of Controlled Release* **2016**, *240*, 312–322. https://doi.org/10.1016/j.jconrel.2016.01.004.
(39) Avramović, N.; Mandić, B.; Savić-Radojević, A.; Simić, T. Polymeric Nanocarriers of Drug Delivery Systems in Cancer Therapy. *Pharmaceutics* **2020**, *12* (4), 298. https://doi.org/10.3390/pharmaceutics12040298.
(40) Lima, A. C.; Alvarez-Lorenzo, C.; Mano, J. F. Design Advances in Particulate Systems for Biomedical Applications. *Advanced Healthcare Materials* **2016**, *5* (14), 1687–1723. https://doi.org/10.1002/adhm.201600219.
(41) Mitragotri, S.; Stayton, P. Organic Nanoparticles for Drug Delivery and Imaging. *MRS Bulletin* **2014**, *39* (3), 219–223. https://doi.org/10.1557/mrs.2014.11.
(42) Lee, W. L.; Loo, S. C. J. Revolutionizing Drug Delivery through Biodegradable Multilayered Particles. *Journal of Drug Targeting* **2012**, *20* (8), 633–647. https://doi.org/10.3109/1061186X.2012.702772.
(43) Sanchez, L.; Yi, Y.; Yu, Y. Effect of Partial PEGylation on Particle Uptake by Macrophages. *Nanoscale* **2017**, *9* (1), 288–297. https://doi.org/10.1039/c6nr07353k.
(44) Chang, F.; van Ravensteijn, B. G. P.; Lacina, K. S.; Kegel, W. K. Bifunctional Janus Spheres with Chemically Orthogonal Patches. *ACS Macro Lett.* **2019**, *8* (6), 714–718. https://doi.org/10.1021/acsmacrolett.9b00193.
(45) Tang, J. L.; Schoenwald, K.; Potter, D.; White, D.; Sulchek, T. Bifunctional Janus Microparticles with Spatially Segregated Proteins. *Langmuir* **2012**, *28* (26), 10033–10039. https://doi.org/10.1021/la3010079.
(46) Garbuzenko, O. B.; Winkler, J.; Tomassone, M. S.; Minko, T. Biodegradable Janus Nanoparticles for Local Pulmonary Delivery of Hydrophilic and Hydrophobic Molecules to the Lungs. *Langmuir* **2014**, *30* (43), 12941–12949. https://doi.org/10.1021/la502144z.
(47) Indoria, S.; Singh, V.; Hsieh, M.-F. Recent Advances in Theranostic Polymeric Nanoparticles for Cancer Treatment: A Review. *International Journal of Pharmaceutics* **2020**, *582*, 119314. https://doi.org/10.1016/j.ijpharm.2020.119314.
(48) Chen, Q.; Bae, S. C.; Granick, S. Directed Self-Assembly of a Colloidal Kagome Lattice. *Nature* **2011**, *469* (7330), 381–384. https://doi.org/10.1038/nature09713.
(49) Zhang, Z.; Pfleiderer, P.; Schofield, A. B.; Clasen, C.; Vermant, J. Synthesis and Directed Self-Assembly of Patterned Anisometric Polymeric Particles. *J. Am. Chem. Soc.* **2011**, *133* (3), 392–395. https://doi.org/10.1021/ja108099r.
(50) Nguyen, T. D.; Jankowski, E.; Glotzer, S. C. Self-Assembly and Reconfigurability of Shape-Shifting Particles. *ACS Nano* **2011**, *5* (11), 8892–8903. https://doi.org/10.1021/nn203067y.
(51) Marson, R. L.; Nguyen, T. D.; Glotzer, S. C. Rational Design of Nanomaterials from Assembly and Reconfigurability of Polymer-Tethered Nanoparticles. *MRS Communications* **2015**, *5* (3), 397–406. https://doi.org/10.1557/mrc.2015.54.
(52) Youssef, M.; Hueckel, T.; Yi, G.-R.; Sacanna, S. Shape-Shifting Colloids via Stimulated Dewetting. *Nature Communications* **2016**, *7*, 12216. https://doi.org/10.1038/ncomms12216.
(53) Stuart, M. A. C.; Huck, W. T. S.; Genzer, J.; Müller, M.; Ober, C.; Stamm, M.; Sukhorukov, G. B.; Szleifer, I.; Tsukruk, V. V.; Urban, M.; Winnik, F.; Zauscher, S.; Luzinov, I.; Minko, S. Emerging Applications of Stimuli-Responsive Polymer Materials. *Nature Materials* **2010**, *9* (2), 101–113. https://doi.org/10.1038/nmat2614.
(54) Synytska, A.; Ionov, L. Stimuli-Responsive Janus Particles. *Particle & Particle Systems Characterization* **2013**, *30* (11), 922–930. https://doi.org/10.1002/ppsc.201300146.

(55) Lee, K. J.; Yoon, J.; Rahmani, S.; Hwang, S.; Bhaskar, S.; Mitragotri, S.; Lahann, J. Spontaneous Shape Reconfigurations in Multicompartmental Microcylinders. *PNAS* **2012**, *109* (40), 16057–16062. https://doi.org/10.1073/pnas.1213669109.
(56) Topham, P. D.; Howse, J. R.; Crook, C. J.; Armes, S. P.; Jones, R. A. L.; Ryan, A. J. Antagonistic Triblock Polymer Gels Powered by PH Oscillations. *Macromolecules* **2007**, *40* (13), 4393–4395. https://doi.org/10.1021/ma071041j.
(57) Yoo, J.-W.; Irvine, D. J.; Discher, D. E.; Mitragotri, S. Bio-Inspired, Bioengineered and Biomimetic Drug Delivery Carriers. *Nature Reviews Drug Discovery* **2011**, *10* (7), 521–535. https://doi.org/10.1038/nrd3499.
(58) Yoo, J.-W.; Mitragotri, S. Polymer Particles That Switch Shape in Response to a Stimulus. *PNAS* **2010**, *107* (25), 11205–11210. https://doi.org/10.1073/pnas.1000346107.
(59) Yoo, J.-W.; Doshi, N.; Mitragotri, S. Adaptive Micro and Nanoparticles: Temporal Control over Carrier Properties to Facilitate Drug Delivery. *Advanced Drug Delivery Reviews* **2011**, *63* (14), 1247–1256. https://doi.org/10.1016/j.addr.2011.05.004.
(60) Geng, Y.; Dalhaimer, P.; Cai, S.; Tsai, R.; Tewari, M.; Minko, T.; Discher, D. E. Shape Effects of Filaments versus Spherical Particles in Flow and Drug Delivery. *Nat Nanotechnol* **2007**, *2* (4), 249–255. https://doi.org/10.1038/nnano.2007.70.
(61) Champion, J. A.; Mitragotri, S. Role of Target Geometry in Phagocytosis. *Proc Natl Acad Sci U S A* **2006**, *103* (13), 4930–4934. https://doi.org/10.1073/pnas.0600997103.
(62) Shi, J.; Choi, J. L.; Chou, B.; Johnson, R. N.; Schellinger, J. G.; Pun, S. H. Effect of Polyplex Morphology on Cellular Uptake, Intracellular Trafficking, and Transgene Expression. *ACS Nano* **2013**, *7* (12). https://doi.org/10.1021/nn403069n.
(63) Hoshyar, N.; Gray, S.; Han, H.; Bao, G. The Effect of Nanoparticle Size on in Vivo Pharmacokinetics and Cellular Interaction. *Nanomedicine (Lond)* **2016**, *11* (6), 673–692. https://doi.org/10.2217/nnm.16.5.
(64) Chu, K. S.; Hasan, W.; Rawal, S.; Walsh, M. D.; Enlow, E. M.; Luft, J. C.; Bridges, A. S.; Kuijer, J. L.; Napier, M. E.; Zamboni, W. C.; DeSimone, J. M. Plasma, Tumor and Tissue Pharmacokinetics of Docetaxel Delivered via Nanoparticles of Different Sizes and Shapes in Mice Bearing SKOV-3 Human Ovarian Carcinoma Xenograft. *Nanomedicine: Nanotechnology, Biology and Medicine* **2013**, *9* (5), 686–693. https://doi.org/10.1016/j.nano.2012.11.008.
(65) Rahmani, S.; Lahann, J. Recent Progress with Multicompartmental Nanoparticles. *MRS Bulletin* **2014**, *39* (3), 251–257. https://doi.org/10.1557/mrs.2014.10.
(66) Wang, Y.; Zhang, Y.; Wang, B.; Cao, Y.; Yu, Q.; Yin, T. Fabrication of Core–Shell Micro/Nanoparticles for Programmable Dual Drug Release by Emulsion Electrospraying. *J Nanopart Res* **2013**, *15* (6), 1726. https://doi.org/10.1007/s11051-013-1726-y.
(67) Salvador-Morales, C.; Brahmbhatt, B.; Márquez-Miranda, V.; Araya-Duran, I.; Canan, J.; Gonzalez-Nilo, F.; Vilos, C.; Cebral, J.; Mut, F.; Lohner, R.; Leong, B.; Sundaresan, G.; Zweit, J. Mechanistic Studies on the Self-Assembly of PLGA Patchy Particles and Their Potential Applications in Biomedical Imaging. *Langmuir* **2016**, *32* (31), 7929–7942. https://doi.org/10.1021/acs.langmuir.6b02177.
(68) Bhaskar, S.; Pollock, K. M.; Yoshida, M.; Lahann, J. Towards Designer Microparticles: Simultaneous Control of Anisotropy, Shape, and Size. *Small* **2010**, *6* (3), 404–411. https://doi.org/10.1002/smll.200901306.

(69) Pawar, A. B.; Kretzschmar, I. Fabrication, Assembly, and Application of Patchy Particles. *Macromolecular Rapid Communications* **2010**, *31* (2), 150–168. https://doi.org/10.1002/marc.200900614.
(70) Xie, H.; She, Z.-G.; Wang, S.; Sharma, G.; Smith, J. W. One-Step Fabrication of Polymeric Janus Nanoparticles for Drug Delivery. *Langmuir* **2012**, *28* (9), 4459–4463. https://doi.org/10.1021/la2042185.
(71) Jang, J.-H.; Dendukuri, D.; Hatton, T. A.; Thomas, E. L.; Doyle, P. S. A Route to Three-Dimensional Structures in a Microfluidic Device: Stop-Flow Interference Lithography. *Angewandte Chemie International Edition* **2007**, *46* (47), 9027–9031. https://doi.org/10.1002/anie.200703525.
(72) DeSimone, J. M. Co-Opting Moore's Law: Therapeutics, Vaccines and Interfacially Active Particles Manufactured via PRINT®. *Journal of Controlled Release* **2016**, *240*, 541–543. https://doi.org/10.1016/j.jconrel.2016.07.019.
(73) Perry, J. L.; Herlihy, K. P.; Napier, M. E.; DeSimone, J. M. PRINT: A Novel Platform Toward Shape and Size Specific Nanoparticle Theranostics. *Acc Chem Res* **2011**, *44* (10), 990–998. https://doi.org/10.1021/ar2000315.
(74) Wang, J.-Y.; Wang, Y.; Sheiko, S. S.; Betts, D. E.; DeSimone, J. M. Tuning Multiphase Amphiphilic Rods to Direct Self-Assembly. *J. Am. Chem. Soc.* **2012**, *134* (13), 5801–5806. https://doi.org/10.1021/ja2066187.
(75) Xu, J.; Wong, D. H. C.; Byrne, J. D.; Chen, K.; Bowerman, C.; DeSimone, J. M. Future of the Particle Replication in Nonwetting Templates (PRINT) Technology. *Angew Chem Int Ed Engl* **2013**, *52* (26), 6580–6589. https://doi.org/10.1002/anie.201209145.
(76) Kobayashi, H.; Watanabe, R.; Choyke, P. L. Improving Conventional Enhanced Permeability and Retention (EPR) Effects; What Is the Appropriate Target? *Theranostics* **2013**, *4* (1), 81–89. https://doi.org/10.7150/thno.7193.
(77) Bose, T.; Latawiec, D.; Mondal, P. P.; Mandal, S. Overview of Nano-Drugs Characteristics for Clinical Application: The Journey from the Entry to the Exit Point. *J Nanopart Res* **2014**, *16* (8), 2527. https://doi.org/10.1007/s11051-014-2527-7.
(78) Torza, S.; Mason, S. G. Coalescence of Two Immiscible Liquid Drops. *Science* **1969**, *163* (3869), 813–814. https://doi.org/10.1126/science.163.3869.813.
(79) Mayer, S. W. Dependence of Surface Tension on Temperature. *J. Chem. Phys.* **1963**, *38* (8), 1803–1808. https://doi.org/10.1063/1.1733879.
(80) Glycerine Producers' Association. *Physical Properties of Glycerine and Its Solutions*; Glycerine Producers' Association: New York, NY, 1963.
(81) Wu, S. Interfacial and Surface Tensions of Polymers. *Journal of Macromolecular Science, Part C* **1974**, *10* (1), 1–73. https://doi.org/10.1080/15321797408080004.
(82) Wu, S. Calculation of Interfacial Tension in Polymer Systems. *Journal of Polymer Science Part C: Polymer Symposia* **1971**, *34* (1), 19–30. https://doi.org/10.1002/polc.5070340105.
(83) Gratton, S. E. A.; Pohlhaus, P. D.; Lee, J.; Guo, J.; Cho, M. J.; DeSimone, J. M. Nanofabricated Particles for Engineered Drug Therapies: A Preliminary Biodistribution Study of PRINT™ Nanoparticles. *J Control Release* **2007**, *121* (1–2), 10–18. https://doi.org/10.1016/j.jconrel.2007.05.027.
(84) Danhier, F.; Lecouturier, N.; Vroman, B.; Jérôme, C.; Marchand-Brynaert, J.; Feron, O.; Préat, V. Paclitaxel-Loaded PEGylated PLGA-Based Nanoparticles: In Vitro and in Vivo Evaluation. *Journal of Controlled Release* **2009**, *133* (1), 11–17. https://doi.org/10.1016/j.jconrel.2008.09.086.

(85) Maji, R.; Dey, N. S.; Satapathy, B. S.; Mukherjee, B.; Mondal, S. Preparation and Characterization of Tamoxifen Citrate Loaded Nanoparticles for Breast Cancer Therapy. *Int J Nanomedicine* **2014**, *9*, 3107–3118. https://doi.org/10.2147/IJN.S63535.
(86) Liu, L.; Cao, F.; Liu, X.; Wang, H.; Zhang, C.; Sun, H.; Wang, C.; Leng, X.; Song, C.; Kong, D.; Ma, G. Hyaluronic Acid-Modified Cationic Lipid–PLGA Hybrid Nanoparticles as a Nanovaccine Induce Robust Humoral and Cellular Immune Responses. *ACS Appl. Mater. Interfaces* **2016**, *8* (19), 11969–11979. https://doi.org/10.1021/acsami.6b01135.
(87) Stack, M. S.; Nephew, K. P.; Burdette, J. E.; K. Mitra, A. The Tumor Microenvironment of High Grade Serous Ovarian Cancer. *Cancers (Basel)* **2018**, *11* (1). https://doi.org/10.3390/cancers11010021.
(88) Zhang, B.; Chen, F.; Xu, Q.; Han, L.; Xu, J.; Gao, L.; Sun, X.; Li, Y.; Li, Y.; Qian, M.; Sun, Y. Revisiting Ovarian Cancer Microenvironment: A Friend or a Foe? *Protein Cell* **2018**, *9* (8), 674–692. https://doi.org/10.1007/s13238-017-0466-7.
(89) Silva, I. A.; Bai, S.; McLean, K.; Yang, K.; Griffith, K.; Thomas, D.; Ginestier, C.; Johnston, C.; Kueck, A.; Reynolds, R. K.; Wicha, M. S.; Buckanovich, R. J. Aldehyde Dehydrogenase in Combination with CD133 Defines Angiogenic Ovarian Cancer Stem Cells That Portend Poor Patient Survival. *Cancer Res* **2011**, *71* (11), 3991–4001. https://doi.org/10.1158/0008-5472.CAN-10-3175.
(90) Landen, C. N.; Goodman, B.; Katre, A. A.; Steg, A. D.; Nick, A. M.; Stone, R. L.; Miller, L. D.; Mejia, P. V.; Jennings, N. B.; Gershenson, D. M.; Bast, R. C.; Coleman, R. L.; Lopez-Berestein, G.; Sood, A. K. Targeting Aldehyde Dehydrogenase Cancer Stem Cells in Ovarian Cancer. *Mol Cancer Ther* **2010**, *9* (12), 3186–3199. https://doi.org/10.1158/1535-7163.MCT-10-0563.
(91) Zhang, J.; Guo, X.; Chang, D. Y.; Rosen, D. G.; Mercado-Uribe, I.; Liu, J. CD133 Expression Associated with Poor Prognosis in Ovarian Cancer. *Mod Pathol* **2012**, *25* (3). https://doi.org/10.1038/modpathol.2011.170.
(92) Curley, M. D.; Therrien, V. A.; Cummings, C. L.; Sergent, P. A.; Koulouris, C. R.; Friel, A. M.; Roberts, D. J.; Seiden, M. V.; Scadden, D. T.; Rueda, B. R.; Foster, R. CD133 Expression Defines a Tumor Initiating Cell Population in Primary Human Ovarian Cancer. *Stem Cells* **2009**, *27* (12), 2875–2883. https://doi.org/10.1002/stem.236.
(93) Sharrow, A. C.; Perkins, B.; Collector, M. I.; Yu, W.; Simons, B. W.; Jones, R. J. Characterization of Aldehyde Dehydrogenase 1 High Ovarian Cancer Cells: Towards Targeted Stem Cell Therapy. *Gynecol Oncol* **2016**, *142* (2), 341–348. https://doi.org/10.1016/j.ygyno.2016.03.022.
(94) Kryczek, I.; Liu, S.; Roh, M.; Vatan, L.; Szeliga, W.; Wei, S.; Banerjee, M.; Mao, Y.; Kotarski, J.; Wicha, M. S.; Liu, R.; Zou, W. Expression of Aldehyde Dehydrogenase and CD133 Defines Ovarian Cancer Stem Cells. *Int J Cancer* **2012**, *130* (1), 29–39. https://doi.org/10.1002/ijc.25967.
(95) Cho, J. A.; Park, H.; Lim, E. H.; Kim, K. H.; Choi, J. S.; Lee, J. H.; Shin, J. W.; Lee, K. W. Exosomes from Ovarian Cancer Cells Induce Adipose Tissue-Derived Mesenchymal Stem Cells to Acquire the Physical and Functional Characteristics of Tumor-Supporting Myofibroblasts. *Gynecologic Oncology* **2011**, *123* (2), 379–386. https://doi.org/10.1016/j.ygyno.2011.08.005.
(96) Karnoub, A. E.; Dash, A. B.; Vo, A. P.; Sullivan, A.; Brooks, M. W.; Bell, G. W.; Richardson, A. L.; Polyak, K.; Tubo, R.; Weinberg, R. A. Mesenchymal Stem Cells within Tumour

Stroma Promote Breast Cancer Metastasis. *Nature* **2007**, *449* (7162), 557–563. https://doi.org/10.1038/nature06188.
(97) Fonseca, C.; Simões, S.; Gaspar, R. Paclitaxel-Loaded PLGA Nanoparticles: Preparation, Physicochemical Characterization and in Vitro Anti-Tumoral Activity. *Journal of Controlled Release* **2002**, *83* (2), 273–286. https://doi.org/10.1016/S0168-3659(02)00212-2.
(98) Li, M.; Czyszczon, E. A.; Reineke, J. J. Delineating Intracellular Pharmacokinetics of Paclitaxel Delivered by PLGA Nanoparticles. *Drug Deliv. and Transl. Res.* **2013**, *3* (6), 551–561. https://doi.org/10.1007/s13346-013-0162-y.
(99) Mu, L.; Feng, S. S. A Novel Controlled Release Formulation for the Anticancer Drug Paclitaxel (Taxol®): PLGA Nanoparticles Containing Vitamin E TPGS. *Journal of Controlled Release* **2003**, *86* (1), 33–48. https://doi.org/10.1016/S0168-3659(02)00320-6.
(100) Alshetaili, A. S.; Anwer, M. K.; Alshahrani, S. M.; Alalaiwe, A.; Alsulays, B. B.; Ansari, M. J.; Imam, F.; Alshehri, S. Characteristics and Anticancer Properties of Sunitinib Malate-Loaded Poly-Lactic-Co-Glycolic Acid Nanoparticles against Human Colon Cancer HT-29 Cells Lines. *Tropical Journal of Pharmaceutical Research* **2018**, *17* (7), 1263–1269. https://doi.org/10.4314/tjpr.v17i7.
(101) Joseph, J. J.; Sangeetha, D.; Gomathi, T. Sunitinib Loaded Chitosan Nanoparticles Formulation and Its Evaluation. *International Journal of Biological Macromolecules* **2016**, *82*, 952–958. https://doi.org/10.1016/j.ijbiomac.2015.10.079.
(102) Saber, M. M.; Bahrainian, S.; Dinarvand, R.; Atyabi, F. Targeted Drug Delivery of Sunitinib Malate to Tumor Blood Vessels by CRGD-Chiotosan-Gold Nanoparticles. *International Journal of Pharmaceutics* **2017**, *517* (1), 269–278. https://doi.org/10.1016/j.ijpharm.2016.12.016.
(103) Dudek, A. Z.; Nguyen, S. Safety of Nab-Paclitaxel plus Sunitinib: Analysis of Three Cases. *Anticancer Res* **2008**, *28* (5B), 3099–3105.
(104) Mrozik, K. M.; Blaschuk, O. W.; Cheong, C. M.; Zannettino, A. C. W.; Vandyke, K. N-Cadherin in Cancer Metastasis, Its Emerging Role in Haematological Malignancies and Potential as a Therapeutic Target in Cancer. *BMC Cancer* **2018**, *18* (1), 939. https://doi.org/10.1186/s12885-018-4845-0.
(105) Almería, B.; Fahmy, T. M.; Gomez, A. A Multiplexed Electrospray Process for Single-Step Synthesis of Stabilized Polymer Particles for Drug Delivery. *Journal of Controlled Release* **2011**, *154* (2), 203–210. https://doi.org/10.1016/j.jconrel.2011.05.018.
(106) Livak, K. J.; Schmittgen, T. D. Analysis of Relative Gene Expression Data Using Real-Time Quantitative PCR and the 2(-Delta Delta C(T)) Method. *Methods* **2001**, *25* (4), 402–408. https://doi.org/10.1006/meth.2001.1262.
(107) Ford, C. E.; Werner, B.; Hacker, N. F.; Warton, K. The Untapped Potential of Ascites in Ovarian Cancer Research and Treatment. *British Journal of Cancer* **2020**, *123* (1), 9–16. https://doi.org/10.1038/s41416-020-0875-x.
(108) Sobral, M. V.; Xavier, A. L.; Lima, T. C.; de Sousa, D. P. Antitumor Activity of Monoterpenes Found in Essential Oils. *ScientificWorldJournal* **2014**, *2014*. https://doi.org/10.1155/2014/953451.
(109) Assmann, C. E.; Cadoná, F. C.; Bonadiman, B. da S. R.; Dornelles, E. B.; Trevisan, G.; Cruz, I. B. M. da. Tea Tree Oil Presents in Vitro Antitumor Activity on Breast Cancer Cells without Cytotoxic Effects on Fibroblasts and on Peripheral Blood Mononuclear Cells. *Biomedicine & Pharmacotherapy* **2018**, *103*, 1253–1261. https://doi.org/10.1016/j.biopha.2018.04.096.

(110) Greay, S. J.; Ireland, D. J.; Kissick, H. T.; Levy, A.; Beilharz, M. W.; Riley, T. V.; Carson, C. F. Induction of Necrosis and Cell Cycle Arrest in Murine Cancer Cell Lines by Melaleuca Alternifolia (Tea Tree) Oil and Terpinen-4-Ol. *Cancer Chemother Pharmacol* **2010**, *65* (5), 877–888. https://doi.org/10.1007/s00280-009-1093-7.

(111) Hatada, K.; Ute, K.; Oka, K.-I.; Pappas, S. P. Unambiguous 13C-NMR Assignments for Isocyanate Carbons of Isophorone Diisocyanate and Reactivity of Isocyanate Groups in Z - and E-Stereoisomers. *Journal of Polymer Science Part A: Polymer Chemistry* **1990**, *28* (11), 3019–3027. https://doi.org/10.1002/pola.1990.080281111.

(112) Ono, H.-K.; Jones, F. N.; Pappas, S. P. Relative Reactivity of Isocyanate Groups of Isophorone Diisocyanate. Unexpected High Reactivity of the Secondary Isocyanate Group. *Journal of Polymer Science: Polymer Letters Edition* **1985**, *23* (10), 509–515. https://doi.org/10.1002/pol.1985.130231003.

(113) Meneghetti, M. R.; Meneghetti, S. M. P. Sn(IV)-Based Organometallics as Catalysts for the Production of Fatty Acid Alkyl Esters. *Catal. Sci. Technol.* **2015**, *5* (2), 765–771. https://doi.org/10.1039/C4CY01535E.

(114) Gürtler, C.; Danielmeier, K. A Catalyst System for the Reaction of Carboxylic Acids with Aliphatic Isocyanates. *Tetrahedron Letters* **2004**, *45* (12), 2515–2521. https://doi.org/10.1016/j.tetlet.2004.02.012.

(115) Götz, H.; Beginn, U.; Bartelink, C. F.; Grünbauer, H. J. M.; Möller, M. Preparation of Isophorone Diisocyanate Terminated Star Polyethers. *Macromolecular Materials and Engineering* **2002**, *287* (4), 223–230. https://doi.org/10.1002/1439-2054(20020401)287:4<223::AID-MAME223>3.0.CO;2-Z.

(116) Silva, M. J. da; Ayala, D. a. M. Unravelling Transition Metal-Catalyzed Terpenic Alcohol Esterification: A Straightforward Process for the Synthesis of Fragrances. *Catal. Sci. Technol.* **2016**, *6* (9), 3197–3207. https://doi.org/10.1039/C5CY01538C.

(117) Kabalka, G. W.; Varma, M.; Varma, R. S.; Srivastava, P. C.; Knapp, F. F. The Tosylation of Alcohols. *J. Org. Chem.* **1986**, *51* (12), 2386–2388. https://doi.org/10.1021/jo00362a044.

(118) Rolland, J. P.; Maynor, B. W.; Euliss, L. E.; Exner, A. E.; Denison, G. M.; DeSimone, J. M. Direct Fabrication and Harvesting of Monodisperse, Shape-Specific Nanobiomaterials. *J. Am. Chem. Soc.* **2005**, *127* (28), 10096–10100. https://doi.org/10.1021/ja051977c.

(119) Manea, A.-M.; Vasile, B. S.; Meghea, A. Antioxidant and Antimicrobial Activities of Green Tea Extract Loaded into Nanostructured Lipid Carriers. *Comptes Rendus Chimie* **2014**, *17* (4), 331–341. https://doi.org/10.1016/j.crci.2013.07.015.

(120) Han, H. J.; Lee, J.-S.; Park, S.-A.; Ahn, J.-B.; Lee, H. G. Extraction Optimization and Nanoencapsulation of Jujube Pulp and Seed for Enhancing Antioxidant Activity. *Colloids and Surfaces B: Biointerfaces* **2015**, *130*, 93–100. https://doi.org/10.1016/j.colsurfb.2015.03.050.

(121) Sinico, C.; De Logu, A.; Lai, F.; Valenti, D.; Manconi, M.; Loy, G.; Bonsignore, L.; Fadda, A. M. Liposomal Incorporation of Artemisia Arborescens L. Essential Oil and in Vitro Antiviral Activity. *European Journal of Pharmaceutics and Biopharmaceutics* **2005**, *59* (1), 161–168. https://doi.org/10.1016/j.ejpb.2004.06.005.

(122) Quintão, F. J. O.; Tavares, R. S. N.; Vieira-Filho, S. A.; Souza, G. H. B.; Santos, O. D. H. Hydroalcoholic Extracts of Vellozia Squamata: Study of Its Nanoemulsions for Pharmaceutical or Cosmetic Applications. *Revista Brasileira de Farmacognosia* **2013**, *23* (1), 101–107. https://doi.org/10.1590/S0102-695X2013005000001.